



# Small Scale Mass Flow Plug Calibration

*Jonathan Sasson*

*Case Western Reserve University, Cleveland, Ohio*

## NASA STI Program . . . in Profile

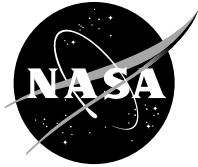
Since its founding, NASA has been dedicated to the advancement of aeronautics and space science. The NASA Scientific and Technical Information (STI) Program plays a key part in helping NASA maintain this important role.

The NASA STI Program operates under the auspices of the Agency Chief Information Officer. It collects, organizes, provides for archiving, and disseminates NASA's STI. The NASA STI Program provides access to the NASA Technical Report Server—Registered (NTRS Reg) and NASA Technical Report Server—Public (NTRS) thus providing one of the largest collections of aeronautical and space science STI in the world. Results are published in both non-NASA channels and by NASA in the NASA STI Report Series, which includes the following report types:

- **TECHNICAL PUBLICATION.** Reports of completed research or a major significant phase of research that present the results of NASA programs and include extensive data or theoretical analysis. Includes compilations of significant scientific and technical data and information deemed to be of continuing reference value. NASA counter-part of peer-reviewed formal professional papers, but has less stringent limitations on manuscript length and extent of graphic presentations.
- **TECHNICAL MEMORANDUM.** Scientific and technical findings that are preliminary or of specialized interest, e.g., “quick-release” reports, working papers, and bibliographies that contain minimal annotation. Does not contain extensive analysis.
- **CONTRACTOR REPORT.** Scientific and technical findings by NASA-sponsored contractors and grantees.
- **CONFERENCE PUBLICATION.** Collected papers from scientific and technical conferences, symposia, seminars, or other meetings sponsored or co-sponsored by NASA.
- **SPECIAL PUBLICATION.** Scientific, technical, or historical information from NASA programs, projects, and missions, often concerned with subjects having substantial public interest.
- **TECHNICAL TRANSLATION.** English-language translations of foreign scientific and technical material pertinent to NASA's mission.

For more information about the NASA STI program, see the following:

- Access the NASA STI program home page at <http://www.sti.nasa.gov>
- E-mail your question to [help@sti.nasa.gov](mailto:help@sti.nasa.gov)
- Fax your question to the NASA STI Information Desk at 757-864-6500
- Telephone the NASA STI Information Desk at 757-864-9658
- Write to:  
NASA STI Program  
Mail Stop 148  
NASA Langley Research Center  
Hampton, VA 23681-2199



# Small Scale Mass Flow Plug Calibration

*Jonathan Sasson*

*Case Western Reserve University, Cleveland, Ohio*

National Aeronautics and  
Space Administration

Glenn Research Center  
Cleveland, Ohio 44135

## Acknowledgments

I would like to extend my gratitude to my adviser, Dr. Paul Barnhart, for his support and guidance throughout the course of my thesis work. His expertise was invaluable. I am a better engineer because of his dedication as an adviser. I want to thank my committee members, Dr. Joseph Prah and Dr. Yasuhiro Kamotani for their comments and suggestions that improved the quality of my thesis. I also want to thank Dr. David Davis for allowing me to test at NASA Glenn Research Center (GRC) and getting the funding to do so. Without his efforts this work could not have been accomplished. He helped procure funding from the LERCIP intern program for the numerical study, and from the High-Speed Project of NASA's Fundamental Aeronautics Program for the experimental work. Lastly, I thank Sierra Lobo for allowing me to take the necessary time to complete my work and supporting me through the last year of my education.

This report contains preliminary findings,  
subject to revision as analysis proceeds.

This work was sponsored by the Fundamental Aeronautics Program  
at the NASA Glenn Research Center.

*Level of Review:* This material has been technically reviewed by NASA technical management.

Available from

NASA STI Program  
Mail Stop 148  
NASA Langley Research Center  
Hampton, VA 23681-2199

National Technical Information Service  
5285 Port Royal Road  
Springfield, VA 22161  
703-605-6000

This report is available in electronic form at <http://www.sti.nasa.gov/> and <http://ntrs.nasa.gov/>

# Contents

|   |          |
|---|----------|
| List of Figures                                     | i        |
| List of Tables                                      | iii      |
| List of Symbols                                     | iv       |
| List of Acronyms                                    | vii      |
| Acknowledgments                                     | viii     |
| Abstract  | ix       |
| <b>1 Introduction</b>                               | <b>1</b> |
| 1.1 Calibration . . . . .                           | 3        |
| 1.2 Distortion . . . . .                            | 4        |
| <b>2 Analysis Methodology</b>                       | <b>6</b> |
| 2.1 System Description . . . . .                    | 6        |
| 2.1.1 Minimum Geometric Area . . . . .              | 9        |
| 2.2 Control Volume Analysis . . . . .               | 11       |
| 2.2.1 Inviscid Solution . . . . .                   | 14       |
| 2.2.2 Skin Friction Model . . . . .                 | 16       |
| 2.2.3 Coupled System/Viscous Model . . . . .        | 18       |
| 2.2.4 Boundary Layer Analysis . . . . .             | 21       |
| 2.2.4.1 Momentum Integral - Waltz' Method . . . . . | 21       |
| 2.2.4.2 Waltz' Method Solution . . . . .            | 24       |
| 2.2.4.3 Method of Solution . . . . .                | 25       |
| 2.3 CFD Analysis . . . . .                          | 25       |
| 2.3.1 Calibration Mesh . . . . .                    | 27       |
| 2.3.1.1 Turbulence Model . . . . .                  | 29       |
| 2.3.1.2 Stability Condition . . . . .               | 29       |
| 2.3.1.3 Convergence . . . . .                       | 30       |
| 2.3.2 Distortion Mesh . . . . .                     | 30       |

|                     |   |            |
|---------------------|---|------------|
| <b>3</b>            | <b>Experiment</b>                               | <b>32</b>  |
| 3.1                 | 6WB Facility . . . . .                          | 32         |
| 3.2                 | Test Setup . . . . .                            | 34         |
| 3.3                 | Instrumentation . . . . .                       | 36         |
| 3.3.1               | Stations . . . . .                              | 36         |
| 3.3.2               | LVDT . . . . .                                  | 39         |
| 3.4                 | ASME Nozzle . . . . .                           | 39         |
| 3.5                 | Operation . . . . .                             | 41         |
| 3.5.1               | Baseline Calibration . . . . .                  | 42         |
| 3.5.2               | Distortion Generation . . . . .                 | 42         |
| 3.6                 | Uncertainties . . . . .                         | 46         |
| <b>4</b>            | <b>Results and Discussion</b>                   | <b>49</b>  |
| 4.1                 | Non-Distorted Calibration . . . . .             | 49         |
| 4.2                 | Distortion Description . . . . .                | 56         |
| 4.2.1               | Pattern Descriptors . . . . .                   | 56         |
| 4.2.2               | Numerical Descriptors . . . . .                 | 57         |
| 4.3                 | Pressure Decay . . . . .                        | 61         |
| 4.3.1               | Non-Distorted Case . . . . .                    | 61         |
| 4.3.2               | Distorted Case . . . . .                        | 62         |
| 4.4                 | Distortion Results . . . . .                    | 64         |
| <b>5</b>            | <b>Conclusion</b>                               | <b>76</b>  |
| <b>Appendix A</b>   | <b>Method of Solution</b>                       | <b>79</b>  |
| A.0.1               | Single Varibale Newton-Raphson Method . . . . . | 79         |
| A.0.2               | Multi-Variable Newton-Raphson Method . . . . .  | 80         |
| A.0.3               | LU Decomposition . . . . .                      | 82         |
| A.0.4               | Fourth Order Runge-Kutta . . . . .              | 84         |
| A.0.5               | Bicubic Spline Interpolation . . . . .          | 85         |
| <b>Appendix B</b>   | <b>Uncertainty Analysis</b>                     | <b>87</b>  |
| <b>Appendix C</b>   | <b>Engineering Drawings</b>                     | <b>89</b>  |
| <b>Bibliography</b> |   | <b>102</b> |

# List of Figures

|      |  |    |
|------|--|----|
| 1.1  | Low-boom inlet test at NASA GRC 8x6ft SWT. . . . .                             | 1  |
| 1.2  | Low-boom inlet/MFP configuration. . . . .                                      | 2  |
| 2.1  | Components of the calibration rig and control volume elements. . . .           | 7  |
| 2.2  | Schematic for calculating MFP minimum area. . . . .                            | 10 |
| 2.3  | Minimum geometric area . . . . .   | 12 |
| 2.4  | Sample control volume with the flow quantities. . . . .                        | 14 |
| 2.5  | Main Components of the N+2 Calibration Rig. . . . .                            | 26 |
| 2.6  | Mesh of N+2 calibration rig including the plenum. . . . .                      | 28 |
| 3.1  | 15 by 15 cm SWT facility without experimental hardware. . . . .                | 32 |
| 3.2  | Test setup and instrumentation stations. . . . .                               | 35 |
| 3.3  | Upstream view of the AIP instrumentation rake. . . . .                         | 38 |
| 3.4  | Upstream view of the MFP instrumentation rake. . . . .                         | 39 |
| 3.5  | Mass-flow plug in housing. . . . .   | 40 |
| 3.6  | Distortion devices modeled after measured AIP profile. . . . .                 | 47 |
| 4.1  | MFP discharge coefficient results. . . . .                                     | 52 |
| 4.2  | ASME nozzle calibration. . . . .   | 53 |
| 4.3  | MFP discharge coefficient results with reduced "ideal" mass flow rate. . . . . | 54 |
| 4.4  | Numerical calibration results at different pressure ratios. . . . .            | 55 |
| 4.5  | Circumferential distortion. . . . .  | 59 |
| 4.6  | Ring circumferential distortion. . . . .                                       | 60 |
| 4.7  | Pressure variations in non-distorted calibration. . . . .                      | 63 |
| 4.8  | AIP versus MFP distortion. . . . .   | 65 |
| 4.9  | Inlet and CFD distortion results. . . . .                                      | 69 |
| 4.10 | Experimental distortion results for screen 15.1. . . . .                       | 70 |
| 4.11 | Distortion results for all screens. . . . .                                    | 71 |
| 4.12 | Distortion results for screen 7. . . . .                                       | 72 |
| 4.13 | Distortion results for screen 8.1. . . . .                                     | 72 |
| 4.14 | Distortion results for screen 9.1. . . . .                                     | 73 |
| 4.15 | Distortion results for screen 14.1. . . . .                                    | 73 |
| 4.16 | Distortion results for screen 15.1. . . . .                                    | 74 |
| 4.17 | Distortion results with weighted flow corrected by MFP pressure. . . .         | 75 |
| C.1  | MFP calibration rig assembly. . . . .  | 90 |

|      |                                       |     |
|------|---------------------------------------|-----|
| C.2  | MFP support assembly- part 1. . . . . | 91  |
| C.3  | MFP support assembly- part 2. . . . . | 92  |
| C.4  | MFP support assembly- part 3. . . . . | 93  |
| C.5  | Settling chamber- part 1. . . . .     | 94  |
| C.6  | Settling chamber- part 2. . . . .     | 95  |
| C.7  | Settling chamber- part 3. . . . .     | 96  |
| C.8  | Connecting flange. . . . .            | 97  |
| C.9  | ASME nozzle- part 1. . . . .          | 98  |
| C.10 | ASME nozzle- part 2. . . . .          | 99  |
| C.11 | ASME nozzle- part 3. . . . .          | 100 |



# List of Tables

|     |                                    |    |
|-----|------------------------------------|----|
| 3.1 | Test Matrix . . . . .              | 43 |
| 3.2 | Distortion screens. . . . .        | 46 |
| 3.3 | Summary of uncertainties . . . . . | 48 |

# List of Symbols

|             |  |
|-------------|--|
| $A$         | Area   |
| $AR$        | Area ratio                                       |
| $C$         | Courant-Friedrichs-Lewy number                   |
| $C_D$       | Discharge coefficient                            |
| $C_f$       | Skin friction coefficient                        |
| $C_0$       | Sutherland's law temperature constant            |
| $D$         | Diameter   |
| $F_c$       | van Driest's parameter                           |
| $F_i$       | Algebraic functions in Walz's method             |
| $h$         | Height   |
| $H$         | Shape factor                                     |
| $K_{A2}$    | Radial and circumferential distortion descriptor |
| $K_r$       | Radial distortion descriptor                     |
| $K_\theta$  | Circumferential distortion descriptor            |
| $L$         | Length   |
| $m$         | Slope linear equation                            |
| $\dot{m}$   | Mass flow rate                                   |
| $M$         | Mach number                                      |
| $N$         | Integer  |
| $p$         | Coordinate point                                 |
| $P$         | Pressure   |
| $Pr$        | Prandtl number; pressure ratio                   |
| $q$         | Dynamic pressure                                 |
| $s$         | Slant height                                     |
| $S$         | Surface area                                     |
| $r$         | Radius; recovery factor                          |
| $R$         | Specific gas constant                            |
| $Re$        | Reynolds number                                  |
| $t$         | Time   |
| $T$         | Temperature                                      |
| $U$         | Velocity   |
| $x, y, z$   | Cartesian coordinates                            |
| $r, \theta$ | Cylindrical coordinates                          |
| $w$         | Corrected flow                                   |
| $W$         | Shape factor                                     |

|     |                              |
|-----|------------------------------|
| $Z$ | Momentum thickness parameter |
|-----|------------------------------|

## Greek Symbols

|            |  |
|------------|--|
| $\beta$    | Dimensionless parameter in Walz's method                         |
| $\gamma$   | Specific heat ratio  |
| $\delta$   | Velocity boundary layer thickness; referred pressure             |
| $\delta^*$ | Displacement thickness   |
| $\delta_3$ | Dissipation thickness  |
| $\epsilon$ | Numerical tolerance  |
| $\mu$      | Viscosity  |
| $\nu$      | Kinematic viscosity  |
| $\phi$     | Cone angle   |
| $\theta$   | Polar coordinate angle; momentum thickness; referred temperature |
| $\rho$     | Density  |
| $\tau$     | Shear stress   |
| $\Omega$   | Square root of $F_c$   |

## Subscripts

|               |   |
|---------------|---|
| 0             | Initial or reference value                  |
| 1             | Upstream or first value                     |
| 2             | Downstream or second value                  |
| <i>actual</i> | Actual                                      |
| <i>aw</i>     | Adiabatic wall                              |
| <i>c</i>      | Contour                                     |
| <i>calc</i>   | Calculated value from control volume method |
| <i>d</i>      | Distorted                                   |
| <i>D</i>      | Diameter                                    |
| <i>e</i>      | Exit value; boundary layer edge             |
| <i>eff</i>    | Effective                                   |
| <i>ideal</i>  | Ideal                                       |
| <i>L</i>      | Length                                      |
| <i>min</i>    | Minimum                                     |
| <i>max</i>    | Maximum                                     |
| <i>plug</i>   | Plug's position $s$                         |
| Surface       |   |
| <i>turb</i>   | Turbulent                                   |
| <i>T</i>      | Total (stagnation) condition                |
| <i>u</i>      | Undistorted                                 |
| <i>w</i>      | Wall  |

## Superscripts

|                 |                             |
|-----------------|-----------------------------|
| $+$             | Law of the wall             |
| $\overline{()}$ | Average quantity            |
| $n$             | Exponential constant        |
| $'$             | Difference in plug position |

# List of Acronyms

|      |  |
|------|--|
| AIP  | Aerodynamic Interface Plane              |
| ASME | American Society of Mechanical Engineers |
| CAD  | Computer Aided Design                    |
| CFD  | Computational Fluid Dynamics             |
| CFL  | Courant Friedrichs Lewy                  |
| CSV  | Comma Separated Variables                |
| CV   | Control Volume                           |
| ESP  | Electronically Scanned Pressure          |
| GRC  | Glenn Research Center                    |
| LVDT | Linear Variable Differential Transducer  |
| MFP  | Mass Flow Plug                           |
| MPR  | Multiple Per Revolution                  |
| QEVC | Quiet Experimental Validation Concept    |
| SST  | Shear Stress Transport                   |
| SWT  | Supersonic Wind Tunnel                   |



# **Small Scale Mass Flow Plug Calibration**

Jonathan Sasson  
Case Western Reserve University  
Cleveland, Ohio 44106

## **Abstract**

A simple control volume model has been developed to calculate the discharge coefficient through a mass flow plug (MFP) and validated with a calibration experiment. The maximum error of the model in the operating region of the MFP is 0.54%. The model uses the MFP geometry and operating pressure and temperature to couple continuity, momentum, energy, an equation of state, and wall shear. Effects of boundary layer growth and the reduction in cross-sectional flow area are calculated using an integral method. A CFD calibration is shown to be of lower accuracy with a maximum error of 1.35%, and slower by a factor of 100. Effects of total pressure distortion are taken into account in the experiment. Distortion creates a loss in flow rate and can be characterized by two different distortion descriptors.

# Chapter 1

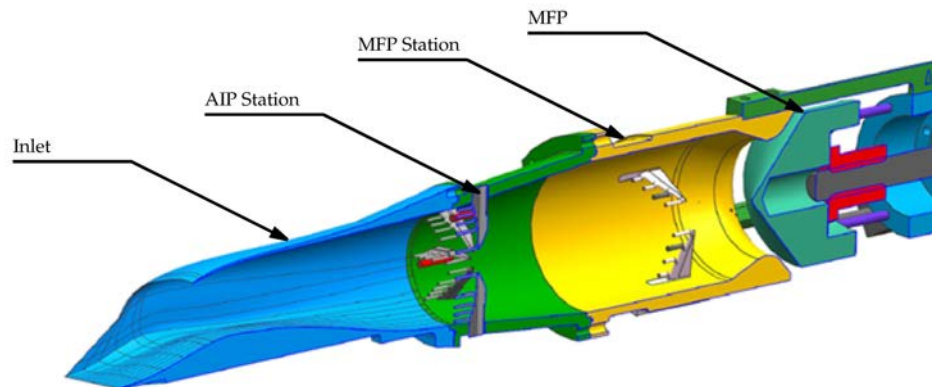
## Introduction



**Figure 1.1:** *Low-boom inlet test at NASA GRC 8x6ft SWT.*

Prior to coupling a high-speed inlet to an actual turbine engine, the performance of the inlet is usually evaluated by testing the inlet with a device that simulates the air flow demand of the engine. The inlet must also hold stable operation over a range of mass flow rates. Accurate measurement of the mass flow rate is therefore





**Figure 1.2:** *Low-boom inlet/MFP configuration.*

necessary. Due to its mechanical simplicity, the air flow through an inlet is often controlled and measured with a mass flow plug which is typically a pipe whose exit area is regulated by translating a body of revolution along the axis of the pipe [1]. The body of revolution is usually conical, but other shapes have been used, and the pipe may be constant area with a sharp corner or variable area with a contour at the exit. Similar mass flow plugs are also used during the testing phase to control and measure boundary-layer bleed flow typically incorporated in high-speed inlets for shock wave stability and enhanced performance.

To achieve the highest mass-flow measurement accuracy, the mass flow plug must be calibrated prior to testing. Most often, calibration of the mass flow plug is performed with well-defined, uniform flow conditions. During inlet testing shock-wave/boundary-layer interactions and flow separation in the subsonic diffuser can significantly distort the flow approaching the mass flow plug. To mitigate the effects of distortion on the mass flow plug calibration, the usual practice of providing at least 10 diameters of development length ahead of the mass flow plug (MFP) is recommended. On larger scale inlets models or in applications where there are multiple engines, 10 diameters are not always practical so the effects of flow distortion must be accounted for during the calibration.

The consequences of distortion on intake testing are apparent in a recent test

performed by Boeing where they characterized the flow through an inlet integrated onto a low-boom supersonic cruise aircraft concept in NASA GRC's 8x6ft Supersonic Wind Tunnel (SWT). Figure 1.1 shows a photograph of the Boeing Quiet Experimental Validation Concept (QEVC) model installed in the 8x6ft SWT with the MFP prominently featured on the starboard side. The MFP was of the type shown in Figure 1.2 [2] and was close-coupled to the inlet as shown. In this figure, the rakes at the Aerodynamic Interface Plane (AIP) station characterize the flow that would enter the engine and the rakes at the MFP station are used for calibration of the MFP. Prior to the 8x6ft SWT test, Boeing experimentally calibrated the MFP under undistorted flow conditions. During the 8x6ft SWT inlet test, the flow conditions, with various levels of flow distortion, were recorded at the AIP and MFP rake stations. The levels of total pressure distortion were high enough to question whether the MFP calibration could be used reliably to determine the flow rate through the inlet.

## 1.1 Calibration

The ultimate goal of the calibration is to determine a discharge coefficient,  $C_D$ , Equation 1.1, for the mass flow plug over an operating range typical of the supersonic testing inlet. It is defined as the ratio of actual mass flow rate to ideal mass flow rate. In other words, it is the ratio of the mass flow rate at the discharge end of a flow device to that of an idealized device expanding at the same initial and final conditions.

$$C_D = \frac{\dot{m}_{actual}}{\dot{m}_{ideal}} \quad (1.1)$$

where  $\dot{m}_{ideal}$  is the ideal inviscid flow rate through the mass flow plug.

The difference between theoretical and actual values is due to viscous effects of the

boundary layer on the wall and heat addition. Apart from friction forces viscosity also creates a boundary layer. The fluid in the boundary layer is moving slower compared to the core-flow and reduces the effective flow area. A meaningful measure of the boundary layer thickness is the displacement thickness. It is a measure of the distance by which the internal potential flow is displaced inwards as a consequence of the decrease in velocity in the boundary layer.

Varying the plug position creates a means to vary the back pressure on the inlet. The position is varied by an electric motor and it is measured by a Linear Variable Differential Transducer (LVDT). The four primary components of the calibration rig are the American Society of Mechanical Engineers (ASME) inlet flow nozzle assembly, an adapter spool piece, the cold-pipe assembly, and the mass-flow plug assembly. The ASME nozzle measures the flow rate, and draws air from either a plenum tank or the atmosphere. The wind tunnel exhausters are used as a vacuum source to establish flow through the assembly and to assure the flow is choked at the MFP throat. Plug position and minimum area are defined differently for each plug.

## 1.2 Distortion

Distortion characterizes the non-uniformity of flow at entry to the engine. It is typically measured in terms of the variation of total pressure across the face of the engine – the aerodynamic interface plane. This simple descriptor does not take into account radial or azimuthal variations in pressure. Failure to understand the full nature of the flow field and the sensitivity of the engine to distortion has led to performance and stability problems [3].

Ultimately, it is the engine sensitivity which determines whether the total pressure distribution is a sufficient descriptor of the intake distortion. The same criteria can be applied to MFP testing of an inlet. Although great efforts are taken to avoid

distortion during MFP calibration, some level of it is always apparent during actual testing. Significant distortion approaching the MFP results in an increase in the level of uncertainty in the indicated inlet mass flow rates. To reduce the level of uncertainty, the MFP should be also calibrated with distorted flow; this leads to a distortion descriptor that correlates the discrepancies between undistorted and distorted flow.

# Chapter 2

## Analysis Methodology

### 2.1 System Description

Due to the high costs of wind tunnel testing, it is often not feasible to calibrate the flow nozzle or the MFP. Recently, there has been a substantial increase in the demand of CFD predictions since these are cheaper. They are still time consuming and require the researcher to work closely with a CFD analyst. The goal of this analysis is to create a one-dimensional model that can be implemented by a researcher for any calibration geometry, and obtain a solution that is of comparable accuracy as the CFD results.

A rapid method for calculating the discharge coefficient,  $C_D$ , for a Mass Flow Plug (MFP) is desired that can be used in lieu of an experimentally determined calibration. The method must be able to capture the geometric variations of typical mass flow plugs operating under a range of flow rates, pressures, and temperatures. A control volume analysis has been developed to perform this calculation of the discharge coefficient for nominal, undistorted, axisymmetric flows through a MFP.

The control volume analysis developed for this work is comprised of a sequence of flow calculations through the MFP. The first pass uses an inviscid, compressible

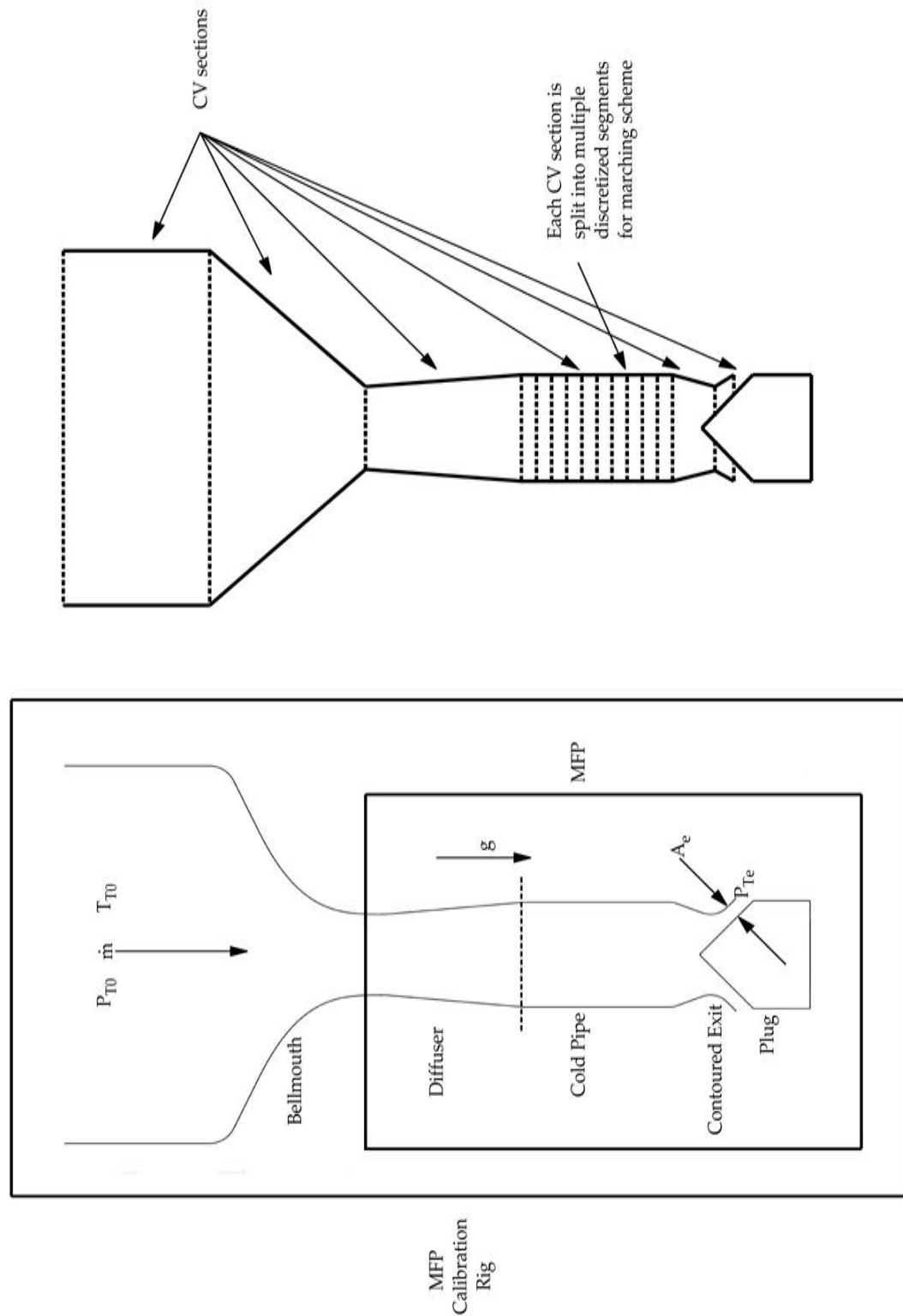


Figure 2.1: Components of the calibration rig and control volume elements.

one-dimensional stream-tube model. The second pass calculates a wall shear based on the results from the first inviscid calculation as the flow properties at the edge of the boundary layer using a compressible, turbulent skin friction model. The third pass solves a coupled set of one-dimensional relations for conservation of mass, momentum, energy, an equation of state, and the wall shear calculated in the second calculation. The result of these successive calculations is an accurate one-dimension model of the velocity, pressure, and temperature through the MFP.

The discharge coefficient calculation must also include the effects of boundary layer growth, and the reduction in cross-sectional flow area as characterized by the boundary layer displacement thickness. The last calculation in the sequence uses an integral method to calculate the growth of the boundary layer, from which the displacement thickness is then determined.

The goal of the calibration is to establish a relationship between plug position and discharge coefficient. The calibration rig must be long enough in order for the flow to settle and prevent total pressure distortion. A baseline calibration is established without any distortion devices. Transverse variation in total pressure is due solely to boundary layer growth. This baseline is used to compare against a calibration which deliberately creates total pressure distortion to better simulate inlet conditions. It is important to note that some total pressure loss is always present in the baseline calibration due to wall friction and boundary layer growth. This loss must be accounted for to establish a more accurate trend between the baseline and distorted calibration.

Figure 2.1 shows the basic physical elements of the calibration rig. Although different MFPs use slightly different configurations, they all follow the same basic guidelines. They all include an intake nozzle that measures the flow rate and draws air from a source (either a plenum tank or the atmosphere), a cold pipe with pressure rakes, and the MFP. Locations of quantities of interest are also shown in Figure 2.1. The flow is assumed choked at the MFP throat, therefore the exit Mach number,  $M_e$ ,

is 1. The ideal mass flow rate is determined by the intake total pressure ,  $P_{T0}$ , the total temperature,  $T_{T0}$ , and the MFP minimum area,  $A_e$ . The exit total pressure,  $P_{Te}$ , is calculated by accounting for losses in the rig. This pressure is used to calculate the actual mass flow rate.

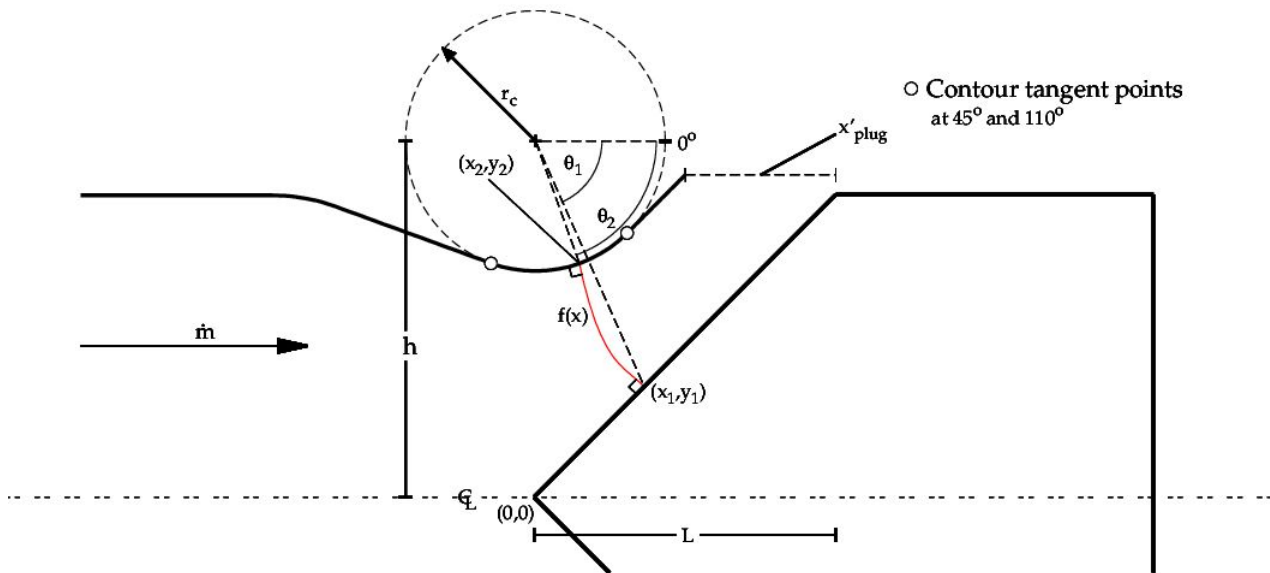
The calibration process is modeled by a series of control volumes across the calibration rig as shown in Figure 2.2. The analysis is also split into four sequential steps. The first step calculates the thermodynamic properties across each control volume isentropically. The second step uses the previous solutions to calculate the wall friction losses. The third step ties together the losses with the isentropic solution using a fully-coupled system of equations to determine the total pressure loss. Finally, the fourth step computes the displacement thickness to correct the effective flow area reduced by boundary layer displacement. The results from these four steps are used to calculate the discharge coefficient,  $C_D$ .

### 2.1.1 Minimum Geometric Area

The minimum geometric area (or throat area) of the MFP must be determined to start the first pass of the control volume analysis. The sonic line is assumed to be perpendicular to surface, therefore the minimum geometric area is approximated by a curve,  $f(x)$ , that is both normal to the cone and the cold pipe's exit as shown in Figure 2.2 and revolved around the  $x$ -axis. Since the cold pipe has a contoured exit (with a radius,  $r_c$ , of 0.43 inches), the location of the curve that creates the minimum area varies by plug position. From Figure 2.2 it is deduced that the minimum area lies between the two tangent points of the contour: between  $45^\circ$  and  $110^\circ$ . This is shown by the white circles on the contour.

To start the calculation a coordinate system with its origin at the tip of the cone is established. The  $x$  location of the center of the contour's circle is given by:





**Figure 2.2:** *Schematic for calculating MFP minimum area.*

$$x_c = L - x'_{pluq} \quad (2.1)$$

The point  $(x_2, y_2)$  at which  $f(x)$  intercepts the contoured exit is defined from the center of the contour and by the angle  $\theta_2$ .

$$\begin{aligned} x_2 &= r_c \cos \theta + x_c \\ y_2 &= h - r_c \sin \theta \end{aligned} \quad (2.2)$$

where  $h$  (1.177 inches) is the height from the center line to the center of the contour. A second angle,  $\theta_1$ , is used to define the point at which  $f(x)$  intercepts the cone. Since the cone is at an angle of 45 degrees,  $x_1 = y_1$ . Therefore:

$$x_1 = \frac{h + x_c \tan \theta_1}{1 + \tan \theta_1}$$

The curve  $f(x)$  is defined by satisfying four distinct boundary conditions. These

boundary conditions are used to find the four constants that define the curve as a cubic. It must pass through both  $(x_1, y_1)$  and  $(x_2, y_2)$  and be perpendicular to both surfaces. Perpendicularity to the cone is satisfied by imposing the surface of the cone as the normal line of  $f(x)$  at  $(x_1, y_1)$ . The radius of curvature of  $f(x)$  at  $(x_2, y_2)$  must equal the contour's radius,  $r_c$  to satisfy perpendicularity. The four boundary conditions are defined as:

$$\begin{aligned} f(x_1) &= y_1 \\ f(x_2) &= y_2 \\ f'(x_1) &= -1 \\ r_c &= \left| \frac{[1 + f'(x_2)^2]^{3/2}}{f''(x_2)} \right| \end{aligned} \tag{2.3}$$

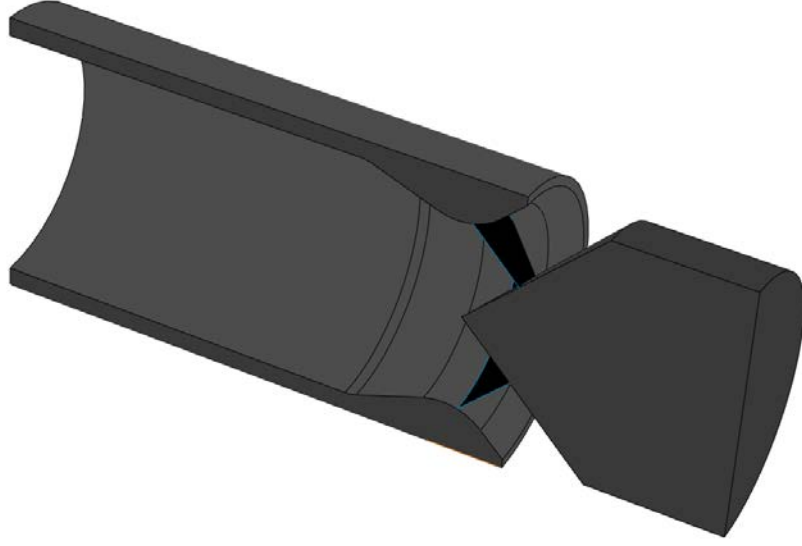
With the four constants known, the area is solved for by revolving the curve around the  $a$ -axis. The surface area of a revolution is determined by

$$A_{throat} = 2\pi \int_{x_1}^{x_2} f(x) \sqrt{1 + f'(x)^2} dx \tag{2.4}$$

Equation 2.4 must be solved for numerically using the 3/8 Simpson's rule. The minimum area depends on both  $\theta_1$  and  $\theta_2$ . The area is optimized by varying the angles, and recomputing the area until the minimum area is reached. The surface area of the revolution is represented in Figure 2.3 as the darker surface.

## 2.2 Control Volume Analysis

To determine the discharge coefficient as given in Equation 1.1 it is necessary to first determine the ideal mass flow rate. A one-dimensional compressible mass flow rate relation is required to account for compressibility effects in the MFP and calibration



**Figure 2.3:** *Minimum geometric area*

rig. The mass flow rate is determined as a function of area,  $A$ , Mach number,  $M$ , total pressure,  $P_T$ , total temperature,  $T_T$ , and gas properties by assuming air is an ideal gas with constant specific heat. The resulting compressible mass flow rate function and its development are presented in Equations 2.5 through 2.11 [4].

$$\dot{m} = \rho U A \quad (2.5)$$

$$U = M \sqrt{\gamma R T} \quad (2.6)$$

$$\rho = \frac{P}{R T} \quad (2.7)$$

$$\dot{m} = A \frac{P}{\sqrt{T}} \sqrt{\frac{\gamma}{R}} M \quad (2.8)$$

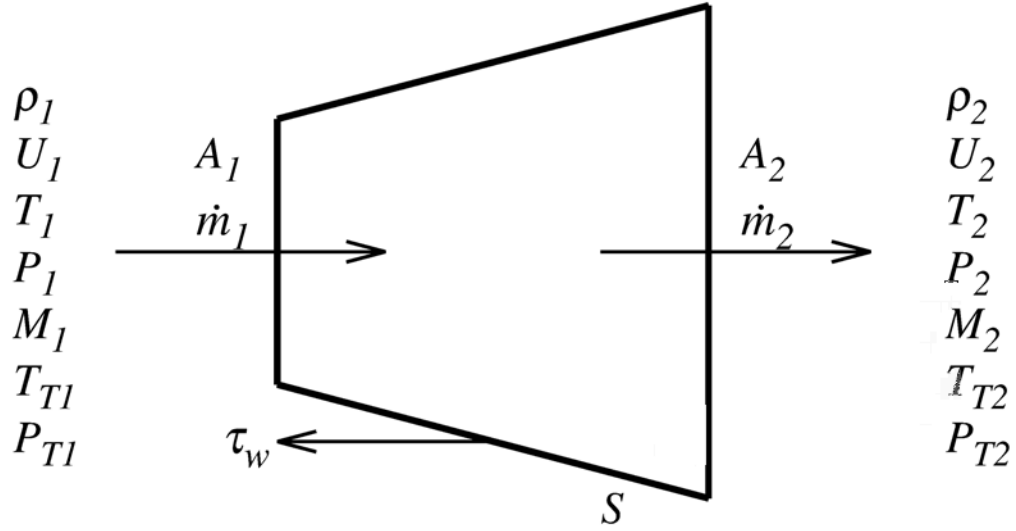
$$P = P_T \left[ 1 + \frac{\gamma - 1}{2} M^2 \right]^{-\frac{\gamma}{\gamma - 1}} \quad (2.9)$$

$$T = T_T \left[ 1 + \frac{\gamma - 1}{2} M^2 \right]^{-1} \quad (2.10)$$

$$\dot{m} = A \frac{P_T}{\sqrt{T_T}} \sqrt{\frac{\gamma}{R}} M \left[ 1 + \frac{\gamma - 1}{2} M^2 \right]^{-\frac{\gamma+1}{2(\gamma-1)}} \quad (2.11)$$

In order to determine the internal flow characteristics of the MFP and calibration rig it is first discretized into a number of segments. The geometry of each section contributes to create a series of one-dimensional control volumes. The inner surfaces create the real boundaries, and the entrance and exit cross-sectional areas of each segment create the imaginary boundaries of the control volume element. The sum of the volume elements create a stream-tube representation of the internal control volume [5]. Each control volume element is further subdivided into smaller sections to create a stream-tube from very small discretized control volume sections. Figure 2.4 represents a visualization of a one-dimensional discretized control volume element. The figure also shows the stream-tube the control-volumes create. The internal flow solutions of the one-dimensional stream-tube correspond to physical locations on the calibration rig (shown in Figure 2.1).

The required geometric information for each one-dimensional control volume element of Figure 2.4 consists of the upstream and downstream areas,  $A_1$  and  $A_2$  respectively, and the total surface area,  $S$ . All flow quantities are assumed constant perpendicular to the flow across the volume elements, and are only calculated at the upstream and downstream boundaries. The flow quantities calculated at each imaginary boundary of the control volume are: density,  $\rho$ , axial velocity,  $U$ , pressure,  $P$ , temperature,  $T$ , total temperature,  $T_T$ , total pressure,  $P_T$ , Mach number,  $M$ .



**Figure 2.4:** *Sample control volume with the flow quantities.*

### 2.2.1 Inviscid Solution

The first step in the methodology is to compute the flow quantities presented in the previous section from a simple statement of conservation of mass presented in Equation 2.8.

$$\dot{m}_1 = \dot{m}_2 \quad (2.12)$$

Equation 2.11 and 2.12 are combined to develop compressible one-dimensional stream tube relation, and it is shown in Equation 2.13. Even though Equation 2.13 takes into account changes in total pressure and temperature, the flow is modeled isentropically in the first step. Therefore the upstream total pressure and temperature remain constant along the stream tube. The only parameter that corresponds to a change in Mach number is the change in flow area across a volume element.

$$A_1 \frac{P_{T1}}{\sqrt{T_{T1}}} \sqrt{\frac{\gamma}{R}} M_1 \left[ 1 + \frac{\gamma-1}{2} M_1^2 \right]^{-\frac{\gamma+1}{2(\gamma-1)}} = A_2 \frac{P_{T2}}{\sqrt{T_{T2}}} \sqrt{\frac{\gamma}{R}} M_2 \left[ 1 + \frac{\gamma-1}{2} M_2^2 \right]^{-\frac{\gamma+1}{2(\gamma-1)}} \quad (2.13)$$

The first pass analysis starts at the bellmouth's entrance and marches downstream across each volume element, using Equation 2.13 to determine the downstream Mach number from the known upstream Mach number and cross-sectional areas. The downstream Mach number then becomes the upstream Mach number for the next volume element marching the solution downstream. The temperatures and pressures are determined from the known Mach numbers and Equations 2.9 and 2.10 respectively. Velocity and density are computed from Equations 2.6 and 2.7. Due to the isentropic assumption, the total pressure and temperature are constant across each volume element.

Equation 2.13 cannot be solved explicitly for the downstream Mach number  $M_2$ . It is therefore solved iteratively using a single variable Newton-Raphson iteration scheme. Equation 2.13 is rewritten as Equation 2.14 such that each term on the left-hand-side is normalized and approximately unity in magnitude. This helps the convergence of the iteration scheme. The ratio of total pressure and temperature is exactly 1 under inviscid assumptions and therefore not shown in Equation 2.14.

$$\left( \frac{A_1}{A_2} \right) - \frac{M_2}{M_1} \left[ \frac{1 + \frac{\gamma-1}{2} M_2^2}{1 + \frac{\gamma-1}{2} M_1^2} \right]^{-\frac{\gamma+1}{2(\gamma-1)}} = 0 \quad (2.14)$$

To start the first step in the analysis, Equation 2.14 is used to solve for the bellmouth's entrance Mach number. The upstream and downstream areas correspond to the bellmouth's entrance and MFP minimum geometric exit, respectively. The downstream Mach number is 1 since the MFP is choked at the exit for the pressure ratio imposed. Equation 2.14 is solved using the single variable Newton-Raphson iteration scheme.

### 2.2.2 Skin Friction Model

The inviscid flow solution determined in the first step is used to calculate the surface shear force using boundary layer theory. The inviscid velocity, density, temperature, and Mach number become the boundary layer edge quantities, denoted by the subscript  $e$ . The wall shear per unit surface area is given in Equation 2.15 as a function of density and velocity at the boundary layer edge, and the skin friction coefficient,  $C_f$ . Since the edge velocity and density are known from the previous inviscid calculation, the only variable left to be determined is the skin friction coefficient.

$$\tau_w = \frac{1}{2} \rho_e U_e^2 C_f \quad (2.15)$$

The flow is assumed turbulent throughout the calculation. Since the pressure gradient is larger across the throat region and it covers a small segment compared to the rest of the rig, the calculation assumes no significant pressure gradient. With these assumptions, a flat plate compressible turbulent skin friction coefficient formulation of White and Christoph is used. This correlation has proven very accurate over the entire practical range of Reynolds numbers, Mach numbers, and wall temperatures. A complete derivation of the method is found in Reference [6].

The simple formula for turbulent skin friction on a flat plate as determined by White and Christoph is:

$$C_f \approx \frac{0.455}{\Omega^2 \ln^2 \left( \frac{0.06}{\Omega} \frac{Re_L}{2} \frac{\mu_e}{\mu_w} \sqrt{\frac{T_e}{T_w}} \right)} \quad (2.16)$$

$\Omega$  is the square root of van Driest's parameter  $F_c$ . The details of this parameter are also presented in Reference [6].

$$\Omega = \frac{\sqrt{\frac{T_{aw}}{T_e} - 1}}{\sin^{-1} a^{3/2} + \sin^{-1} \frac{1}{2\sqrt{a}}} \quad (2.17)$$

where

$$a = \sqrt{\frac{\gamma - 1}{2} M_e^2 \frac{T_e}{T_{aw}}} \quad (2.18)$$

The equations presented here are a simplified version from those found in Reference num by assuming adiabatic flow. Equation 2.16 also accounts for the axisymmetric geometry of the calibration rig by using the turbulent cone rule, or an approximate Mangler transformation. This is apparent in the factor of 1/2 in the Reynolds number. The adiabatic wall temperature,  $T_{aw}$ , depends on the static temperature, Mach number and recovery factor,  $r$ , as presented in Equation 2.19:

$$T_{aw} = T_e \left( 1 + r \frac{\gamma - 1}{2} M_e^2 \right) \quad (2.19)$$

The recovery factor is calculated by breaking the law of the wall into three different parts: a linear layer for  $y^+ < 5$ , a buffer layer for  $5 < y^+ < 30$ , and a log layer for  $y^+ > 30$ . By assuming a constant turbulent Prandtl number, the velocity and temperature profiles are integrated to obtain an estimate for the turbulent recovery factor. The details of the derivation are presented in Reference [7].

$$r_{turb} \approx Pr^{1/3} \quad (2.20)$$

The predominant term in the calculation of the skin friction coefficient is the Reynolds number based on length. The length used to calculate the Reynolds number is not a physical length but rather is defined by Equation 2.23. It is determined by dimensional arguments. Since the volume element does not account for an axial length, an effective length is approximated by the surface area,  $S$ , of the volume element. The running length is the sum of all the effective lengths of the preceding volume elements.

Each control element is modeled as a conical frustum as seen in Figure 2.4. The



surface area of the frustum is defined by Equation 2.21, where the base and the top radius of the frustum are defined by  $R_1$  and  $R_2$  respectively. These can be rewritten in terms of the cross-sectional areas at the entrance and exit ( $A_1$  and  $A_2$ ) of the volume element shown in Equation 2.22. Substituting Equation 2.22 into Equation 2.21 yields the effective length  $L$  shown in Equation 2.23.

$$S = \pi(R_1 + R_2)\sqrt{(R_1 - R_2)^2 + L^2} \quad (2.21)$$

$$R_n = \sqrt{\frac{A_n}{\pi}} \quad (2.22)$$

$$L = \frac{1}{\sqrt{\pi}} \sum_{n=2}^N \frac{\sqrt{S_n^2 - (A_n - A_{n-1})^2}}{\sqrt{A_{n-1}} + \sqrt{A_n}} \quad (2.23)$$

$$Re_L = \frac{\rho_e U_e L}{\mu_e} \quad (2.24)$$

Finally, the viscosity is calculated by the Sutherland-law approximation and it is presented in Equation 2.25. The variables  $\mu_0$  ( $3.584 \times 10^{-7} \text{ lb-s/ft}^2$ ),  $T_0$  (491.6  $R$ ), and  $C_0$  (198.6  $R$ ) are constants in the Sutherland-law approximation specific for the gas to be modeled [6].

$$\mu(T) \approx \mu_0 \left( \frac{T}{T_0} \right)^{3/2} \frac{T_0 + C_0}{T + C_0} \quad (2.25)$$

### 2.2.3 Coupled System/Viscous Model

The results of the second step do not contain the necessary information to calculate the discharge coefficient. The effects of wall shear calculated in the second step violate the assumptions of the isentropic flow model used in the first step. A third step is required to couple the effects of wall shear stress on the internal MFP calibration rig

flow solutions. Wall shear stress creates a small loss in total pressure which results in a reduction in mass flow compared to the one calculated by isentropic assumptions in the first step.

The 7 downstream quantities ( $\rho_2$ ,  $U_2, T_2$ ,  $P_2$ ,  $T_{T2}$ ,  $P_{T2}$ , and  $M_2$ ) are determined from the 7 known upstream quantities ( $\rho_1$ ,  $U_1, T_1$ ,  $P_1$ ,  $T_{T1}$ ,  $P_{T1}$ , and  $M_1$ ) including the effects of wall shear [5]. Figure 2.2 is a representation of this system. The 7 necessary governing equations to solve for the 7 unknowns are presented in Equations 2.26 through 2.32. These relations create a system of equations that must be solved simultaneously, and a multi-variable Newton-Raphson iteration scheme is used. Each term in the equations are once again normalized to provide a value close to unity to aid in the convergence of the iteration scheme. The isentropic flow solution is used as the initial guess for the 7 variables the iteration technique. The 7 equations represent characteristics every physical control volume consists of [4].

1. Equation of state for an ideal gas:

$$\frac{\rho_2}{\rho_1} \frac{P_1}{P_2} \frac{T_2}{T_1} - 1 = 0 \quad (2.26)$$

2. Conservation of mass across the volume element:

$$\frac{\rho_2 U_2 A_2}{\rho_1 U_1 A_1} - 1 = 0 \quad (2.27)$$

3. Conservation of momentum across the volume element:

$$\frac{\rho_1 U_1 U_2 A_1 - \rho_1 U_1^2 A_1 + P_2 A_2 - P_1 A_1 - \bar{P}(A_2 - A_1) + \bar{\tau} S}{(P_1 + \frac{1}{2} \rho_1 U_1^2) A_1} = 0 \quad (2.28)$$

( $\bar{P}$  and  $\bar{\tau}$  are the arithmetic averages of the upstream and downstream values across the volume element).

4. Conservation of energy across the volume element:

$$1 - \frac{T_{T2}\rho_2 U_2 A_2}{T_{T1}\rho_1 U_1 A_1} = 0 \quad (2.29)$$

5. Relation between total and static temperature for an ideal gas:

$$\frac{T_{T2}}{T_{T1}} - \frac{T_2}{T_1} \left[ \frac{1 + \frac{\gamma-1}{2} M_2^2}{1 + \frac{\gamma-1}{2} M_1^2} \right] = 0 \quad (2.30)$$

6. Relation between total and static pressure for an ideal gas:

$$\frac{P_{T2}}{P_{T1}} - \frac{P_2}{P_1} \left[ \frac{1 + \frac{\gamma-1}{2} M_2^2}{1 + \frac{\gamma-1}{2} M_1^2} \right]^{\frac{\gamma}{\gamma-1}} = 0 \quad (2.31)$$

7. Relation between velocity and Mach number for an ideal gas:

$$\frac{U_2}{U_1} \frac{M_1}{M_2} \sqrt{\frac{T_1}{T_2}} - 1 = 0 \quad (2.32)$$

The third step in the analysis is similar to the first step in that it computes all the flow properties marching through the volume elements to determine the internal flow. The difference here is that the total pressure does not remain constant because of the wall shear stress effects. Even though total temperature remains constant since there is no heat addition, it is treated as an unknown in the system of equations for completion. It also serves as a redundancy in the calculations. If the total temperature changes, then there is an error in the solution.

This section of the analysis also starts at the bellmouth's entrance and marches downstream to the throat. The flow through the throat is choked. Since the downstream Mach number (unity) is known across this volume element, the system is reduced to a 6 by 6 system. Initially the system is using the ideal mass flow rate determined in the first step (used to calculate the entrance Mach number). In order

to conserve mass, the total pressure in the last control volume will want increase. To avoid the erroneous sudden increase in pressure, the total pressure is assumed constant across the last volume element. This reduces the system of equations on the last control volume even further to a 5 by 5 system. With the new exit total pressure and Mach number of 1, a new mass flow rate is determined. The entrance Mach number is recomputed from this value and the solution marches downstream again. The process is repeated until the mass flow rate is converged. This process determines the entire MFP calibration rig flow properties while accounting for friction losses.

### 2.2.4 Boundary Layer Analysis

The third pass analysis determined the internal flow properties for the calibration rig, however this is still insufficient information to accurately determine the discharge coefficient. Although the previous calculations took into consideration friction losses on total pressure effects, they did not account for the boundary layer displacement thickness which reduces the effective flow area. The third pass determined mass flow rate is lower than the first pass inviscid mass flow rate, but it yields an unrealistic discharge coefficient around 0.99. A fourth step is therefore necessary to determine the boundary layer growth and the displacement thickness. A von Kármán momentum integral equation is applied in this step.

#### 2.2.4.1 Momentum Integral - Waltz' Method

The simple momentum integral equation presented in Equation 2.33 represents a reliable method for calculating the boundary layer displacement thickness. The equation applies to both laminar and turbulent flows. For compressible flow it is necessary to include Mach number effects [8].

$$\frac{d\theta}{dx} + \frac{\theta}{U_e}(2 + H - M_e^2)\frac{dU_e}{dx} = \frac{1}{2}C_f \quad (2.33)$$

where

$$H \equiv \frac{\delta^*}{\theta} \quad (2.34)$$

is the shape factor of the boundary layer velocity profile,  $\delta$  is the boundary layer thickness,  $\delta^*$  is the displacement thickness, and  $\theta$  is the momentum thickness.

$$\delta^*(x) = \int_0^\infty \left( 1 - \frac{\rho}{\rho_e} \frac{u}{U_e} \right) dy \quad (2.35)$$

Equation 2.33 still has too many unknowns ( $\theta$ ,  $H$ ). The skin friction coefficient is defined by Equation 2.16. Walz's method is applicable to both laminar and turbulent boundary layer methods in both low- and high-speed flows [6]. The method introduces a momentum thickness parameter,  $Z$ , and another shape factor,  $W$ .

$$Z = \theta \left( \frac{\rho_e U_e \theta}{\mu_w} \right)^n \quad (2.36)$$

$$W = \frac{\delta_3}{\theta}$$

where  $n = 1$  for laminar flow and  $n = 0.268$  for turbulent flow, and  $\delta_3$  is the compressible kinetic energy thickness. The two coupled first order differential Equations 2.37 and 2.38 are obtained by the substitution of  $Z$  and  $W$  in the momentum and mechanical energy integral relations. Only the parameters  $Z$  and  $W$  are necessary in these equations.

$$\text{Momentum :} \quad \frac{dZ}{dx} + \frac{F_1}{U_e} \frac{dU_e}{dx} Z = F_2 \quad (2.37)$$

$$\text{Mechanical energy :} \quad \frac{dW}{dx} + \frac{F_3}{U_e} \frac{dU_e}{dx} W = \frac{F_4}{Z} \quad (2.38)$$

The four functions  $F_i$  are algebraic functions of the Mach number, Reynolds number based on momentum thickness  $\left(Re_\theta = \frac{\rho_e U_e \theta}{\mu_w}\right)$ , and shape factor  $H = \delta^*/\theta$ .

The formulas are simplified by the intermediate parameters  $a$  and  $b$ , and are defined as:

$$a \approx 0.0394 (W - 1.515)^{0.7}$$

$$b \approx 1 + 0.88 \frac{\gamma - 1}{2} M_e^2 (W) (2 - W)$$

The functions  $F_1$  to  $F_4$  correlated with turbulent data are given by Walz as:

$$F_1 = 2.268 + 1.268H - M_e^2$$

$$F_2 = 1.268 \frac{a}{b}$$

$$F_3 = 1 - H + 0.88(\gamma - 1)M_e^2$$

$$F_4 = \frac{1}{b} \left[ 2\beta \left( \frac{\rho_e U_e \theta}{\mu_w} \right)^{0.168} - aW \right] \quad (2.39)$$

where

$$H = \frac{\delta^*}{\theta} \approx 1 + 1.48(2 - W) + 104(2 - W)^{6.7} \quad (2.40)$$

$$\beta = \left[ \frac{1 + 0.587(\gamma - 1)M_e^2}{1 + 0.44(\gamma - 1)M_e^2} \right]^n \quad (2.41)$$

The exponent  $n$  in the definition of  $\beta$  is the viscosity-temperature exponent, which is 0.67 for air. Separation occurs at  $W = 1.515$  for either laminar and turbulent flow, which is why the parameter  $a$  equals zero at that point.

#### 2.2.4.2 Waltz' Method Solution

The two differential Equations 2.37 and 2.38 are integrated using a 4<sup>th</sup> Order Runge-Kutta integration method to solve for  $Z$ , and  $W$  [9]. The integration is carried downstream starting from bellmouth entrance.

The integration is marched downstream from the starting point across volume elements. The initial conditions at the upstream location of the control volume are used to solve for the downstream values of  $Z$ ,  $W$ , and  $\theta$ . The downstream values then become the upstream values, and thus the initial conditions for the next volume element.

The initial value of  $H$  is assumed to be 1.35. This value is used to calculate the initial value of  $W$  (1.77). The value of 1.35 is chosen to represent turbulent transition. The transition value of  $H$  is in the range of 1.3 to 1.4. Using  $W$ ,  $a$  and  $b$  are calculated, and used to find  $\theta$ . Since the skin friction coefficient  $C_f$  is known at the entrance, it can be approximated by the following relation to find  $\theta$ . This values serves as an approximation for the initial value of  $Z$ .

$$C_f \approx 2 \frac{a}{b} \left( \frac{\rho_e U_e \theta}{\mu_w} \right)^{0.268}$$

Once the downstream values of  $\theta$ ,  $Z$ ,  $W$  are determined for the last volume element,  $\delta^*$ , is calculated from Equation 2.35. The MFP's throat radius is reduced using  $\delta^*$ , from which an effective throat area is calculated. The ideal mass flow rate through the calibration rig is determined by using the MFP's throat area, and the supply total pressure and temperature. Since the flow is choked at this point, Equation 2.7 is reduced to Equation 2.42.

$$\dot{m}_{ideal} = A_{throat} \frac{P_T}{\sqrt{T_T}} \sqrt{\frac{\gamma}{R}} \left[ \frac{\gamma + 1}{2} \right]^{-\frac{\gamma+1}{2(\gamma-1)}} \quad (2.42)$$

The viscous mass flow rate is finally computed from Equation 2.43 by correcting the calculated mass flow rate from the third pass by the ratio of effective flow area to throat area (minimum geometric area). Finally, the discharge coefficient is determined from Equation 1.1.

$$\dot{m}_{actual} = \dot{m}_{calc} \frac{A_{eff}}{A_{throat}} \quad (2.43)$$

where  $\dot{m}_{calc}$  is the mass flow rate calculated in the third pass.

#### 2.2.4.3 Method of Solution

Several numerical methods are implemented in the analysis to determine the discharge coefficient. The single-variable Newton-Raphson method is used to calculate the entrance Mach number and flow rate of the calibration rig. The multi-variable Newton-Raphson method together with LU decomposition solve the coupled 7 by 7 system to determine the internal flow loss model. Finally, 4th order Runge-Kutta is implemented to solve for the displacement thickness. All of these methods require some initial guess and/or value. The details of these techniques are presented in Appendix A along with the details of the cubic spline interpolation. The interpolation technique is used in a later section [10].

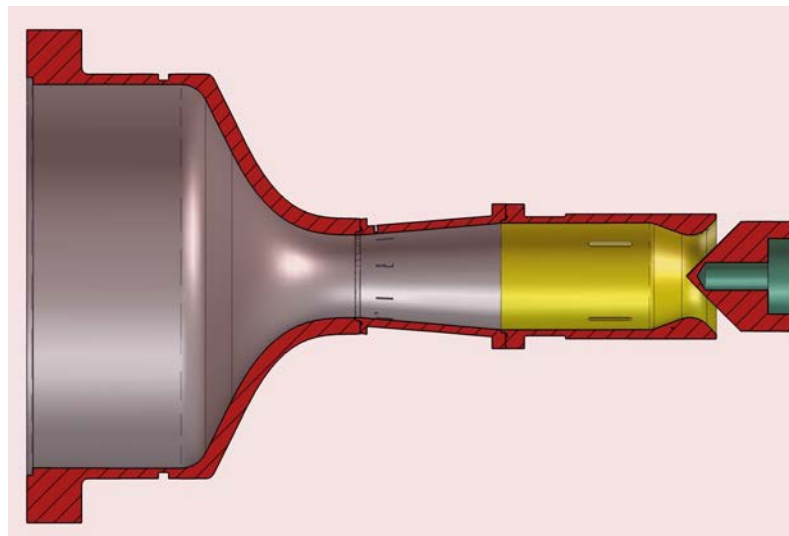
## 2.3 CFD Analysis

Due to the asymmetrical nature of distortion, it is not trivial to create an analysis routine using an axisymmetric, simple control volume method. It is necessary to account for shearing flows with variations azimuthally. Swirl is another phenomenon



that arises. To truly capture the effects of distortion, we resort to CFD to solve for the internal flow in the calibration rig.

It is important to note that the CFD is not capturing all the details of the flow. Only the total pressure is measured and used as a boundary condition. None of the turbulence parameters are known, which are important to truly define the flow. For this reason only profiles which exhibit no flow separation during testing are used in this analysis. The goal of the CFD analysis is to predict a discharged coefficient for the calibration rigs with and without distortion. The results are also used to determine a distortion parameter that characterizes the effects of distortion on the inlet test by Boeing and GRC.



**Figure 2.5:** *Main Components of the N+2 Calibration Rig.*

The first step in the CFD analysis is to create a numerical calibration to serve as a baseline to compare all other results against. The resulting mass flow rate from the numerical calibration is the actual flow rate determined in Section 2.2.4.2. This CFD calibration is compared against the results of the control volume analysis, and actual test data. The comparison is presented in Chapter 4.

A simplified view of the the Boeing N+2 MFP setup of the hardware is presented in Figure 2.5. The initial calibration was performed by Boeing at their facility prior

to testing the inlet shown in Figure 1.1 at GRC. The MFP used in this procedure is a conical plug with a 45 degree angle. The variation of the minimum flow area versus plug position is shown in Chapter 4.

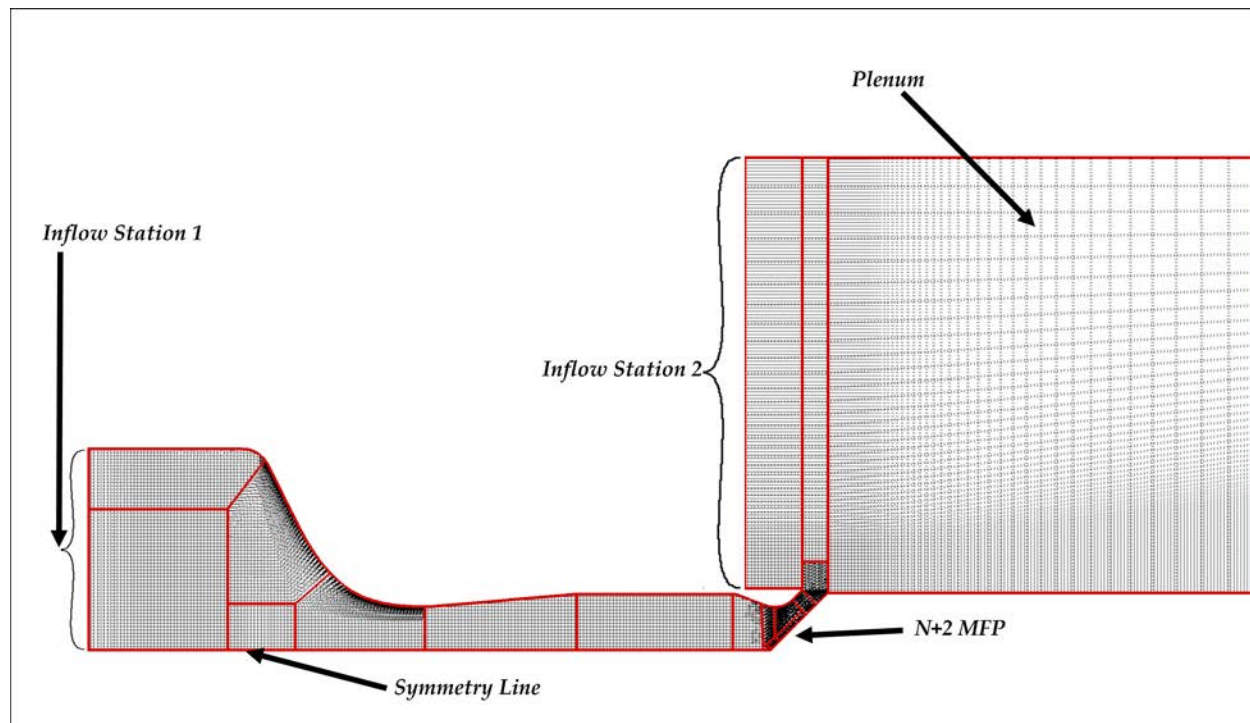
The tool used in the CFD analysis is WIND-US. It is used to numerically solve the Euler and Navier-Stokes equations governing fluid mechanics, along with supporting equation sets governing turbulent and chemically reacting flows. WIND-US has no geometric input, and since WIND-US uses externally generated computational grids, all geometric input and capability depend on the grid generator. The grid generator used in this analysis is Pointwise.

### **2.3.1 Calibration Mesh**

The WIND-US flow simulator provides ample flexibility for both structured and unstructured grids. Grid lines can conform to complex shapes or may pass through regions not in the flow field. The grid may be divided into zones to conform to the geometry better, to allow grid embedding (i.e., zones with finer grids in regions of high gradients like boundary layers), and/or to allow parallel computation. At least 15 grid points are necessary to capture the behavior of the boundary layer.

Only a simple 2-D axisymmetric grid of the geometry is necessary to calculate the discharge coefficient for undistorted flow. The simplified calibration rig CAD assembly shown in Figure 2.5 was imported into Pointwise and stripped of all unnecessary components such as the wall thicknesses and pressure rakes. The pressure rakes are not modeled. A large plenum is added at the MFP exit (shown in Figure 2.6) to simulate outflow to atmosphere.

The spacing between grid points near the surfaces of all the meshes used in this analysis is 0.003 inches. The spacing between points near the symmetry line (shown in Figure 2.6) is 0.047 inches. The distance between each grid point in every zone is automatically computed by Pointwise to match these boundaries. Grid spacing on



**Figure 2.6:** *Mesh of  $N+2$  calibration rig including the plenum.*

each side of a common boundary between zones must be equal to produce a smooth mesh as shown in Figure 2.6. Finer grid spacing near these surfaces appear as a shadow at the wall.

Before running WIND-US the boundary condition at each inflow station must be specified. At inflow station 1, total pressure and temperature are specified. These are constant along the plane to simulate air begin drawn in from a plenum. Each plug position is numerically calibrated at 5 inlet pressures. The details of this analysis are presented in Chapter 4. The Mach number must also be specified; it serves as an initial guess to start the iteration scheme. A Mach number of 0.05 is specified as the initial guess of the entrance Mach number. The boundary condition at inflow station 2 creates the plenum. The freestream static pressure is specified to be atmospheric. A Mach number of 0 will cause the program to run into an error, therefore a total pressure at the inflow station 2 is calculated from Equation 2.9 with a Mach number of 0.05 and the freestream static pressure.

### 2.3.1.1 Turbulence Model

The turbulence model must also be specified. All simulations are run using the Menter Shear Stress Transport (SST) turbulence model [SST]. Previous studies have shown that the SST turbulence model performs well for jet flows [ref]. The SST turbulence model is a robust two-equation eddy-viscosity turbulence model. The model combines the  $k-\omega$  turbulence model and  $k-\epsilon$  turbulence model such that the  $k-\omega$  is used in the inner region of the boundary layer, and switches to the  $k-\epsilon$  in the free shear flow. Both models attempt to provide a general description of turbulence by two transport equations. The first equation is the turbulence kinetic energy while the second is the specific rate of dissipation of turbulence kinetic energy [11].

### 2.3.1.2 Stability Condition

Finally, the program requires a maximum Courant–Friedrichs–Lewy (CFL) number input. It is a necessary stability condition in the numerical analysis of explicit time integration schemes. The CFL is defined in Equation 2.44

$$C = \Delta t \sum_{i=1}^n \frac{u_{xi}}{\Delta x_i} \leq C_{max} \quad (2.44)$$

where

1.  $C$  is the CFL number
2.  $\Delta t$  is the time step
3.  $\Delta x_i$  is the length step in the  $i$  spatial variable. It is not required for the length step to be the same for each spatial variable ( $i = 1, \dots, n$ )
4.  $u_{xi}$  is the magnitude of the velocity in the spatial variable  $i$ .

$C_{max}$  changes depending on the method used to discretized the equations (explicit or implicit).  $C_{max}$  is typically 1 for explicit methods [11].

### 2.3.1.3 Convergence

Convergence is defined when the solution has reached steady state. It is verified by checking whether the mass flow rate is constant along each  $i$  index. If the difference in mass flow rates in each  $i$  index is less than some specified tolerance, the solution has converged. The mass flow is integrated at each  $i$  index across the  $j$  plane (and  $k$  in 3D grids). It is calculated by Equation 2.45 [1]. The final mass flow rate is the average of flow rates between the downstream tangential edge of the radial nose of the MFP and the cold pipe entrance. The result is given in Equation 2.46.

$$\dot{m} = \int_{\theta} \int_r \rho u r dr d\theta \quad (2.45)$$

$$\dot{m} = \frac{\sum_{i=1}^N \dot{m}_i}{N} \quad (2.46)$$

The mass flow sees a spike at the common boundary of each zone, and some initial concern required a closer look at this phenomenon. The concern was that it could cause some delay in convergence, or a false average. This effect was determined to be insignificant, and further details are presented in Chapter 4.

### 2.3.2 Distortion Mesh

The goal of the distortion analysis is to characterize the effect of total pressure distortion on mass flow rate. During the test shown in Figure 1.1 and 1.2, Boeing measured a significant level of total pressure distortion. The total pressure distortion was measured at the AIP. The same distortion profiles are applied as boundary conditions at the AIP to calculate the mass flow rate. However, the test only produces forty data points, which is not enough to create a fine mesh consisting of 4,800 grid points. The data is first spliced by a bicubic interpolation scheme to produce boundary conditions

for the entire AIP (these are the inflow boundary conditions).

Since the boundary condition is applied at the AIP, there is no need to include any geometry upstream of it. Therefore the bellmouth is discarded in the distortion analysis. The grid is created by making a 2-D grid with the desired plug position, and then revolving it around the  $x$ -axis. A 3-D grid is necessary since the applied total pressure distortion profile is not symmetrical. The same surface boundary conditions as in the calibration case are applied at the surface of the mesh.

To reduce computational and convergence time with this mesh, the solution method employed parallel processing along with three levels of grid sequencing. First, a coarse grid sequence included only every fourth point in each direction. Second, a medium grid sequence utilized every other point in each direction. Third, a fine sequence used every grid point in the mesh.

The freestream static pressure this time is calculated from the measured total pressure. Once again, a total pressure is calculated with the wall static pressure to obtain the measured Mach number. The case matrix is found in Chapter 4. Convergence is determined in the same manner as in the calibration case, using Equation 2.46. The supercomputer cluster at NASA Ames was used for all CFD runs.

# Chapter 3

## Experiment

### 3.1 6WB Facility

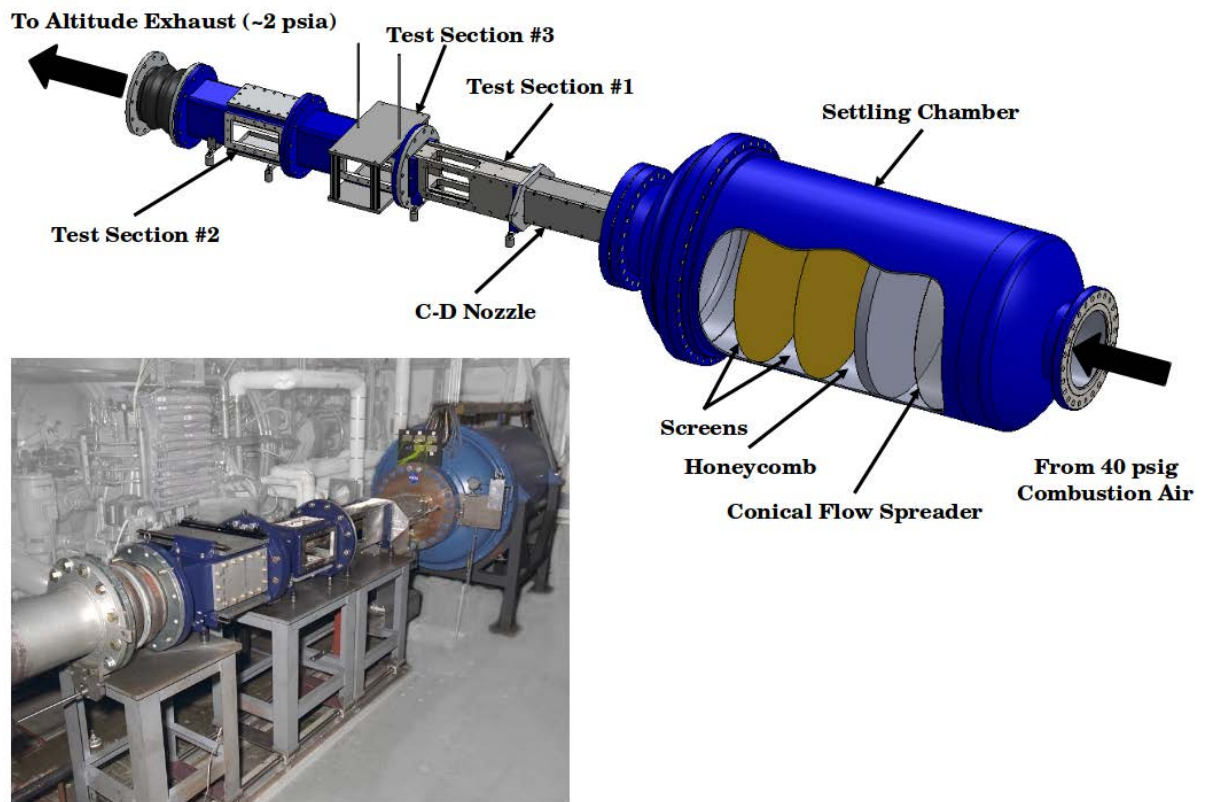


Figure 3.1: 15 by 15 cm SWT facility without experimental hardware.

The objective of the experimental work is to validate the analysis presented in Chapter 2, by testing Boeing’s MFP assembly. The first test is to perform an undistorted flow calibration for comparison to the Boeing experimental calibration, the CFD numerical calibration, and the control-volume method calibration. The second test is to place obstruction devices in the contraction of the calibration rig to create distorted inflow conditions and repeat the calibration procedure. The results are compared to the CFD study of distortion observed during Boeing’s inlet test.

The experimental work was performed using the W6B altitude exhaust system at NASA GRC (shown in Figure 3.1). Three test sections are connected downstream of the nozzle. They are attached to a fixed diffuser which exits to the altitude exhaust system. The altitude exhaust is controlled by the central air system, and can maintain a back pressure vacuum of about 1.75 psia. This is controlled by a remotely actuated facility valve (valve AC040). The facility can handle a maximum flow rate of 25 lb/s.

Data acquisition and recording is via a laboratory standard ESCORT D system. Particular data acquisition capabilities include total and static pressure measurements, temperatures, hot wire anemometry, flow visualization, and laser data techniques. ESCORT also has the capability of evaluating specific parameters and displaying them real-time. Data (both channel and calculated variables) are provided as ASCII comma separated variables (CSV) files [2].

ESP is an off the shelf electronically scanned pressure system. The system consists of numerous 32 port, rack mounted modules of  $\pm 15$  psid, located outside the test chamber. Each module has a check pressure to assure the module is performing correctly and can be calibrated in place using up to 5 highly accurate calibration pressures to maintain the overall system accuracy of  $\pm 0.05\%$  of range. This calibration is automatically performed every hour [12].



## 3.2 Test Setup

The test article assembly is shown in Figure 3.2. The N+2 MFP and the contraction assembly were designed and fabricated by Boeing. The remainder of the components were designed and fabricated specifically for this test. Ambient air is drawn through the ASME nozzle which serves as the primary reference mass-flow measurement device. Further details on the nozzle are provided in Section 3.4.

In this experiment the flow from the ASME nozzle is dumped directly into a settling chamber which acts as a plenum. The intent of the plenum chamber was for the flow through the mixing pipe to settle. The nozzle is directly connected to the settling chamber via an interface flange. An O-ring sitting in a groove on the nozzle's flange creates a seal on the interface flange to prevent and flow leakage. From the settling chamber, the flow passes through a 22:1 contraction and enters the MFP. The plenum attaches directly to the bellmouth. The connecting flange also has an o-ring and connects to the bellmouth with 8 #12 screws. The MFP assembly is held in place via a support structure specifically designed for this experiment.

The MFP assembly consists of a diffuser with an AIP pressure rake at its 1.5 diameter entrance that expands to 1.994 inches. It also has cold pipe of the same diameter with an MFP pressure rake and an contoured exit. The MFP rake is 2 inches from the pipe exit. The 2 inch mass flow plug sits at various positions inside the pipe. The entire test article assembly is mounted on the top window of W6B test section #2 as shown in Figure 3.2. After passing through the MFP, the flow exhausts into the test section which is maintained at approximately 1.75 psia (altitude exhaust). The resultant pressure ratio is 8.22 ensuring a choked MFP.

Since altitude exhaust is the only service required for the experiment, test section # 3 is blanked off with a 12 inch blank pipe flange. The maximum possible flow rate through the test article is approximately 0.6 lb/s for these conditions.

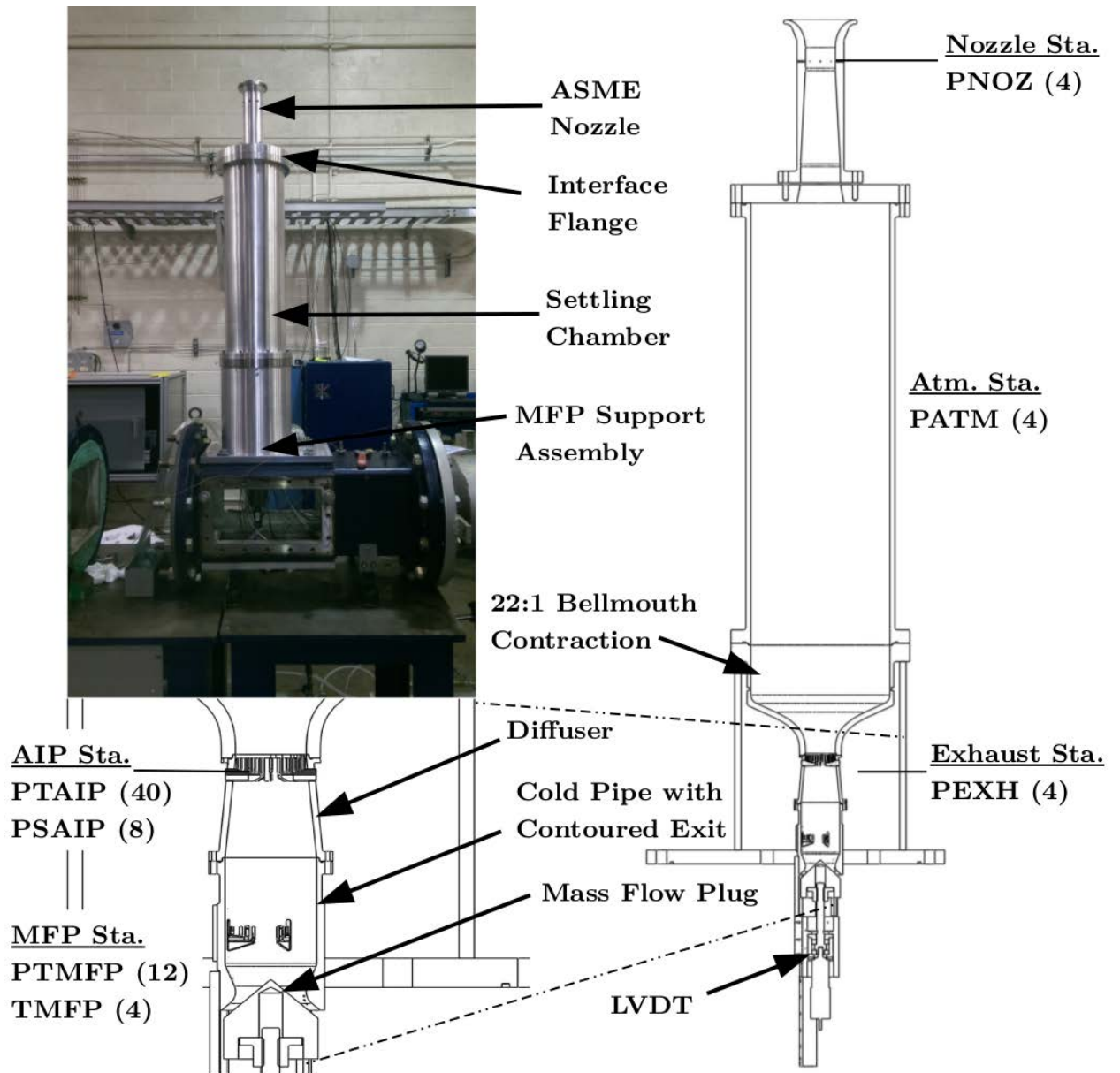


Figure 3.2: Test setup and instrumentation stations.

## 3.3 Instrumentation

### 3.3.1 Stations

The test article is instrumented with steady state instrumentation. The AIP rake has limited dynamic instrumentation, but this was not used during testing. The MFP rake also has four thermocouples. Figure 3.2 shows the instrumentation stations through the test article. Unless otherwise noted, all steady state pressures will be recorded with 15 psia ESP modulus. The uncertainty of all pressure measurements is  $\pm 0.00229$  psi [12].

Electronically scanned modules are differential pressure measurement units consisting of an array of silicon pressure sensors which are electronically multiplexed through an on board multiplexer and instrumentation amplifier. These modules are widely used to measure surface pressure on models and walls of wind tunnels. The ESP modules contain 32 measurement channels connected to pressure ports through small diameter tubing.

Moving from the upstream end to the downstream end, the details of each instrumentation station are as follows:

1. **Atmospheric Station**

Four ESP modules monitor atmospheric pressure in the testing facility.

2. **Nozzle Station**

The ASME nozzle is the primary reference mass-flow measurement device. There are eight equally spaced wall taps located at the throat of the nozzle to measure static pressure. They are shown on the engineering drawing for the nozzle in Appendix C. The taps are connected together in groups of two creating four distinct static pressure measurements. These pressures are measured with four 5.0 psid (referenced to atmosphere) Bell & Howell transducers.

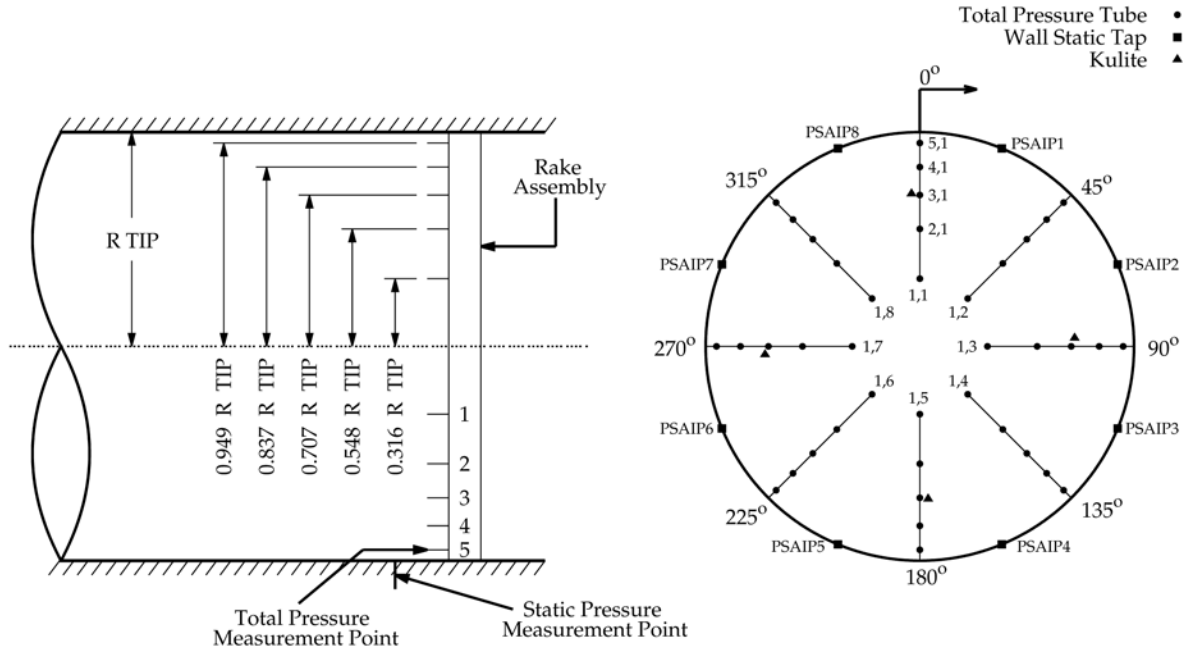
### 3. AIP Station

The AIP rake sits at the entrance of the 1.5 inch diameter diffuser. The rake follows the guidelines established in ARP 1420 to measure total pressure at the AIP [13]. It represents an engine face plane which is defined by the leading edge of the most upstream engine strut, vane, or blade row. The station contains eight equally-spaced rakes with five pitot tubes per rake for a total of 40 total pressures. The pitot tubes are all area-weighted, i.e. the area covered by each ring is the same. Figure 3.3 represents the layout of the rake. The figure shows an upstream view of the rake; it represents the pressure distribution a compressor "sees". The nomenclature used in Figure 3.3 that refers to the individual pitot tubes  $(i, j)$  is per ARP246 [14]. The ring number is defined by  $i$ , and the rake number by  $j$ .

In addition, there are eight a wall static pressure tap located azimuthally midway between the AIP rakes. The rakes and static pressure taps are connected to the ESP modules. Every other rake has one dynamic total pressure transducer for a total of four. These transducers (kulites) are not used during the experiment. They were used during the original Boeing calibration, and the 8x6 ft inlet test. They were left in place for consistency with the previous tests, and to help generate distortion.

### 4. MFP Station

The MFP station records the conditions immediately upstream of the mass flow plug. This station contains four equally-spaced rakes with three pitot tubes per rake for a total of 12 total pressures. These are clocked 22.5 degrees counter clock wise (looking upstream) as to avoid the wakes of the upstream AIP rakes. The tubes on these of rakes are also positioned radially so as to have equal area weighting. There are no wall static taps at the MFP station. The layout of the rake is shown in Figure 3.4 in an upstream view.



**Figure 3.3:** Upstream view of the AIP instrumentation rake.

In addition, each rake contains a single type-K thermocouple in between the first and second pitot tube for a total of four total temperature measurements. The thermocouples produce a voltage output that can be correlated to the temperature that the thermocouple is measuring. The range for type-K thermocouples is between 132 R to 2742 R. The error for these thermocouples is  $\pm 0.75\%$  above 492 R (0 °C) and  $\pm 0.4\%$  below 492 R.

## 5. Exhaust Station

The exhaust station consists of four equally spaced static pressures to monitor the MFP back-pressure and pressure ratio across the MFP.

In total there are 72 steady state pressure readings, and four temperature measurements. The instrumentation takes a reading every second. When data is recorded, the data is averaged over ten seconds to create a single reading of each measurement point.

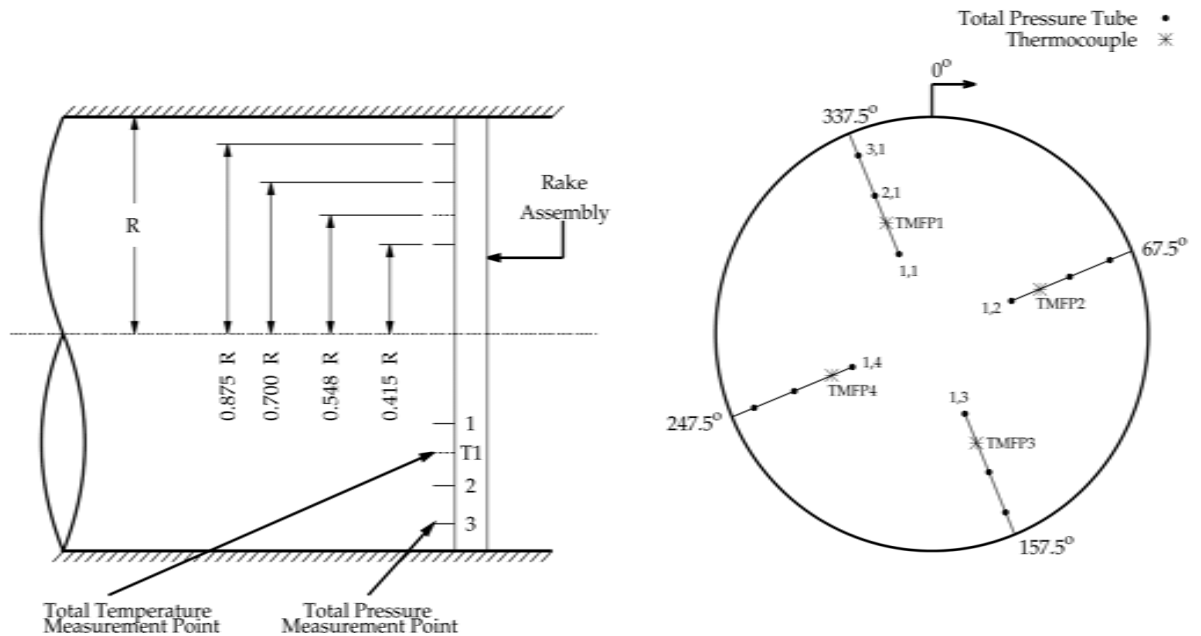


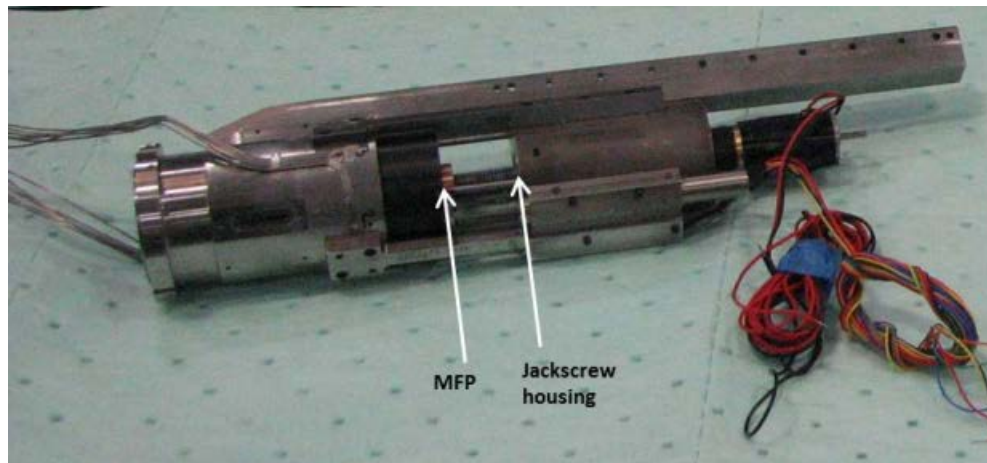
Figure 3.4: Upstream view of the MFP instrumentation rake.

### 3.3.2 LVDT

The MFP has a diameter of 2 inches and a half cone angle of 45 degrees. The cone has a 1 inch length and a shoulder of 1.052 inches. The drive system includes a 24 VDC electric motor with two limit switches. The plug is instrumented with an LVDT which is used to determine the plug position. The jackscrew is 1.75 inches deep into the shoulder of the plug. The LVDT position is calibrated during model installation by setting plug at the full closed limit switch position and measuring the distance between the aft face of the MFP and the jackscrew housing with calipers (Figure 3.5). The plug will then be translated to the full open limit switch position incrementally during testing

## 3.4 ASME Nozzle

The ASME Long-Radius Flow Nozzle is one the most important components of the testing section as it serves two purposes. It draws the fluid into the settling chamber,



**Figure 3.5:** *Mass-flow plug in housing.*

and measures the actual mass flow rate flowing through the MFP. The nozzle generates differential pressure which is used to determine the mass flow rate. The flow rate is corrected by a nozzle discharge coefficient.

The ASME nozzle's shape consists of a quarter ellipse convergence section and a cylindrical throat section. The ellipse is a function of the throat diameter,  $D_{ASME}$ . The major radius is  $2/3$  of  $D_{ASME}$ , and the minor radius equals  $D_{ASME}$ . A throat diameter of 1.5 inches was determined to limit the throat Mach number,  $M_{ASME}$ , to 0.8 at the maximum plug position (i.e. fully open). This is to avoid choking the nozzle and have it limit the mass flow rate instead of the plug. Post manufacturing inspection revealed that  $D_{ASME}$  is exactly 1.500 inches. The uncertainty in the measurement is  $\pm 0.0005$  inches. The nozzle is manufactured out of aluminum with a surface finish of 32 micro-inches.

The advantages of the nozzle over the venturi are its shorter length and lower manufacturing cost. To reduce the permanent head loss, the exit flow does not exhaust into a sudden expansion but rather into a shallow angle ( $7.5^\circ$ ) conical diffuser (recovery cone). In cases operating without a recovery cone, the permanent head loss has been measured up to 40% of the differential pressure [15]. The shallow angle is determined by the ellipse that defines the geometry of the nozzle. A flange at end of

the conical diffuser attaches the nozzle to the rest of the assembly.

With the geometry known, the air flowing through the nozzle can be approximated as an ideal gas. The wall taps measure the differential pressure and determine the static pressure at the throat. They are shown in the engineering drawing provided in Appendix C as well as on the overall system description of Figure 3.2. Using the atmospheric pressure as the total pressure and the measured static pressure, the throat Mach number is calculated from Equation 3.1.

$$M_{ASME} = \sqrt{\frac{2}{\gamma - 1} \left( \frac{P_{T0}}{P}^{\frac{\gamma-1}{\gamma}} - 1 \right)} \quad (3.1)$$

The final parameter needed to calculate the flow rate is the nozzle discharge coefficient. It takes into account any losses due to viscous effects, and permanent head loss. The nozzle is calibrated in the flow lab at GRC to determine a correlation for discharge coefficient based on the throat Reynolds number. The calibration curve and the Reynolds number calculation are presented in Chapter 4. Finally, the mass-flow rate is determined from the Mach number and discharge coefficient where  $A_{ASME}$  is the throat cross-sectional geometric area.

$$\dot{m} = C_D A_{ASME} \frac{P_{T0}}{\sqrt{T_{T0}}} \sqrt{\frac{\gamma}{R}} M_{ASME} \left[ 1 + \frac{\gamma - 1}{2} M_{ASME}^2 \right]^{-\frac{\gamma+1}{2(\gamma-1)}} \quad (3.2)$$

### 3.5 Operation

The maximum pressure ratio (8.22) is used during testing to ensure a hard choked MFP. Thus a single run consists of simply translating the MFP over an axial translation range specified later in this section. A sample of the full test matrix involves a calibration sweep with uniform flow conditions, followed by a number of runs with various distortion generation devices. Before testing any distortion devices, a baseline calibration without any distortion generators is established. The test matrix is seen



in Table 3.1.

### 3.5.1 Baseline Calibration

The calibration begins by positioning the plug 95% of the way forward from the jackscrew housing. The plug is not closed all the way to avoid damaging the MFP or the cold pipe. The back pressure is then dropped to approximately 1.75 psia. The plug is opened by increments of 5% of the closed plug position to measure the mass flow rate at various plug positions. The Mach number at the AIP is monitored during testing and the plug is opened until the Mach number is approximately 0.7 to simulate realistic engine operation. At each plug position the pressure is first allowed to settle for a few seconds before a data sample is recorded. Each sampling records the data over 10 seconds and averages the data to obtain a single reading for each instrument.





### 3.5.2 Distortion Generation





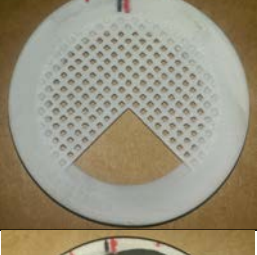

Distortion is created by a ring, rapidly prototyped out of ABS plastic, that fits in the throat of the bellmouth contraction 3 inches above the AIP. Each ring has a mesh that partially covers different sections of the AIP. The mesh wire has a thickness and spacing of 0.125 inches. The settling chamber is lifted with a crane to insert the distortion generator. Each device is tested at three different orientations: 0, 22.5 and 337.5 degrees. The orientation is such that at 0 degrees lines with AIP rake #1. The goal is to create high pressure areas the MFP rakes will be able to capture. Several devices are tested to obtain levels of distortion at the MFP similar to those of the CFD study. The plug position is swept starting from the same position as in the calibration run, however it is stopped when the AIP Mach number is about 0.6. There are two reasons for this lower Mach number; to match the Mach numbers seen in the CFD study and to avoid breaking the mesh and damaging the pressure rakes.

| Date     | Test | Config. | Pressure Ratio | MFP Positions | Duration | Notes                   |
|----------|------|---------|----------------|---------------|----------|-------------------------|
| 09/16/14 | 1    | D0-1    | Max            | 14            | 15 min.  | Baseline Calibration    |
| 09/16/14 | 2    | D1-1    | Max            | 9             | 10 min.  | Device #2, at 0°        |
| 09/16/14 | 3    | D1-1    | Max            | 9             | 10 min.  | Device #2, at 22.5°     |
| 09/16/14 | 4    | D1-1    | Max            | 9             | 10 min.  | Device #2, at 337.5°    |
| 09/16/14 | 5    | D1-2    | Max            | 9             | 10 min.  | Device #3, at 0°        |
| 09/16/14 | 6    | D1-2    | Max            | 9             | 10 min.  | Device #3, at 22.5°     |
| 09/16/14 | 7    | D1-2    | Max            | 9             | 10 min.  | Device #3, at 337.5°    |
| 09/16/14 | 8    | D1-3    | Max            | 9             | 10 min.  | Device #8, at 0°        |
| 09/16/14 | 9    | D1-4    | Max            | 9             | 10 min.  | Device #7, at 337.5°    |
| 09/17/14 | 10   | D0-2    | Max            | 14            | 15 min.  | Baseline Calibration    |
| 09/17/14 | 11   | D1-4    | Max            | 9             | 10 min.  | Device #7, at 0°        |
| 09/17/14 | 12   | D1-4    | Max            | 9             | 10 min.  | Device #7, at 22.5°     |
| 09/17/14 | 13   | D1-5    | Max            | 9             | 10 min.  | Device #8.1, at 0°      |
| 09/17/14 | 14   | D1-5    | Max            | 9             | 10 min.  | Device #8.1, at 22.5°   |
| 09/17/14 | 14   | D1-5    | Max            | 9             | 10 min.  | Device #8.1, at 337.5°  |
| 09/17/14 | 16   | D1-6    | Max            | 9             | 10 min.  | Device #7.1, at 0°      |
| 09/17/14 | 17   | D1-6    | Max            | 9             | 10 min.  | Device #7.2, at 337.5°  |
| 09/17/14 | 18   | D1-7    | Max            | 9             | 10 min.  | Device #8.2, at 0°      |
| 09/17/14 | 19   | D1-7    | Max            | 9             | 10 min.  | Device #8.2, at 22.5°   |
| 09/17/14 | 20   | D1-7    | Max            | 9             | 10 min.  | Device #8.2, at 337.5°  |
| 09/19/14 | 21   | D0-3    | Max            | 14            | 15 min.  | Baseline Calibration    |
| 09/19/14 | 22   | D1-8    | Max            | 9             | 10 min.  | Device #9, at 0°        |
| 09/19/14 | 23   | D1-8    | Max            | 9             | 10 min.  | Device #9, at 22.5°     |
| 09/19/14 | 24   | D1-8    | Max            | 9             | 10 min.  | Device #9, at 337.5°    |
| 09/19/14 | 25   | D1-9    | Max            | 9             | 10 min.  | Device #9.1, at 0°      |
| 09/19/14 | 26   | D1-9    | Max            | 9             | 10 min.  | Device #9.1, at 22.5°   |
| 09/19/14 | 27   | D1-9    | Max            | 9             | 10 min.  | Device #9.1, at 337.5°  |
| 09/19/14 | 28   | D1-10   | Max            | 9             | 10 min.  | Device #12, at 337.5°   |
| 09/19/14 | 29   | D1-11   | Max            | 9             | 10 min.  | Device #7.2, at 337.5°  |
| 10/01/14 | 30   | D0-4    | Max            | 14            | 15 min.  | Baseline Calibration    |
| 10/01/14 | 31   | D1-12   | Max            | 9             | 10 min.  | Device #15.1, at 0°     |
| 10/01/14 | 32   | D1-12   | Max            | 9             | 10 min.  | Device #15.1, at 22.5°  |
| 10/01/14 | 33   | D1-12   | Max            | 9             | 10 min.  | Device #15.1, at 337.5° |
| 10/01/14 | 34   | D1-13   | Max            | 9             | 10 min.  | Device #14.1, at 0°     |
| 10/01/14 | 35   | D1-13   | Max            | 9             | 10 min.  | Device #14.1, at 22.5°  |
| 10/01/14 | 36   | D1-13   | Max            | 9             | 10 min.  | Device #14.1, at 337.5° |
| 10/01/14 | 37   | D0-5    | Max            | 19            | 20 min.  | Baseline Calibration    |

Table 3.1: Test Matrix

Value The rings with just a mesh create low levels of MFP distortion. To create the higher levels observed in the Boeing inlet test, parts of the mesh are blocked with duct tape. The idea is to create a low pressure area and a jet on the opposite side of the ring. The mesh is very thin, and at high speeds it may break and damage the pressure rakes. Duct tape makes the mesh more flexible. Two distortion rings are created that match the high and low pressure regions of AIP distortion observed during the inlet test. One of these rings is shown in Figure 3.6.

| Screen # | Max. MFP Distortion | Screen   |
|----------|---------------------|--|
| 2        | 6.21%               |   |
| 3        | 6.34%               |  |
| 7        | 17.72%              |  |
| 7.1      | 16.21%              |  |

|     |        |  |  |
|-----|--------|--|--|
| 7.2 | 19.62% |    |  |
| 8   | 10.67% |    |  |
| 8.1 | 21.76% |    |  |
| 8.2 | 0.01   |  |  |
| 9   | 18.08% |  |  |
| 9.1 | 28.37% |  |  |




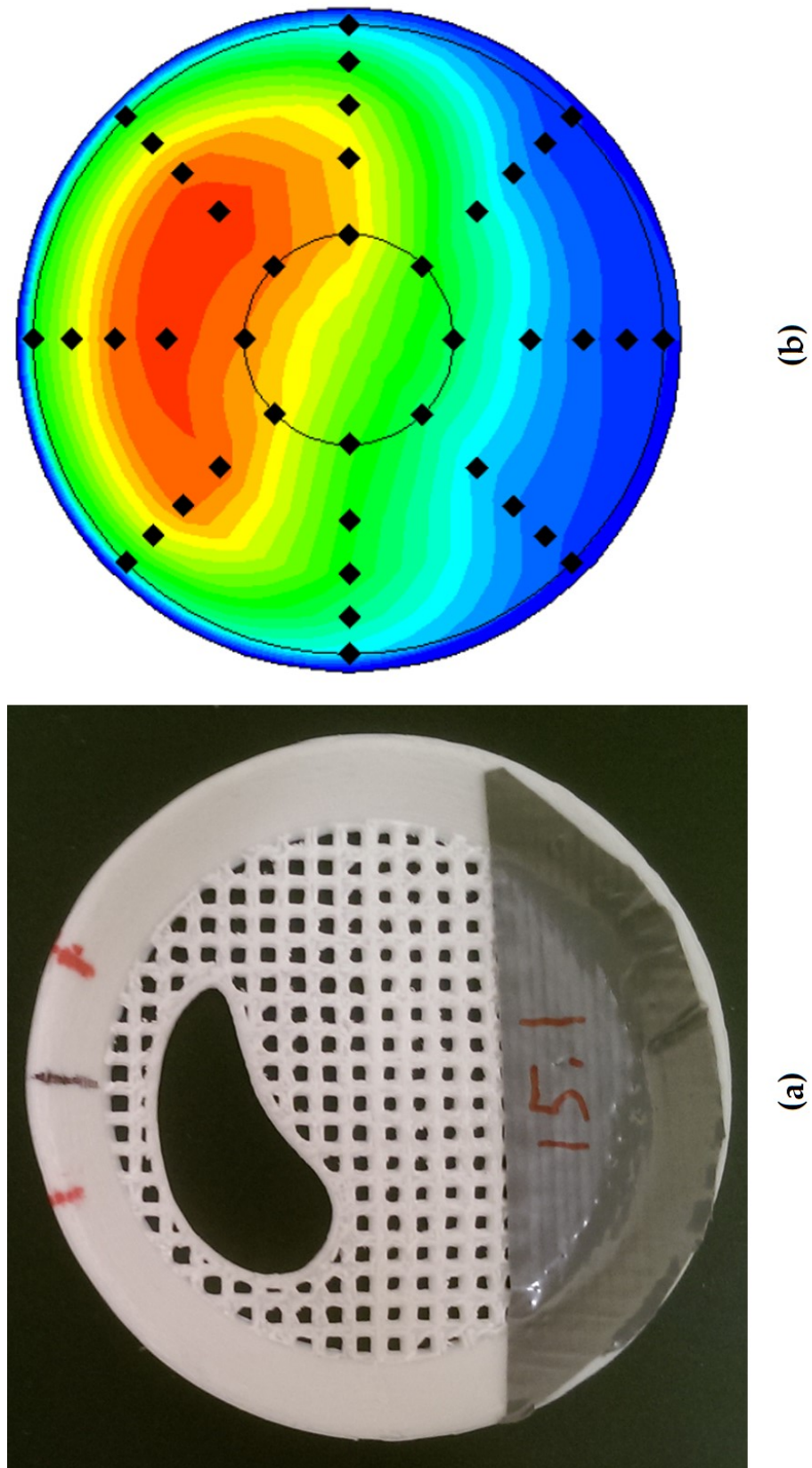
|      |        |   |
|------|--------|---|
| 12   | 5.15%  |   |
| 14.1 | 39.61% |   |
| 15.1 | 37.09% |  |

Table 3.2: Distortion screens.

## 3.6 Uncertainties

Table 3.3 shows a summary of the uncertainties of the various measurement devices. All of these lead to an uncertainty in the calculated and ideal mass flow rate, and discharge coefficient. There is also some uncertainty in the ASME nozzle discharge coefficient. This is by far the largest error and has the most effect on the error calculations presented in Appendix B. The error for various points in this discharge coefficient can be seen in Figure 4.2.



**Figure 3.6:** *Distortion devices modeled after measured AIP profile.*

| Source                               | Value      |
|--------------------------------------|------------|
| ASME throat diameter                 | 0.0005 in  |
| ESP pressure reading                 | 0.0029 psi |
| Differential pressure on ASME nozzle | 0.005 psi  |
| Thermocouples                        | 0.001 R    |
| Plug position                        | 0.001 in   |

Table 3.3: Summary of uncertainties

# Chapter 4

## Results and Discussion

### 4.1 Non-Distorted Calibration

The experiment was performed five times without any distortion devices to produce a baseline calibration using non-distorted flow. The results of this calibration are presented in Figure 4.1 showing the MFP's discharge coefficient,  $C_D$ , and the MFP area ratio,  $AR$ . The area ratio is defined as the throat area determined in Chapter 2 over the cold pipe's maximum cross-sectional area.

$$AR = \frac{A_{throat}}{A_{max}} \quad (4.1)$$

The experimental results are compared against predictions made by the control volume method presented in Chapter 2 and a CFD calibration. The ideal mass flow rate is calculated from the total upstream conditions and the throat area for all solutions. The region of interest in the calibration lies between an area ratio of 0.3 and 0.5. It is in this region that the MFP is used as a flow meter during wind tunnel testing. In this region the maximum deviation of the control volume calculations from the experimental results is 0.54%. The maximum deviation in the CFD results is 1.35%. The maximum experimental error in the operating range is 0.57%. The



locations of these errors are shown in Figure 4.1 by the small arrows. The error analysis is presented in Appendix B. The control volume method is within the error bounds of the experimental data. Both the control volume method and the CFD analysis are within the experimental error in the operating range.

The simple control volume analysis developed from first principals has a higher accuracy than the CFD solution calibration by approximately 0.8%. Figure 4.1 shows the control volume method is a reliable alternative to calibrate a MFP assembly. It also reduces the pre-computational time since no grid is required, only a simple description of the physical geometry. Each CFD solution took about 8 hours to converge using the supercomputer clusters at NASA Ames, while the control volume method took 5 minutes to calculate the calibration curve over the range of MFP area ratios presented.

The actual experimental flow rate is calculated from the ASME nozzle as shown in Chapter 3. The nozzle's discharge coefficient is determined from a metrology calibration. The calibration is presented in Figure 4.2 showing the nozzle's discharge coefficient and the Reynolds number at the throat,  $Re_{ASME}$ . The Reynolds number is computed by the following steps:

1. Static temperature at the throat is determined from Equation 2.10 using the throat's Mach number,  $M_{ASME}$  (determined in Chapter 3), and the total temperature.
2. Density is computed from the static pressure and temperature at the ASME nozzle's throat using the ideal gas law.
3. Velocity is calculated from the throat's Mach number and the static temperature:  $V_{ASME} = \sqrt{\gamma RT} M_{ASME}$ .
4. Viscosity is calculated from the static temperature using Sutherland's law (presented in Chapter 2).

5. Reynolds number is determined from the parameters determined in 2 through 4 and the throat diameter.

The metrology results show a significant amount of scatter, with a maximum deviation of 1.52% at  $Re_{ASME} = 100,000$ , and do not cover the entire range tested during the MFP calibration. The discharge coefficient has a sudden drop for Reynolds numbers lower than 50,000, however no test data is taken below 65,000. A least squares fit is used to determine the discharge coefficient between the minimum and the maximum tested Reynolds number. This curves matches the typical curve of an ASME nozzle drawing air from the atmosphere as shown by the dashed curve in Figure 4.2. The typical wind tunnel test operating range lies in the region calibrated in the metrology lab. The scatter could account for the increased error in the control volume method outside the operating range in Figure 4.1. The maximum error in the control volume method is 1.79%. This maximum error is near the plug’s minimum limit.

Because wind tunnel testing engineers at NASA use the total pressure measured by the MFP rakes instead of the total upstream pressure to calculate a reduced “ideal” flow rate to calculate the discharge coefficient. This discharge coefficient does not account for any viscous losses upstream of the plug. The results of calculating the discharge coefficient with this reduced ideal mass flow rate are presented in Figure 4.3. The figure also includes calibration results performed by Boeing who use the MFP pressures to correct their calibration. The behavior of the curves shown in Figure 4.3 is vastly different than in Figure 4.1. Viscous effects are not prevalent in the operating range, which is not the expected behavior with increasing mass flow rate. Boeing’s calibration is within the experimental error of the new calibration.

The CFD results were calculated for pressure ratios of 1.4 to 5 to create choked and unchoked conditions at the throat. The pressure ratio,  $Pr$ , is defined as the upstream total pressure over the exit back pressure (static). The upstream pressure

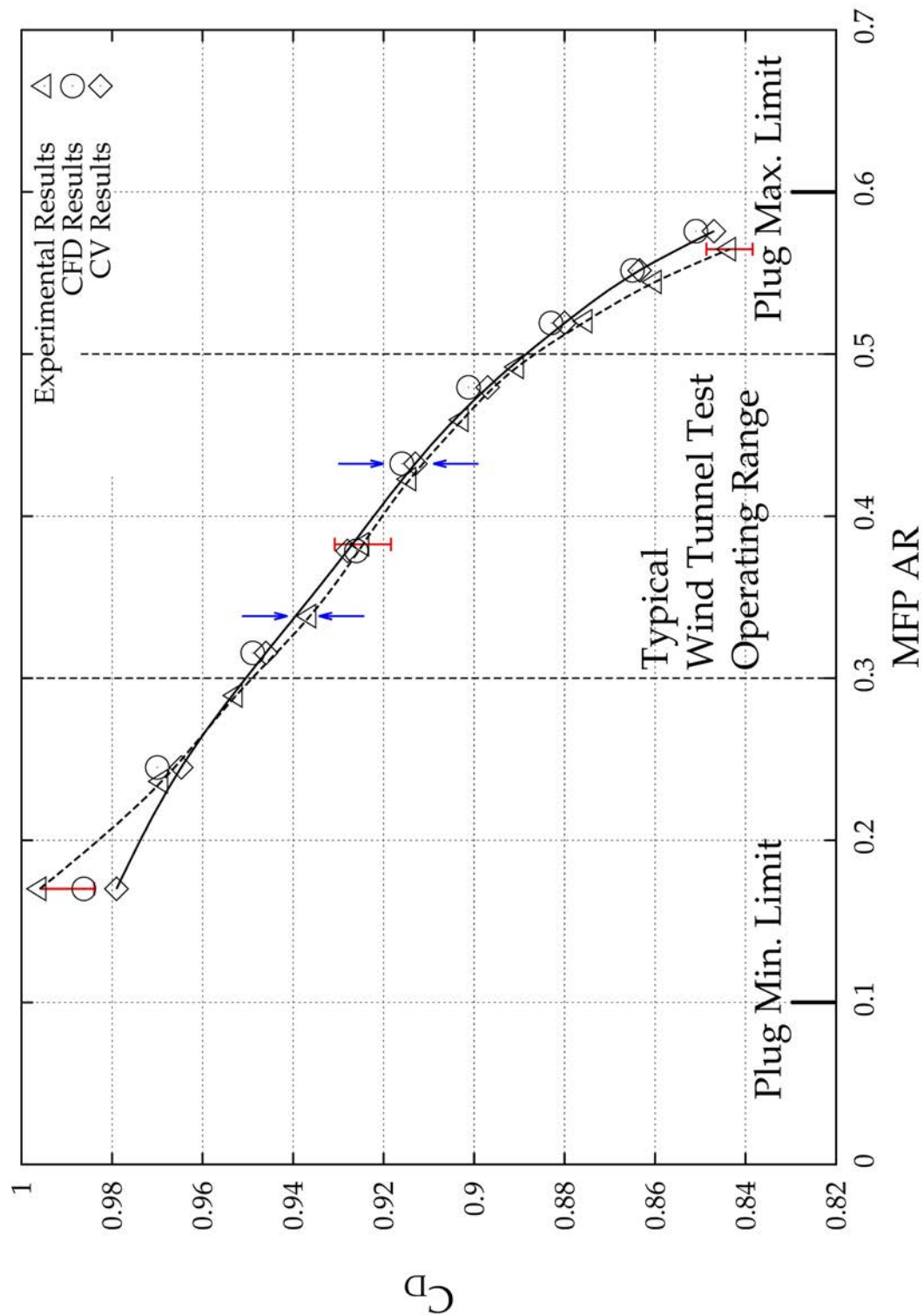


Figure 4.1: MFP discharge coefficient results.

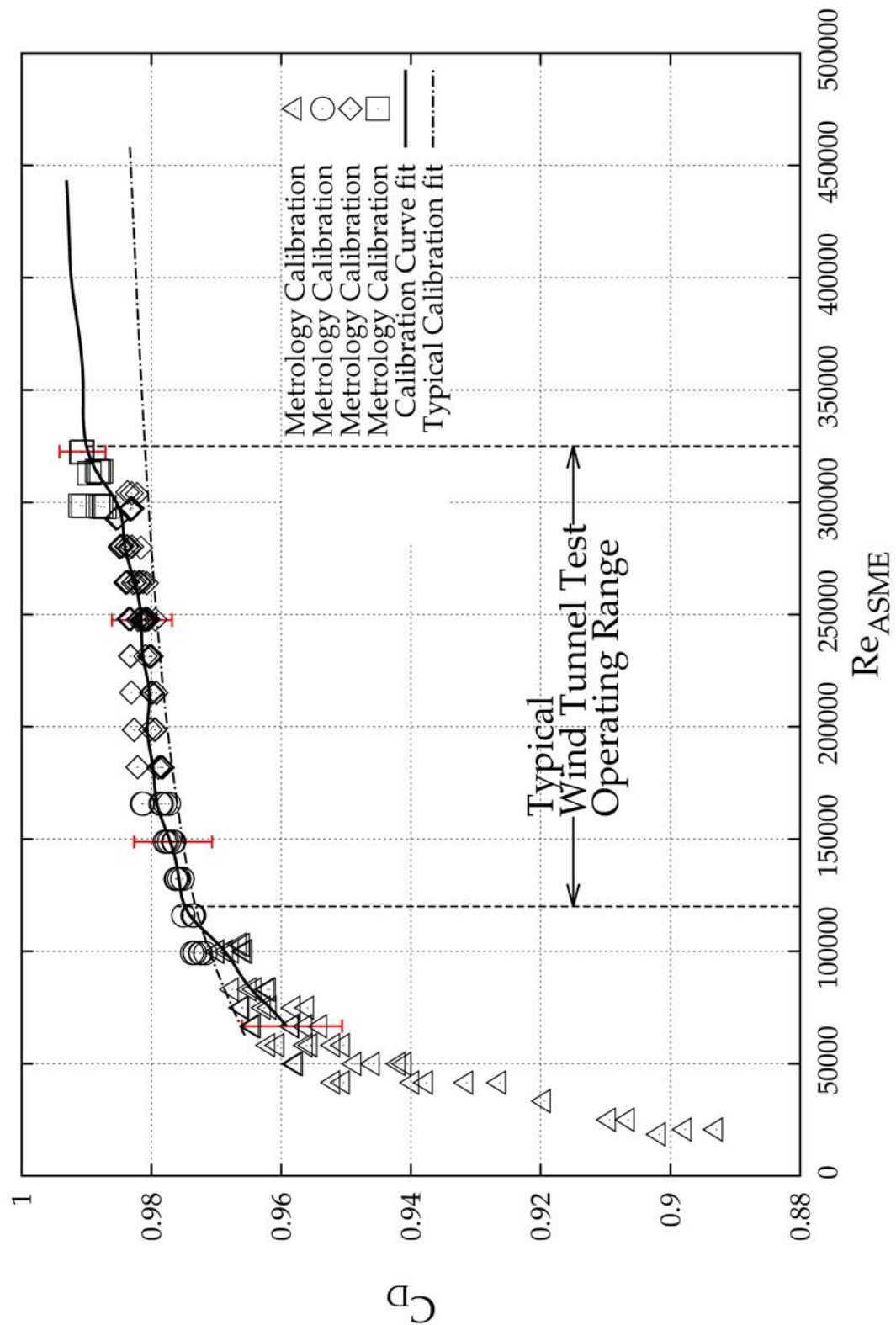


Figure 4.2: *ASME nozzle calibration.*

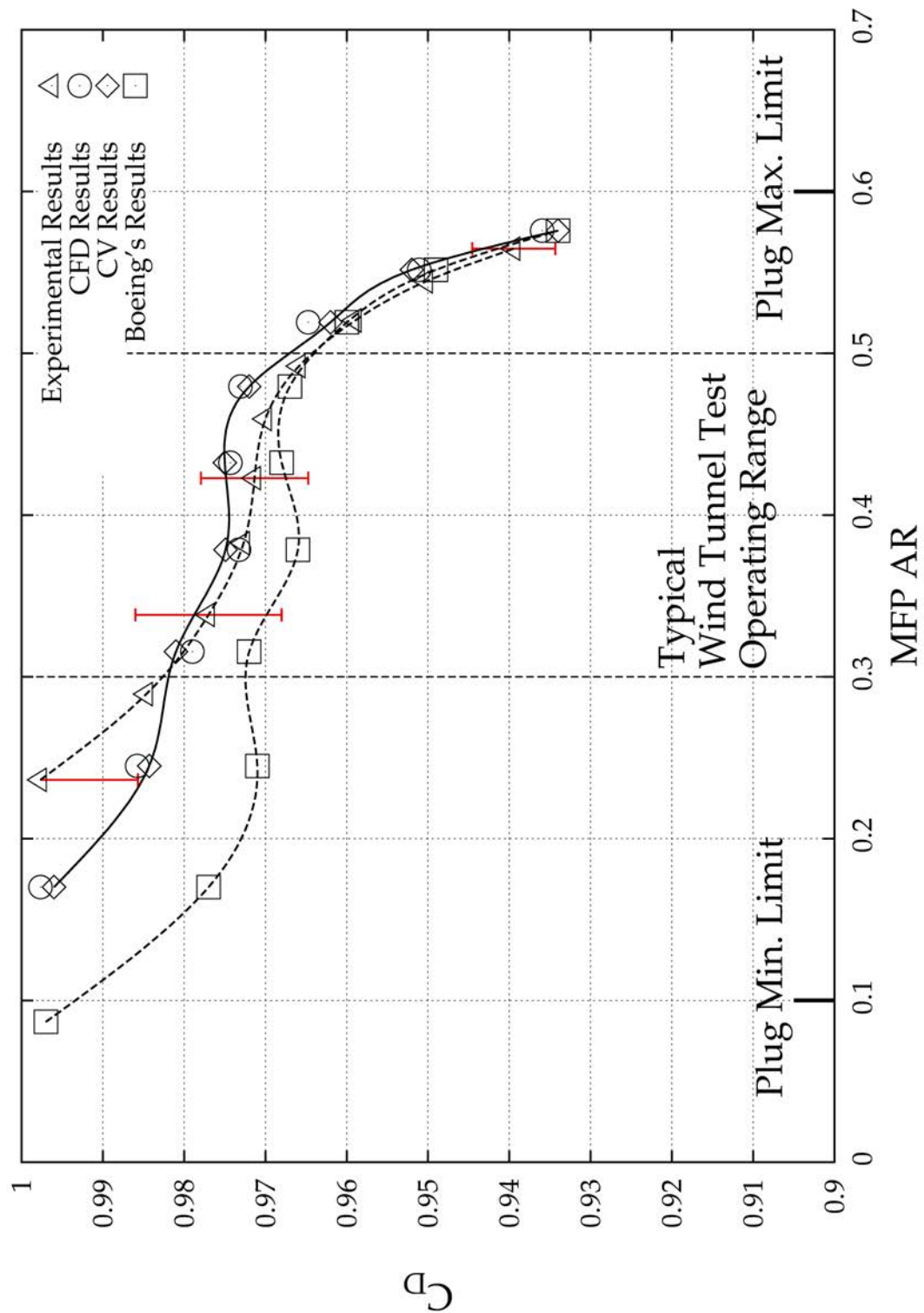
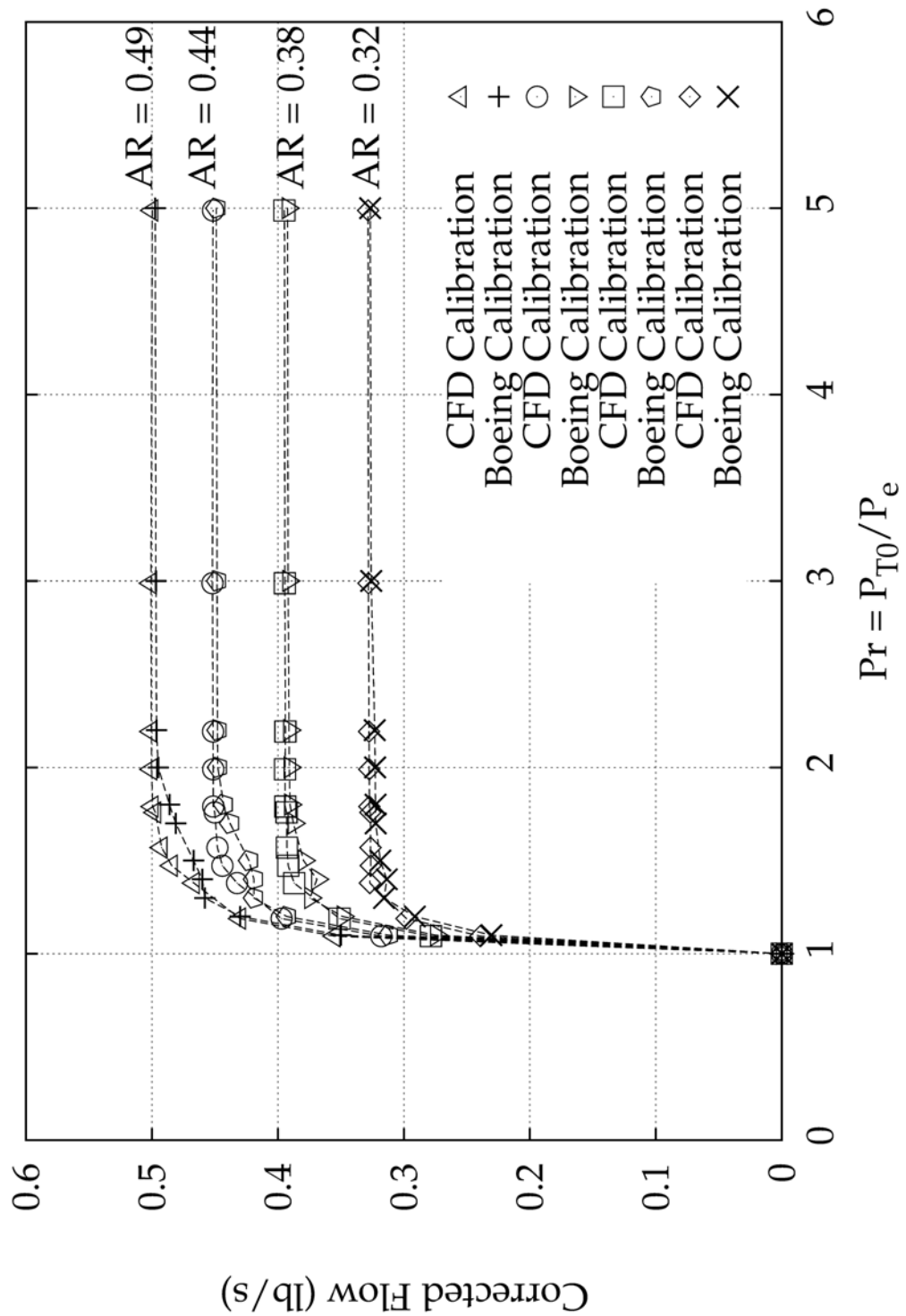


Figure 4.3: *MFP discharge coefficient results with reduced "ideal" mass flow rate.*



**Figure 4.4:** Numerical calibration results at different pressure ratios.

in the CFD calibration was varied from 14.7 to 75 *psia* compared to 14.35 *psia* during the test. The results presented in Figure 4.4 are from a simulation at 75 *psia* and pressure ratio of 5. These results are compared against the calibration performed by Boeing at the same pressure ratios. The curves represent the weighted mass flow rates over the range of pressure ratios at the MFP station for various area ratios.

Corrected flow rate,  $w$ , is the mass flow rate that passes through a device if the inlet pressure and temperature correspond to ambient conditions at sea level on a standard day. The flow is corrected by the pressure and temperature observed at the MFP ( $\theta = T_T/518.7$  and  $\delta = P_T/14.696$ ). There is a minute negative slope to the line due to the slight increase in viscosity with pressure. This result is negligible is does not affect the results significantly.

$$w = \dot{m} \frac{\sqrt{\theta}}{\delta} \quad (4.2)$$

The best agreement between the CFD and Boeing results occurs after a pressure ratio of 2, where the MFP is hard choked. The maximum error in this region is 1.78%. The CFD results are not as accurate for lower pressure ratios which correspond to the transonic region. The CFD overestimates the flow in this region, and the error grows with increasing flow rate (area ratio).

## 4.2 Distortion Description

### 4.2.1 Pattern Descriptors

Distortion is traditionally visualized by plotting total pressure contours at the AIP in polar coordinates  $(r, \theta)$ . The study the the flow behavior as it travels downstream contours are also plotted at the MFP station. Visual patterns are useful to relate the total pressure defect regions to the source of problems in the intake flow. The

experimental and numerical results are presented as pressure contours throughout this chapter. They are always upstream looking, meaning it is the total pressure distribution the engine “sees” approaching the compressor blades. The black diamonds in all of the contours represent the position of each pitot tube probe at the AIP, and MFP station. These are created by cubic spline interpolation of the test data. The pressure is normalized by the upstream total pressure.

### 4.2.2 Numerical Descriptors

Numerical parameters define and correlate the loss of engine performance and stability due to distortion. These parameters describe the radial and circumferential intensities and extents of distortion in quantified terms. For each radial ring of probes, four elements are typically defined as recommended in ARP 1420 [16]:

1. The circumferential intensity element
2. The circumferential extent element
3. The multiple-per-revolution element
4. The radial intensity element

The circumferential intensity ( $\Delta PC/P$ ) element refers to the amplitude of a distortion pattern. It is defined such that the total pressure defect at each radial position is the difference between the average pressure at that radius, or the ring average pressure ( $\overline{P_{T,i}}$ ), and the average minimum pressure at that radius ( $\overline{P_{T_{low},i}}$ ), normalized by the ring average pressure. Positive values of intensity indicate a region where the pressure lies below the face average pressure.

$$(\Delta PC/P)_i = \frac{\overline{P_{T,i}} - \overline{P_{T_{low},i}}}{\overline{P_{T,i}}} \quad (4.3)$$



$$\overline{P_{T,i}} = \frac{1}{2\pi} \int_0^{2\pi} P(\theta)_i, d\theta \quad (4.4)$$

$$\overline{P_{T_{low},i}} = \frac{1}{\theta_i^-} \int_{\theta_{1i}}^{\theta_{2i}} P(\theta)_i, d\theta \quad (4.5)$$

$P(\theta_i)$  is determined from linear fit of the data points in each ring.

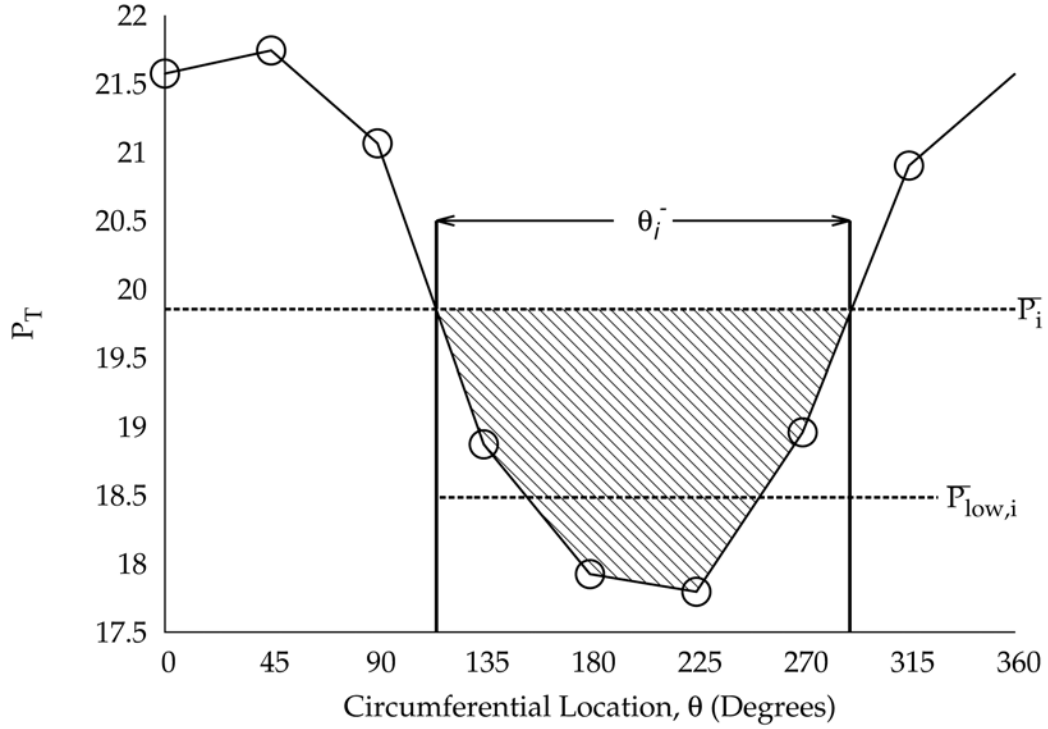
The distortion extent as described by ARP 1420 refers to the circumferential arc size of a distorted region. The circumferential extent for each ring is the angular region, in degrees, in which the pressure is below ring average pressure.

$$\theta_i^- = \theta_{2i} - \theta_{1i} \quad (4.6)$$

The total pressure distortion for the fifth ring of the pattern shown in Figure 3.7 is shown below in Figure 4.6. The graph also shows the low pressure region and the average low pressure of the ring. This pattern is described as a one-per-rev pattern (meaning  $MPR = 1$ ) since it only has one region where the pressure is below the average ring pressure.

The multiple-per-revolution element is a correction term and describes the number of equivalent low pressure regions for each ring. The equivalence is based on the ratio of the total integrated area beneath the average pressure line. It is defined (for  $Q$  low pressure regions) by summing the product of the intensity and the extent of each probe and dividing by the maximum product.

$$(MPR)_i = \frac{\sum_{k=1}^Q \left[ \left( \frac{\Delta PC}{P} \right)_{ik} \theta_{ik}^- \right]}{\left[ \left( \frac{\Delta PC}{P} \right)_{ik} \theta_{ik}^- \right]_{MAX}} \quad (4.7)$$



**Figure 4.5:** *Circumferential distortion.*

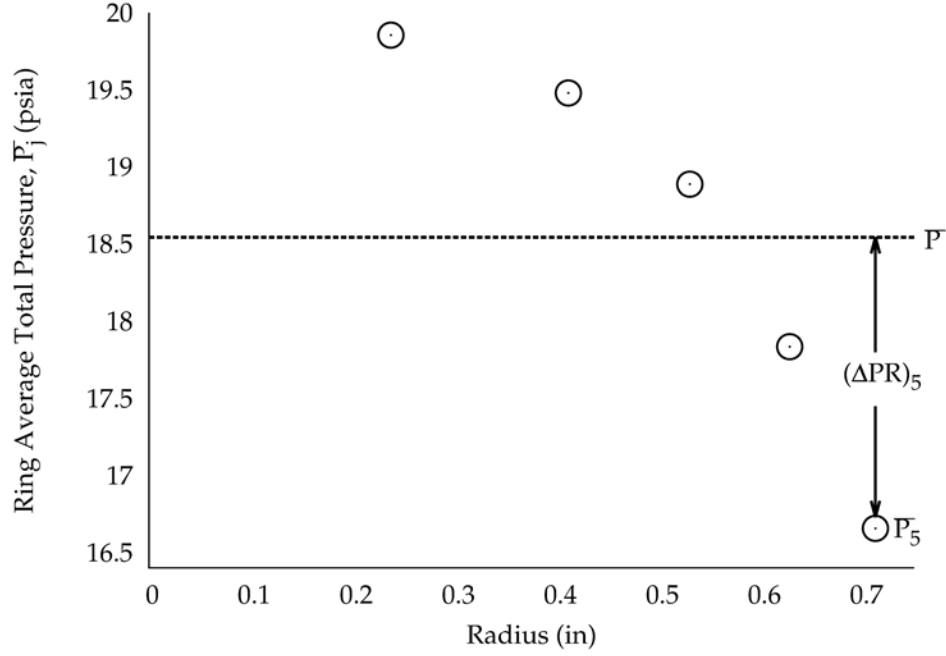
The radial intensity element is defined by the difference between the face average total pressure at the AIP ( $\overline{P_T}$ ) and the ring average pressure, normalized by the AIP average total pressure.

$$\left(\frac{\Delta PR}{P}\right)_i = \frac{\overline{P_T} - \overline{P_{T,i}}}{\overline{P_T}} \quad (4.8)$$

The average total pressure at the AIP is the area-weighted value to be consistent with industry standards and recommendations given in ARP 1420. A positive value represents a ring average pressure that is below the face average.

$$\overline{P_T} = \frac{1}{N} \sum_{i=1}^N \overline{P_{T,i}} \quad (4.9)$$

The above equation assumes that the  $N$  radial rings of probes are located in area-weighted positions. Figure 4.7 is an illustration of the radial distortion of the pattern shown in Figure 3.7.



**Figure 4.6:** *Ring circumferential distortion.*

The distortion intensity elements may be combined to form overall distortion parameters. The resulting parameters are then used to screen inlet distortion data against engine distortion tolerance limits. The required algebra to for some parameters can be very complicated and in some cases expensive to process.

A common descriptor that takes into account both radial and circumferential total pressure distortion is the  $K_{A2}$  descriptor [16]. It is defined as follows

$$K_{A2} = K_{\theta} + K_r \quad (4.10)$$

where  $K_{\theta}$  is the circumferential distortion and  $K_r$  is the radial distortion.

$$K_{\theta} = \frac{\sum_i^N \left[ \frac{1}{r_i} \left\{ \left( \sum_j^M P_T \cos \theta \right)^2 + \left( \sum_j^M P_T \sin \theta \right)^2 \right\}^{1/2} \right]}{\bar{q} \sum_i^N \left( \frac{1}{r_i} \right)} \quad (4.11)$$

$$K_r = \frac{\sum_i^N \left[ \left( \frac{\overline{P_T}}{r_i^{2.8}} \right) \left( \frac{\Delta PR}{P} \right)_i \right]}{\overline{q} \sum_i^N \left( \frac{1}{r_i^{2.8}} \right)} \quad (4.12)$$

where  $\overline{q}$ , the average dynamic pressure, is given by

$$\overline{q} = \frac{\gamma}{2} \overline{P} \overline{M}^2 \quad (4.13)$$

## 4.3 Pressure Decay

### 4.3.1 Non-Distorted Case

Although no distortion devices were used during the baseline calibration, some small amount of total pressure distortion was measured by the AIP and MFP probes. The distortion levels are defined by the difference of the maximum and minimum pressure divided by the average pressure at the corresponding face. This simple descriptor is typically used during inlet testing.

$$DIST = \frac{P_{T,max} - P_{T,min}}{\overline{P_T}} \quad (4.14)$$

The AIP distortion is mostly radial and noticeable every other rake, where the kulites are located. The kulite blockage creates a small low pressure region around the AIP probes. The rest of the flow is unaffected by them. This is shown in Figure 4.7(a) for the non-distorted case with the maximum pressure variation. Total pressure distortion grows downstream and is increased at the MFP due to viscous effects. These effects are evident in Figure 4.7(b) where the total pressure has small radial variations at the MFP station. The small amount of distortion due to the kulites settles downstream and it is not very noticeable at the MFP. Both the AIP and MFP

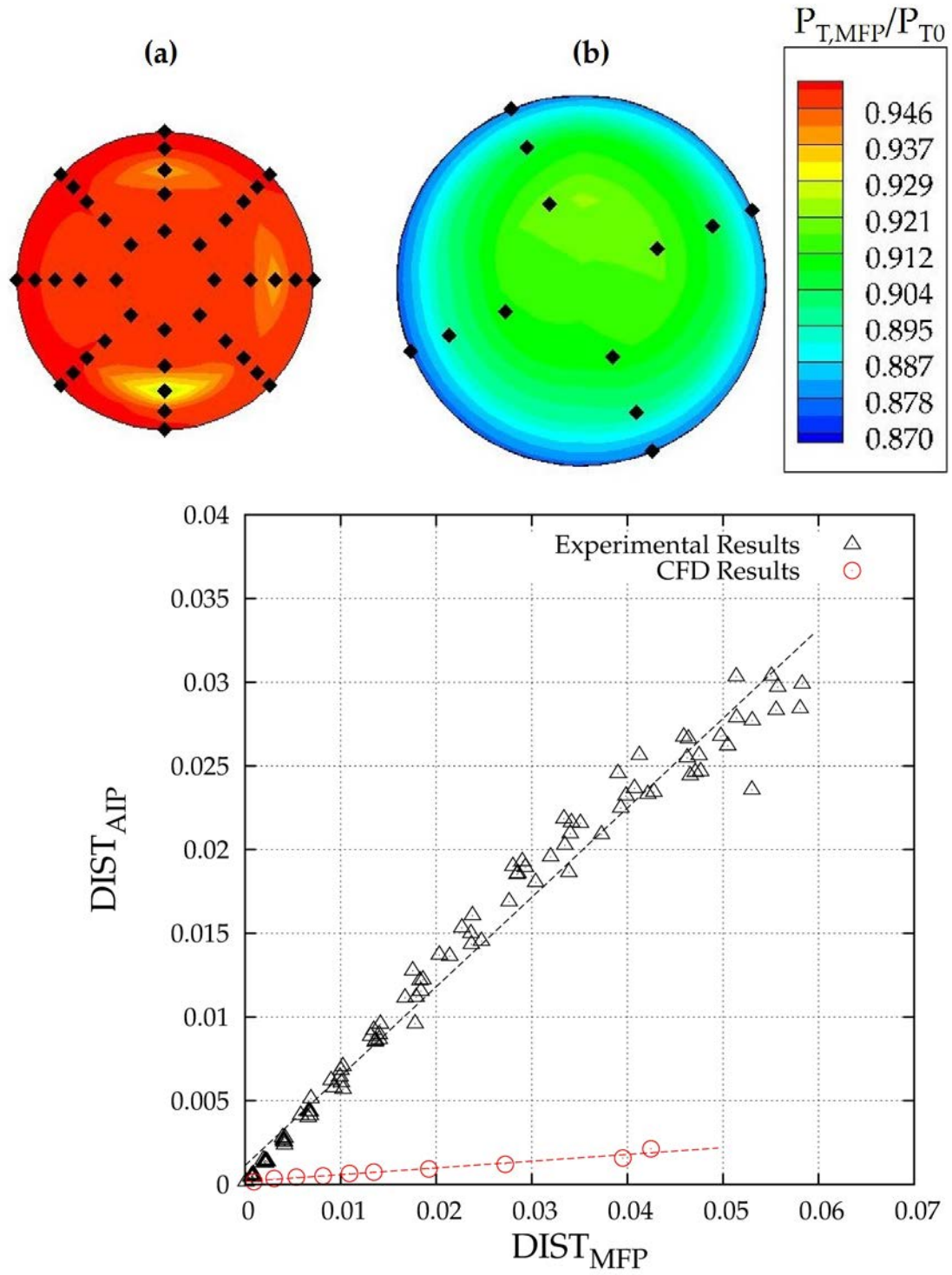
pressure readings are interpolated azimuthally to produce smooth contours.

The results presented in Figure 4.7(c) show the MFP distortion levels increasing linearly as AIP distortion increases. This corresponds to an increase in area ratio as the plug is opened. The CFD results do not detect any significant pressure variations at the AIP. Although the levels at the MFP are higher than the AIP, they are still not comparable to those measured experimentally for a given area ratio. The maximum error in the CFD results is 90%. The CFD results are not reliable in measuring total pressure variations at a given face.

### 4.3.2 Distorted Case

The variation between distortion at the AIP and MFP is presented in Figure 4.8. The CFD distortion is measured by using only the 12 points that correspond to the probes' locations at the MFP station. Experimental distortion tends to decay more rapidly than the CFD would suggest. The CFD solution has a shallower slope and it is not able to accurately predict how well the flow settles downstream. The AIP rakes, which are not modeled in the CFD study, act as crude screens effectively lowering the distortion levels. Increased turbulent mixing in the experiment also lowers the distortion levels. The CFD has no other information on the flow other than the total pressure at the AIP; it does not reflect the turbulence structure, streamwise gradients in the flow nor capture secondary flow component that might be present during inlet testing. The maximum deviation from the experimental values in the CFD results is 33%.

Figure 4.8 also shows the actual MFP distortion levels measured during the inlet test. The CFD model is still not able to accurately predict how well the flow settles compared against the inlet results. The maximum deviation from the inlet test results is lower compared to the new experimental values (16.67%), it is still not a good approximation. These results also include low distortion levels at the AIP



**Figure 4.7:** *Pressure variations in non-distorted calibration.*

not experienced during the inlet test. These levels are similar to those experienced during the test run under non-distorted conditions. In this region the viscous effects dominate and the distortion grows down the MFP.

## 4.4 Distortion Results

To study the effects of total pressure distortion on the MFP calibration a total of 13 different devices were tested to obstruct the flow at the AIP. The experimental results are compared against CFD results. The CFD study consists of 35 different total pressure patterns at the AIP observed during the previous inlet test. The 35 patterns vary over 11 different plug positions. The experiment covers the range of plug positions used for the CFD results. As mentioned previously in Chapter 2, the measured total pressure distribution is used as the upstream boundary condition. Each case takes an average of 50 hours to converge using grid sequencing and parallel processing.

The CFD results are presented in Figure 4.9 as total pressure contours at the AIP and MFP face. Figure 4.9(a) is the pressure profile at the AIP used as a boundary condition. The 40 total pressures and 8 static pressures are used to create 4,800 points for a fine grid. The average of the inner probe ring is used as the center pressure to create the inner region not measured during testing. Figure 4.9(b) is the measured profile at the MFP station during the inlet test. Figure 4.9(c) is the CFD result at the MFP station using all 4,800 points, while Figure 4.9(d) represents a profile created by extrapolating the pressures at the MFP probe locations and interpolating the results.

From (c) it is evident that the cold pipe is not long enough for the flow to settle.. The distortion levels at (b) and (d) are 24.86% and 27.87% respectively. By comparing (c) to (d) it is clear that the MFP rake profile is too coarse and misses a large section of the high pressure region. The MFP rake cannot capture enough points in the high

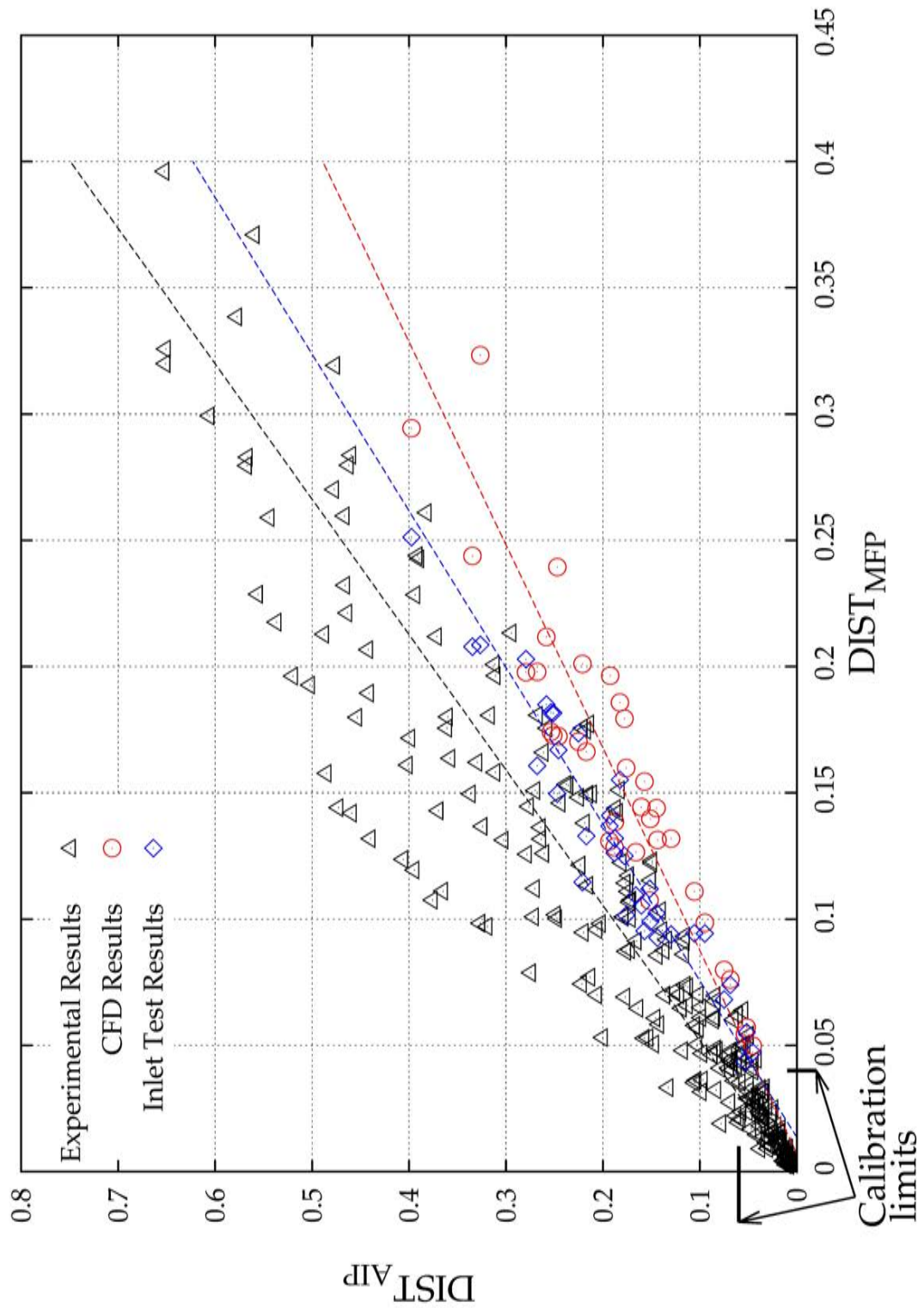


Figure 4.8:  $AIP$  versus  $MFP$  distortion.



pressure region to have a similar distortion levels compared to the full CFD solution. The distortion in (c) is 34.95%.

The result of the MFP rake being too coarse is also observed during the experiment where the same distortion device was tested at three distinct circumferential locations. Although the distortion at the AIP only varied by 5%, distortion at the MFP varied as much as 15% in some cases by changing the orientation of the device at the same plug position. Various devices were tested, each with a different amount of blockage. Higher distortion levels were observed by leaving an open area and blocking another section, creating a high and low pressure region.

Figure 4.10 shows the results of using distortion device #15.1 to recreate a similar distortion pattern observed in Figure 4.9. The low pressure region measured in the experiment is much larger and not comparable to the inlet results. Screen 15.1 is not a good representation of the inlet distortion pattern. Distortion at the AIP varies between 55.58% and 60.57% depending on the orientation. The MFP distortion varies between 22.87% and 37.12%. Both the CFD and inlet test results are in this range of distortion.

The distortion results on all screens are shown in Figure 4.11. The  $y$ -axis is the difference between distorted and undistorted discharge coefficient divided by the undistorted discharge coefficient,  $C_{D,u}$ .

$$\Delta C_D = C_{D,d} - C_{D,u} \quad (4.15)$$

The discharge coefficient is determined by using the upstream pressure to calculate the ideal mass flow rate. The results are compared against the CFD results. For the same range of distortion, the CFD under predicts the mass flow losses.

Although the experimental and CFD trend-lines have a different  $y$ -intercept, they follow the same trend of decreasing discharge coefficient as distortion increases. Distortion is a source of pressure loss and reduces the mass flow rate. There is a significant

amount of scatter in the results shown in Figure 4.11. The distorted behavior depends on the screen used to produce it. The scatter is reduced by looking at each screen individually. It is necessary to take into account the radial and circumferential effects of distortion to classify distortion.

Figures 4.12 through 4.16 represent the results for 5 individual screens and compared to their corresponding CFD solution when applicable. Not all screens match a certain CFD profile. Each figure represents a different mesh at three distinct orientations ( $0^\circ$ ,  $22.5^\circ$  and  $337.5^\circ$ ). The results show that the distorted discharge coefficient is dependent not only on plug position, but also on the individual screens. Each screen has a different distortion pattern which may be defined by the  $K_{A2}$  and DIST descriptors. The results can be used to correct MFP results measured under distortion conditions but calibrated with undistorted flow, such as during Boeing's inlet test.

NASA typically presents distortion results by correcting the flow by the arithmetic average of the total pressure at the MFP station. The pitot tubes are positioned in such a way that the average is area-weighted. The result of this correction is shown in Figure 4.17. The  $y$ -axis shows the difference in weighted flow between the distorted,  $w_d$ , and undistorted cases,  $w_u$ .

$$\Delta w = w_d - w_u \quad (4.16)$$

The difference is normalized by the undistorted weighted flow. Both the experimental and CFD results show a significant amount of scatter around the trend-line. The maximum experimental error in the weighted flow is 0.85%, therefore the trend-line is not very useful. The maximum deviation of the experimental results to the trend-line is 38.35%. Using the trend-line to correct inlet tests is not reliable because of this scatter. Correcting the mass flow rate by the MFP total pressure shows an increase in flow rate, which contradicts the experimental results shown in Figure 4.9.

The MFP is extremely sensitive to distortion levels. The MFP presented in this chapter is a poor design. The straight length segment of the cold pipe is not long enough to allow the flow to settle. Typical MFP configurations use a straight length segment of at least 12 plug diameters to avoid distortion. The straight length segment in this MFP is 3 diameters.

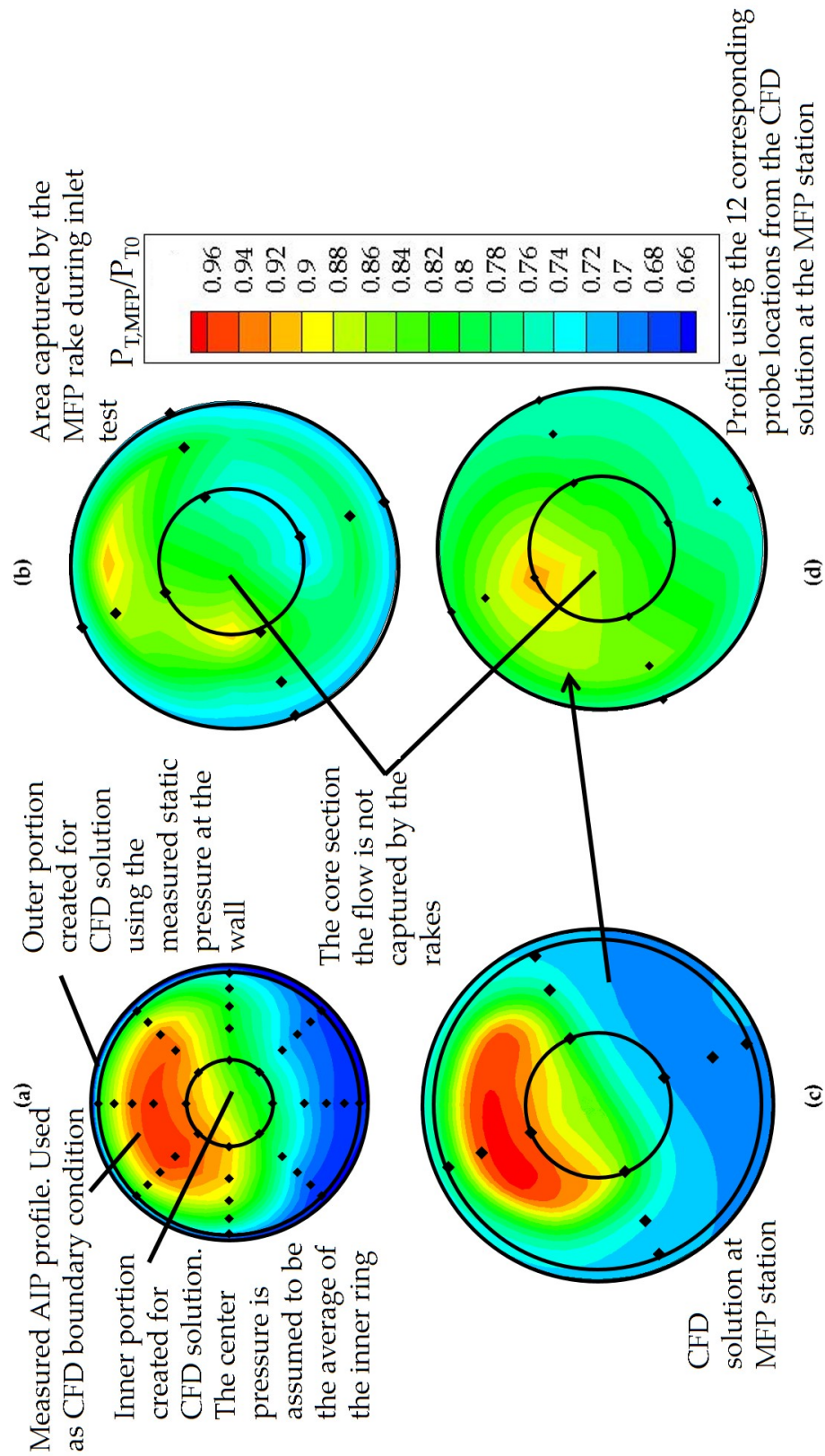
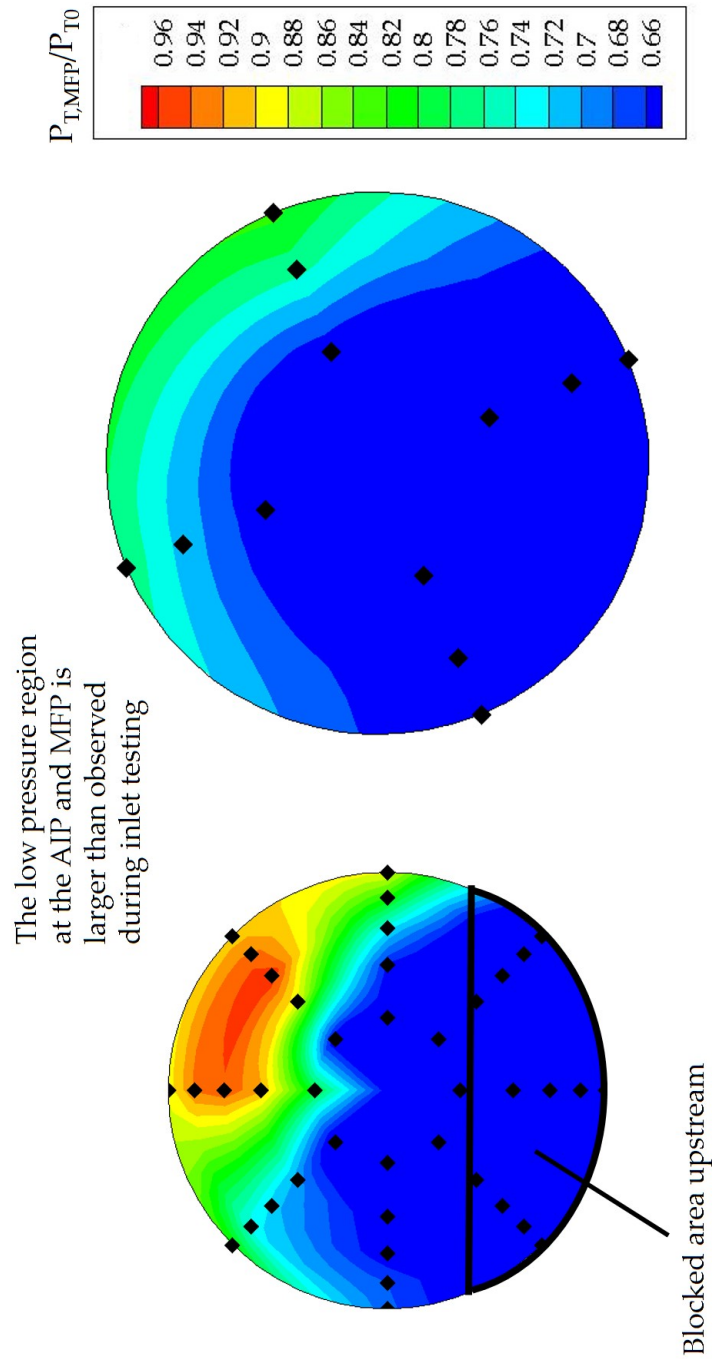
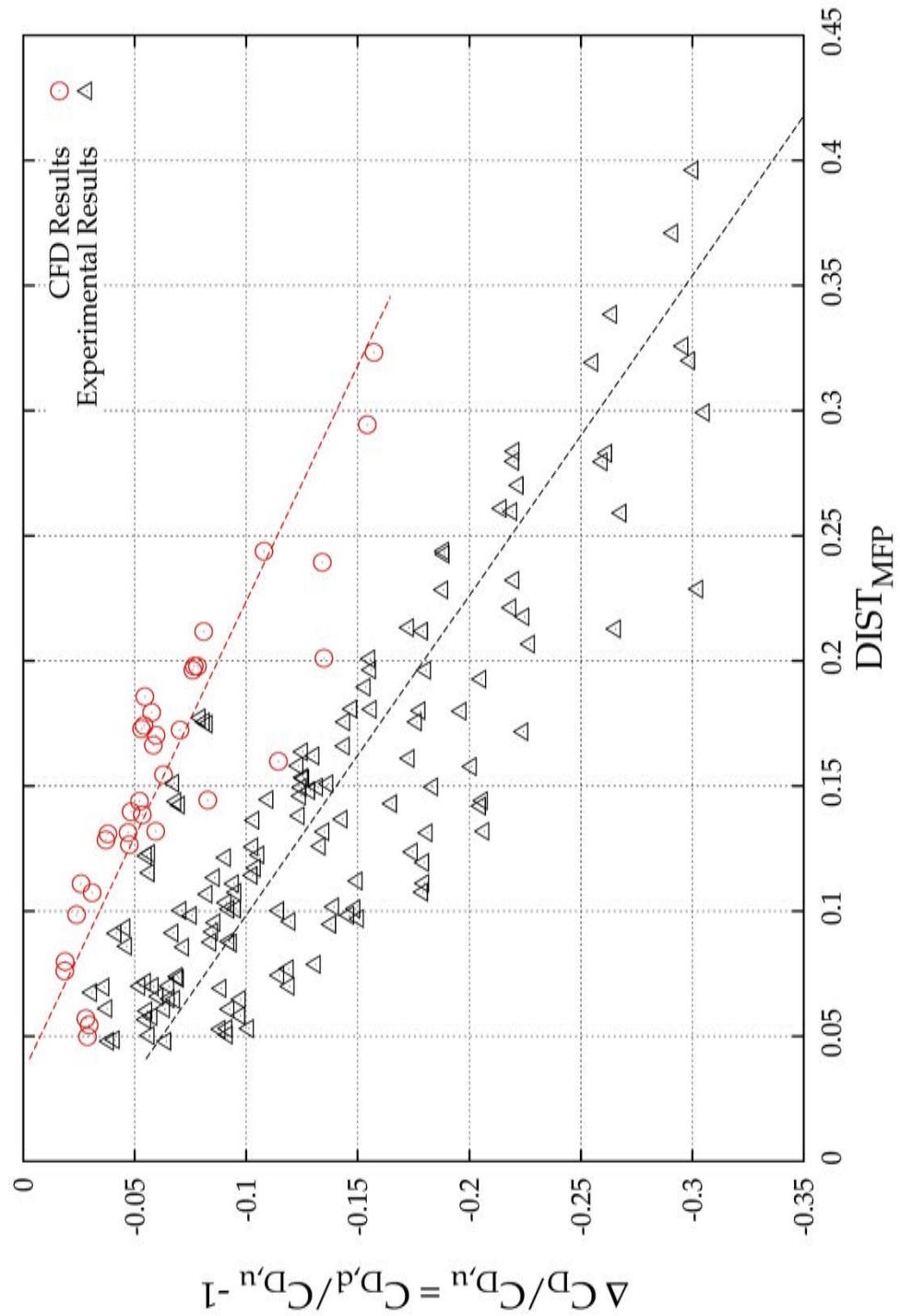


Figure 4.9: Inlet and CFD distortion results.



**Figure 4.10:** *Experimental distortion results for screen 15.1.*



**Figure 4.11:** *Distortion results for all screens.*

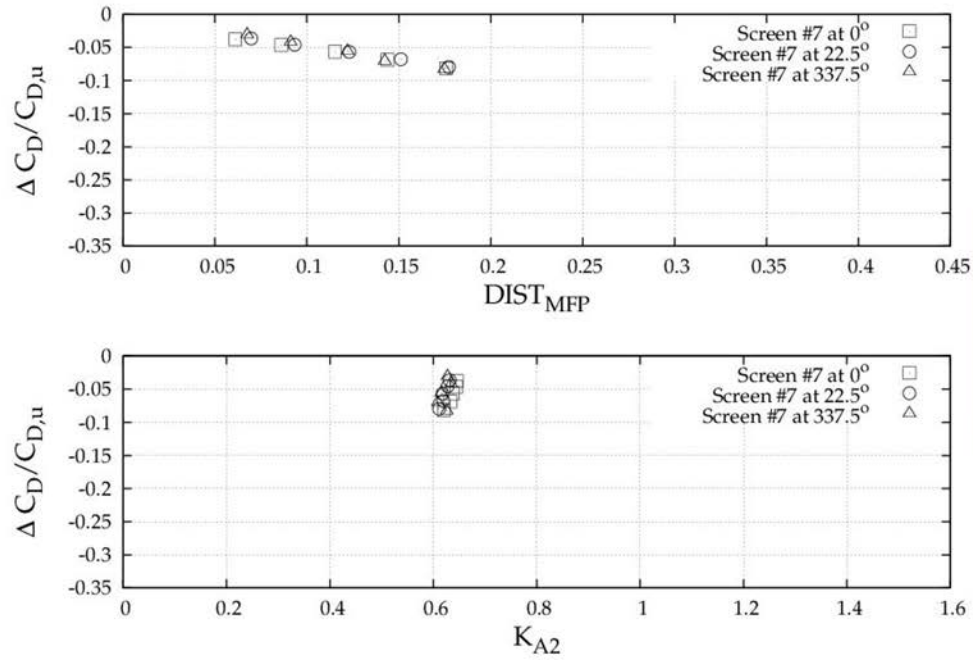


Figure 4.12: Distortion results for screen 7.

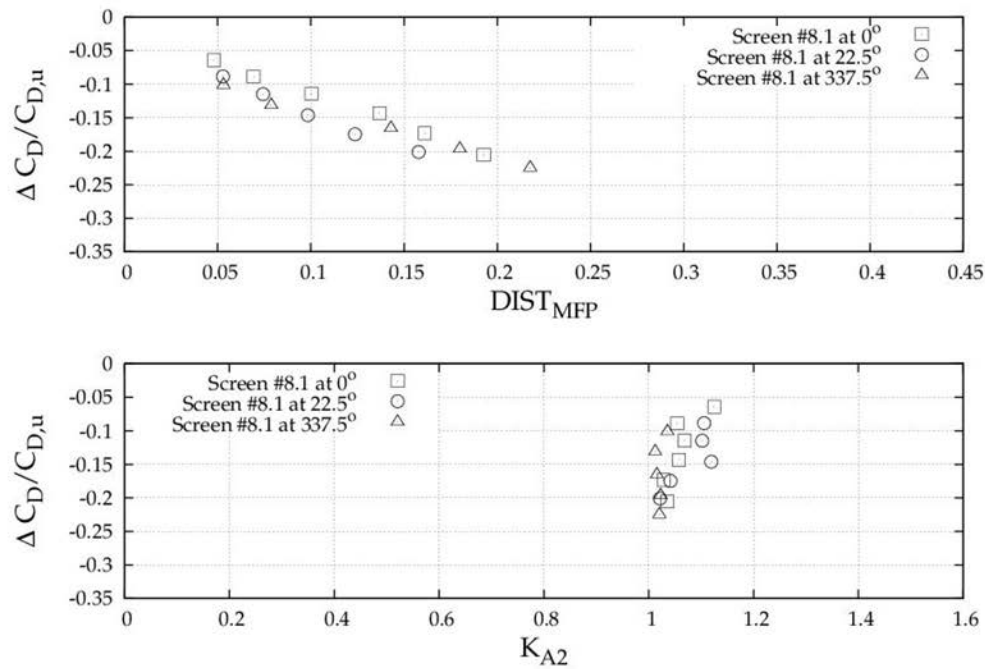


Figure 4.13: Distortion results for screen 8.1.



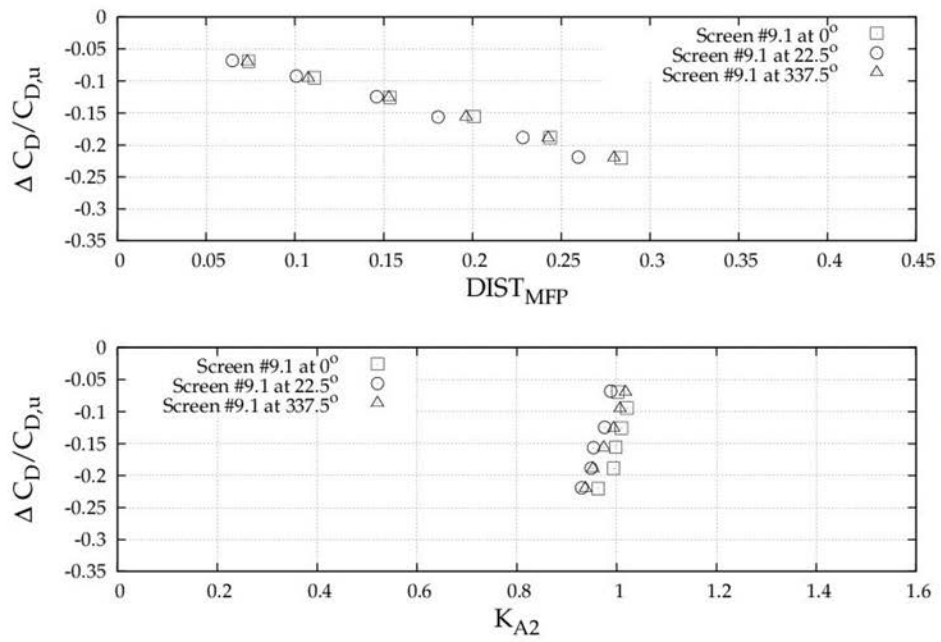


Figure 4.14: Distortion results for screen 9.1.

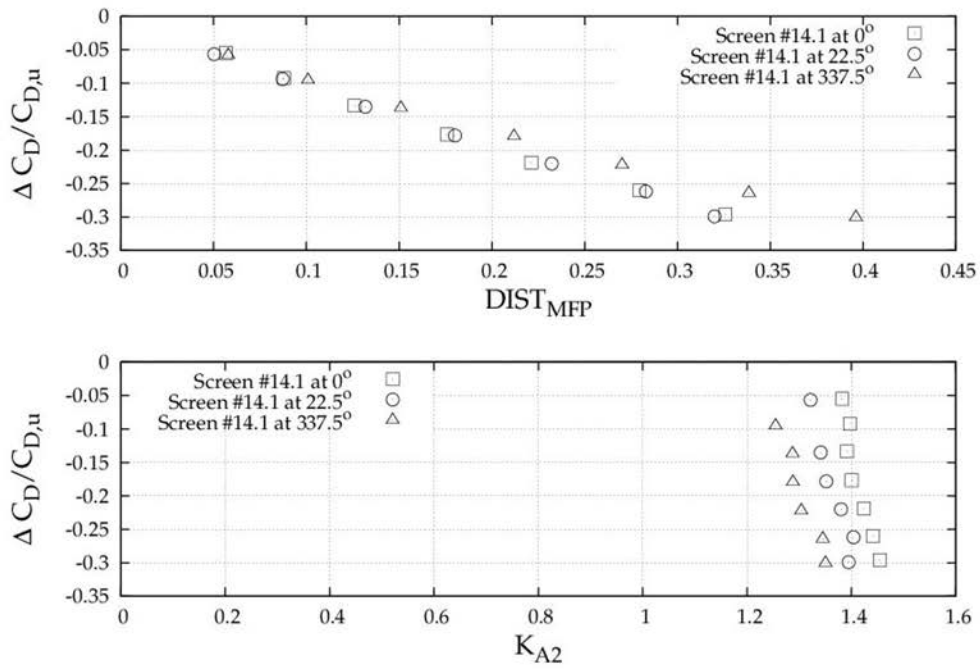


Figure 4.15: Distortion results for screen 14.1.



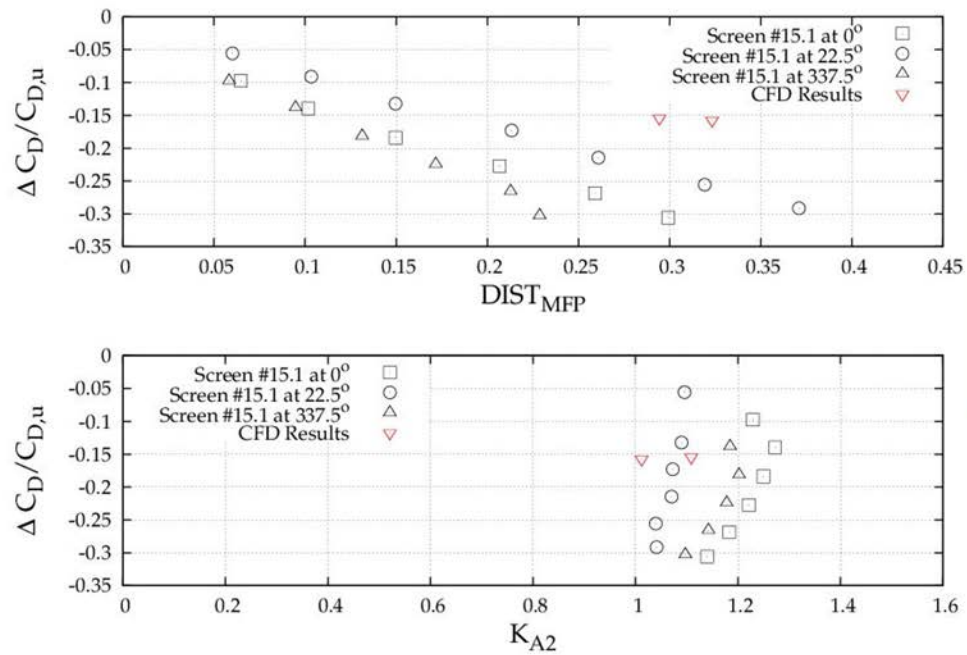
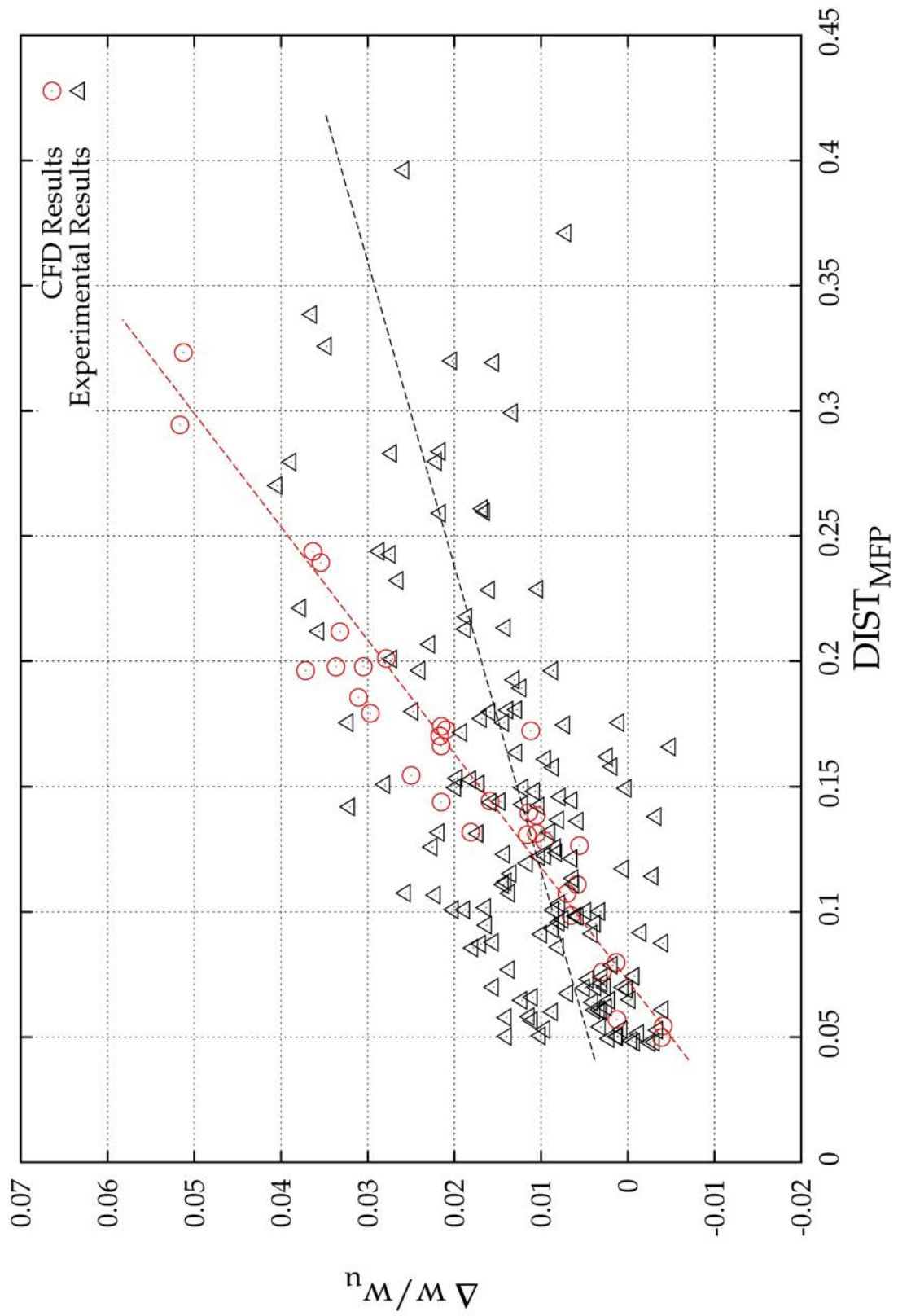


Figure 4.16: Distortion results for screen 15.1.



**Figure 4.17:** Distortion results with weighted flow corrected by MFP pressure.

# Chapter 5

## Conclusion

A simple analytical method of calculating the discharge coefficient,  $C_D$ , for undistorted, axisymmetric flows through a MFP is developed from first principles and verified against experimental results. The control volume method is in excellent agreement with the test data in the typical operating range (with a maximum error of 0.54%) of the MFP. The method allows for rapid the geometric variations of typical mass flow plugs operating under a range of flow rates, pressures and temperatures. It also accurately couples continuity, momentum, energy, an equation of state, and wall shear. The effects of boundary layer growth and the reduction in cross-sectional flow area (characterized by the boundary layer displacement thickness) are calculated using an integral method. The control volume method is of comparable accuracy to the CFD when compared to the experimental results. The maximum error in the CFD is 1.35%. The main advantage of the control volume method is the rapid setup and computational time.

The CFD results are not capable of predicting the pressure decay through the MFP, with a maximum error of 90%. The CFD models are run on the supercomputer cluster at NASA Ames using parallel processing. The control volume requires minimal geometric modeling since no grid is required. Computational time is also reduced by

a factor of 100 for each plug position. The code may be used by experimentalists to accurately calibrate mass flow plugs and other geometries under choked conditions. The control volume method developed is more reliable and easier to use than CFD. It is recommended as a tool to use before developing calibration experiments.

The experimental efforts use a mass flow plug previously employed by Boeing to determine mass flow rate through a low sonic boom inlet. The rig consists of a small diffuser, a straight length segment with a contoured exit for the flow to settle and a plug. The flow through the MFP is measured with an ASME nozzle calibrated by the metrology lab at NASA Glenn. The ASME nozzle calibration was inconsistent at low Reynolds numbers which can be attributed to the larger error in the control volume method outside the operating range.

Total pressure distortion was created at the AIP to quantify its effects on the mass flow rate. Distortion was produced by rapidly prototyped meshes 3 inches upstream the AIP. The discharge coefficient for distorted conditions was as much as 30% lower compared to the baseline calibration. It is shown that deviation in discharge coefficient depends on both the  $K_{A2}$  and DIST distortion descriptors.

The MFP is sensitive to distortion and its effects on the mass flow rate cannot be accurately determined by correcting the flow by the MFP total pressure. The MFP is a flawed design since the straight length segment is too short and does not let the flow to settle. It is only 3 plug diameters in length, while most MFPs are at least 6. A larger straight length segment is recommended in further testing of this MFP. The MFP station rakes are also too coarse and not able to capture all the total pressure variations across the face. In further distortion studies a rake with at least the same amount of pitot tubes as the AIP rake is recommended. The CFD distortion study only showed the general trend in mass flow rate but did not provide any useful insight to classify the distortion. The study uses only total pressure as the upstream boundary condition, which is not enough to define the flow. A better

simulation requires knowledge of the turbulence structure, and a specific distortion pattern over a range of plug positions.

# Appendix A

## Method of Solution

### A.0.1 Single Variable Newton-Raphson Method

The first step of the single variable Newton-Raphson iteration method is to write the governing function in the form left-hand-side = 0. Equation A.41 shows this step, where  $x$  is the variable to solve by iteratively driving the function  $f$  to zero.

$$f(x) = 0 \tag{A.1}$$

An initial guess for  $x$  is required to start the iteration. The function value is checked for convergence (to zero) to within a small numerical tolerance range  $\epsilon$ . This is represented in Equation A.4A. If Equation A.42 is satisfied by the initial value of  $x$ , the solution is converged

$$|f(x)| < \epsilon \tag{A.2}$$

If the solution is not converged, an iteration scheme is required to determine a new value of  $x$ . The iteration scheme is Equation A.43, where  $\Delta x$  is the correction

to be applied to the initial guess of  $x$ .

$$\frac{\partial f}{\partial x} \Delta x \approx f \quad (\text{A.3})$$

The partial derivative for the function can be approximated as a finite difference by Equations A.44 and A.45.

$$\delta = \epsilon x \quad (\text{A.4})$$

$$\frac{\partial f}{\partial x} \approx \frac{f(x + \delta) - f(x - \delta)}{(x + \delta) - (x - \delta)} \quad (\text{A.5})$$

The iteration correction step size is calculated by Equation A.46. The iteration variable is stepped to a new value by Equation A.47. The process is repeated from Equation A.42 until convergence is reached.

$$\Delta x = f / \frac{\partial f}{\partial x} \quad (\text{A.6})$$

$$x = x - \Delta x \quad (\text{A.7})$$

### A.0.2 Multi-Variable Newton-Raphson Method

Similar to the single-variable Newton-Raphson iteration method, the first step in the multi-variable Newton-Raphson iteration method is to write all the governing equations as left-hand-side equal to zero.

$$\begin{aligned}
 f_1 &= (x_1, x_2, x_3, \dots, x_n) \\
 f_2 &= (x_1, x_2, x_3, \dots, x_n) \\
 &\dots \\
 f_n &= (x_1, x_2, x_3, \dots, x_n)
 \end{aligned} \tag{A.8}$$

The functions  $f_i$  are evaluated at the initial guesses for the vector of unknowns,  $x_j$ . The results are then compared against the specified convergence criteria,  $\epsilon$ . If Equation A.9 is satisfied, the solutions are converged and no further iteration is required.

$$|f_i(x_j)| < \epsilon, \quad i = 1, 2, 3, \dots, n \tag{A.9}$$

If the convergence is not met by every function, then an iteration scheme is required to determine the step sizes for each of the unknowns. The iteration scheme is specified by Equation A.10 in matrix notation.

$$\begin{bmatrix} \frac{\partial f_i}{\partial x_j} \end{bmatrix} \begin{bmatrix} \Delta x \end{bmatrix} \approx \begin{bmatrix} f \end{bmatrix} \tag{A.10}$$

Equation A.10 is expressed as Equation A.11 and A.12. In this equation,  $(\begin{bmatrix} \frac{\partial f_i}{\partial x_j} \end{bmatrix})$  is the partial derivative matrix  $[A]$ , and it is used to solve for the column vector  $[\Delta x]$ . The partial derivative matrix is evaluated numerically by a procedure similar given in Equations A.5 and A.6.  $a_{ij}$  refers to elements of  $[A]$ .

$$[A][\Delta x] = [f] \tag{A.11}$$

$$a_{ij} = \frac{\partial f_i}{\partial x_j}, \quad i = 1, 2, 3, \dots, n, \quad j = 1, 2, 3, \dots, n \tag{A.12}$$



The linear system created in Equation A.11 is solved by Lower-Upper decomposition. This procedure is given by Equations A.13 through A.16. Once the corrections  $\Delta x_j$  are determined, the solution is stepped toward convergence by Equation A.17. The procedure is repeated from Equation A.9 until convergence is reached.

$$[A] = [L][U] \quad (\text{A.13})$$

$$[L] \begin{pmatrix} [U][\Delta x] \end{pmatrix} = [f] \quad (\text{A.14})$$

$$[L][y] = [f] \quad (\text{A.15})$$

$$[U][\Delta x] = [y] \quad (\text{A.16})$$

$$x_j = x_j - \Delta x_j, \quad j = 1, 2, 3, \dots, n \quad (\text{A.17})$$

### A.0.3 LU Decomposition

The LU decomposition method is used to solve diagonally-dominant matrix systems. It assumes that  $[A]$  can be decomposed into lower and upper triangular matrices,  $[L]$  and  $[U]$  respectively, as shown in Equations A.13 and A.17.

$$\begin{bmatrix} a_{11} & a_{12} & \cdots & a_{1n} \\ a_{21} & a_{22} & \cdots & a_{2n} \\ \vdots & \vdots & \ddots & \vdots \\ a_{n1} & a_{n2} & \cdots & a_{nn} \end{bmatrix} = \begin{bmatrix} l_{11} & 0 & \cdots & 0 \\ l_{21} & l_{22} & \cdots & 0 \\ \vdots & \vdots & \ddots & \vdots \\ l_{n1} & l_{n2} & \cdots & l_{nn} \end{bmatrix} \begin{bmatrix} 1 & u_{12} & \cdots & u_{1n} \\ 0 & 1 & \cdots & u_{2n} \\ \vdots & \vdots & \ddots & \vdots \\ 0 & 0 & \cdots & 1 \end{bmatrix} \quad (\text{A.18})$$

The details of decomposing  $[L]$  and  $[U]$  and calculating the specific elements are given in Equations A.19 through A.22.

$$l_{ij} = a_{ij} - \sum_{k=1}^{j-1} l_{ik} u_{kj}, \quad j \leq i, \quad i = 1, 2, 3, \dots, n \quad (\text{A.19})$$

$$u_{ij} = \frac{a_{ij} - \sum_{k=1}^{i-1} l_{ik} u_{kj}}{l_{ii}}, \quad i \leq j, \quad j = 2, 3, 4, \dots, n \quad (\text{A.20})$$

$$j = 1, \quad l_{i1} = a_{i1} \quad (\text{A.21})$$

$$i = 1, \quad u_{1j} = \frac{a_{1j}}{l_{11}} = \frac{a_{1j}}{a_{11}} \quad (\text{A.22})$$

The vector  $[y]$  in Equation A.15 is solved by forward substitution using the triangular system. The forward substitution is defined by:

$$y_1 = \frac{f_1}{l_{11}} \quad (\text{A.23})$$

$$y_i = \frac{f_i - \sum_{k=1}^{i-1} l_{ik} y_k}{l_{ii}}, \quad i = 2, 3, 4, \dots, n \quad (\text{A.24})$$

Finally, the correction vector  $[\Delta x]$  is solved by backwards substitution of the triangular system using the intermediate vector  $[y]$ . The backwards substitution is defined by:

$$\Delta x_n = y_n \quad (\text{A.25})$$

$$\Delta x_j = y_j - \sum_{k=n}^{j+1} u_{jk} \Delta x_k, \quad j = n-1, n-2, n-3, \dots, 1 \quad (\text{A.26})$$

### A.0.4 Fourth Order Runge-Kutta

The 4<sup>th</sup> order Runge-Kutta integration technique is used to solved a set of  $N$  coupled first-order ordinary differential equations for the functions  $y_i$ , having the general form

$$\frac{dy_i(x)}{dx} = f_i(x, y_1, \dots, y_n) \quad i = 1, \dots, N \quad (\text{A.27})$$

where the functions  $f_i$  on the right-hand-side are known.

The Runge-Kutta method propagates a solution over an interval by combining the information from several Euler-style steps (each involving one evaluation of the right-hand functions), and then using the information obtained to match a Taylor series expansion up to some higher order.

Initial conditions for the functions must be specified in order for the method to start marching forward. The 4<sup>th</sup> order Runge-Kutta method requires four evaluations of the right-hand side per step  $h$ . The derivative is evaluated at the initial point, twice at trial midpoints, and once at a trial endpoint. The calculations are presented in Equations A.27 through A.30.

$$k_1 = f(x_n, y_n) \quad (\text{A.28})$$

$$k_2 = f\left(x_n + \frac{h}{2}, y_n + \frac{k_1}{2}\right) \quad (\text{A.29})$$

$$k_3 = f\left(x_n + \frac{h}{2}, y_n + \frac{k_2}{2}\right) \quad (\text{A.30})$$

$$k_4 = f(x_n + h, y_n + k_3) \quad (\text{A.31})$$

From these derivatives the final function value is calculated.

$$y_{n+1} = y_n + \frac{h}{6}(k_1 + 2k_2 + 2k_3 + k_4) \quad (\text{A.32})$$

The value of  $x$  is marched forward by the small step  $h$ .

$$x_{n+1} = x_n + h \quad (\text{A.33})$$

The solution keeps marching forward until the desired value of  $y$  is reached. The Runge-Kutta method treats every step in a sequence of steps in an identical manner. Prior behavior of a solution is not used in its propagation. Mathematically it agrees with the behavior of ordinary differential equations; any point along the trajectory of an ODE can serve as an initial point.

### A.0.5 Bicubic Spline Interpolation

The goal of the cubic spline interpolation is to get an interpolation formula that is smooth in the first derivative, and continuous in the second derivative, both within an interval and at its boundaries. Equation A.34 states the main relation that accomplishes this goal (for  $j = 2, \dots, n-1$ ).

$$\frac{x_j - x_{j-1}}{6}y''_{j-1} + \frac{x_{j+1} - x_{j-1}}{3}y''_j + \frac{x_{j+1} - x_j}{6}y''_{j+1} = \frac{y_{j+1} - y_j}{x_{j+1} - x_j} - \frac{y_j - y_{j-1}}{x_j - x_{j-1}} \quad (\text{A.34})$$

Since Equation A.34 provides  $n-2$  linear equations in the  $N$  unknowns  $y''_i$ ,  $i = 1, \dots, n$ , the boundary conditions at  $x_1$  and  $x_n$  must be specified. The natural cubic spline is specified setting both  $y''_1$  and  $y''_n$  equal to zero. Equation A.34 and the boundary conditions are not only a linear equation, but also tridiagonal. Each  $y''_j$  is coupled only to its nearest neighbors at  $j \pm 1$ . Therefore, the system of equations

can be solved by  $O(n)$  operations by a tridiagonal algorithm.

Equations A.35 through A.39 the decomposition of the tridiagonal system and Equation 2.80 is the backward substitution. The decomposition and substitution implemented in this section is similar to the LU decomposition.

$$\sigma = \frac{x_i - x_{i-1}}{x_{i+1} - x_{i-1}} \quad (\text{A.35})$$

$$p = \sigma y''_{i-1} + 2 \quad (\text{A.36})$$

$$y''_i = \frac{\sigma - 1}{p} \quad (\text{A.37})$$

$$u_i = 6 \frac{\frac{y_{i+1} - y_i}{x_{i+1} - x_i} - \frac{y_i - y_{i-1}}{x_i - x_{i-1}}}{x_{i+1} - x_{i-1}} - \sigma \frac{u_{i-1}}{p} \quad (\text{A.38})$$

$$y''_k = y''_k y''_{k+1} + u_k \quad (\text{A.39})$$

$$i = 2, \dots, n-1 \quad k = n-1, n-2, \dots, 1$$

$$u_i = u_n = 0$$

Although the process above describes interpolation in one-dimension, it is possible to use it as a bicubic spline on an  $m$  by  $n$  tabulated function. In this case,  $m$  one-dimensional splines are performed across the rows of the table, followed by one additional one-dimensional spline down the newly created column.

# Appendix B

## Uncertainty Analysis

If  $z$  is a function of  $x$  and  $y$  ( $z = f(x, y)$ ), then the error of  $z$  depends on the error in  $x$  ( $\Delta x$ ) and  $y$  ( $\Delta y$ ). The error of  $z$  is

$$\Delta z^2 = \left( \frac{\partial f}{\partial x} \right)^2 \Delta x^2 + \left( \frac{\partial f}{\partial y} \right)^2 \Delta y^2 \quad (\text{B.1})$$

This equation is used to find the experimental error in the discharge coefficient. The error in the measured flow rate is

$$\begin{aligned} \Delta \dot{m}_{actual}^2 = & \left( \frac{BC_D A}{\sqrt{T_T}} \right)^2 \Delta P_T^2 + \left( \frac{BC_D P_T}{\sqrt{T_T}} \right)^2 \Delta A_{ASME}^2 \\ & + \left( \frac{BP_T A}{\sqrt{T_T}} \right)^2 \Delta C_D^2 + \left( \frac{BC_D A P_T}{2T_T^{3/2}} \right)^2 \Delta T_T^2 \end{aligned} \quad (\text{B.2})$$

where B equals  $\sqrt{\frac{\gamma}{R}} \left( \frac{\gamma+1}{2} \right)^{-\frac{\gamma+1}{2(\gamma-1)}}$ .

The error in the ASME nozzle throat area is

$$\Delta A_{ASME}^2 = \left( \frac{\pi D_{ASME}}{2} \right)^2 \Delta D_{ASME}^2 \quad (\text{B.3})$$

The error in the discharge coefficient depends on the error in the actual flow rate and the error in the MFP throat area.

$$\begin{aligned} \Delta C_D^2 = & \left( \frac{\sqrt{T_T}}{P_T A_{throat} B} \right)^2 \Delta \dot{m}_{actual}^2 + \left( \frac{-\dot{m}_{actual}^2 \sqrt{T_T}}{P_T A_{throat}^2 B} \right)^2 \Delta A_{throat}^2 \\ & + \left( \frac{-\dot{m}_{actual}^2 \sqrt{T_T}}{P_T^2 A_{throat} B} \right)^2 \Delta P_T^2 + \left( \frac{\dot{m}_{actual}^2}{2 P_T A_{throat} B \sqrt{T_T}} \right)^2 \Delta T_T^2 \end{aligned} \quad (B.4)$$

The error in the throat area is

$$\Delta A_{throat}^2 = (4.781 x_{plug} + 1.804)^2 \Delta x_{plug}^2 \quad (B.5)$$

Finally, the error in the weighted flow is given by

$$\begin{aligned} \Delta w^2 = & \left( \frac{14.696}{P_T} \sqrt{\frac{T_T}{518.7}} \right)^2 \Delta \dot{m}^2 + \left( \dot{m} \frac{14.696}{P_T^2} \sqrt{\frac{T_T}{518.7}} \right)^2 \Delta P_T^2 \\ & + \left( \frac{\dot{m} 14.696}{\sqrt{2 P_T T_T 518.7}} \right)^2 \Delta T_T^2 \end{aligned} \quad (B.6)$$

# Appendix C

## Engineering Drawings



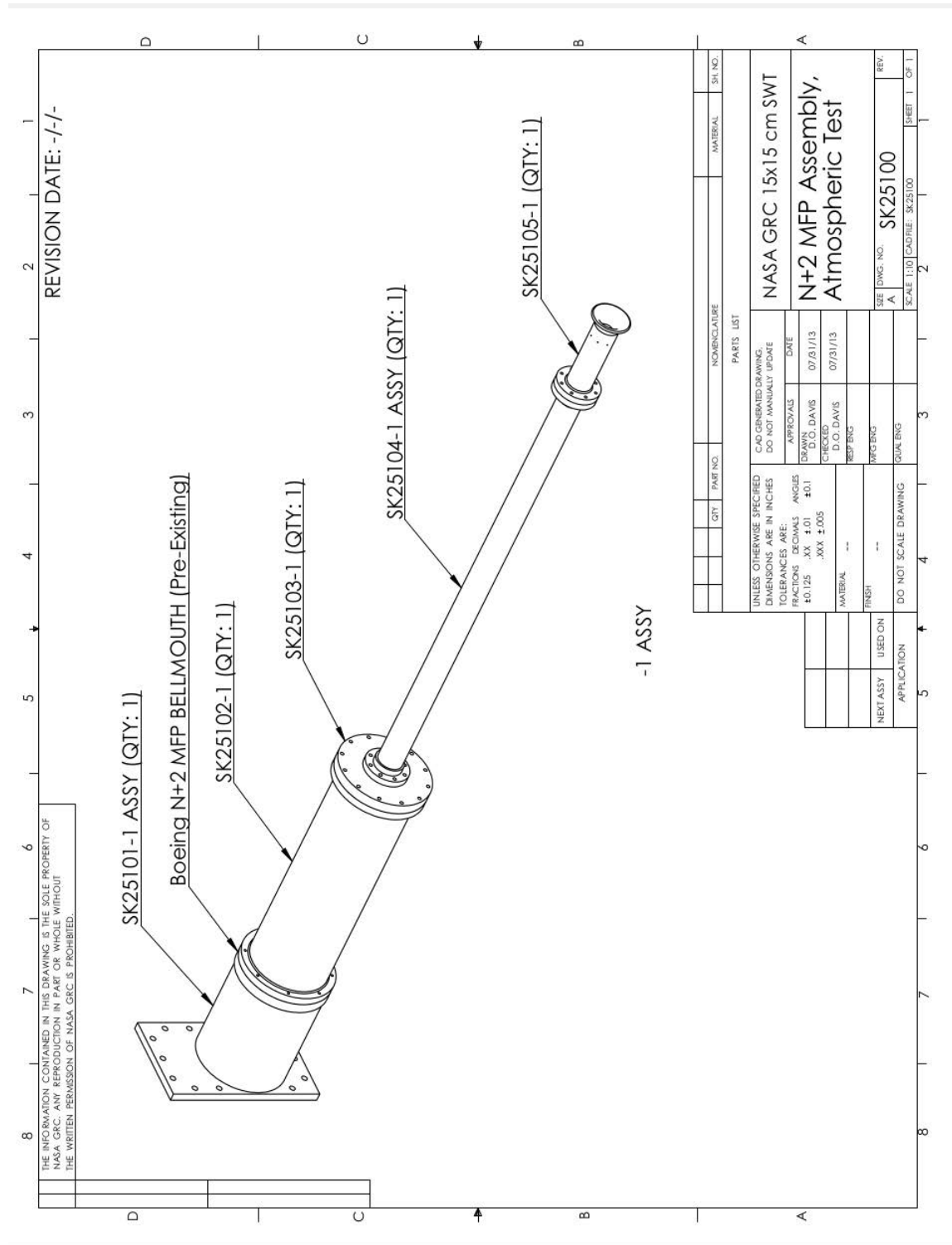
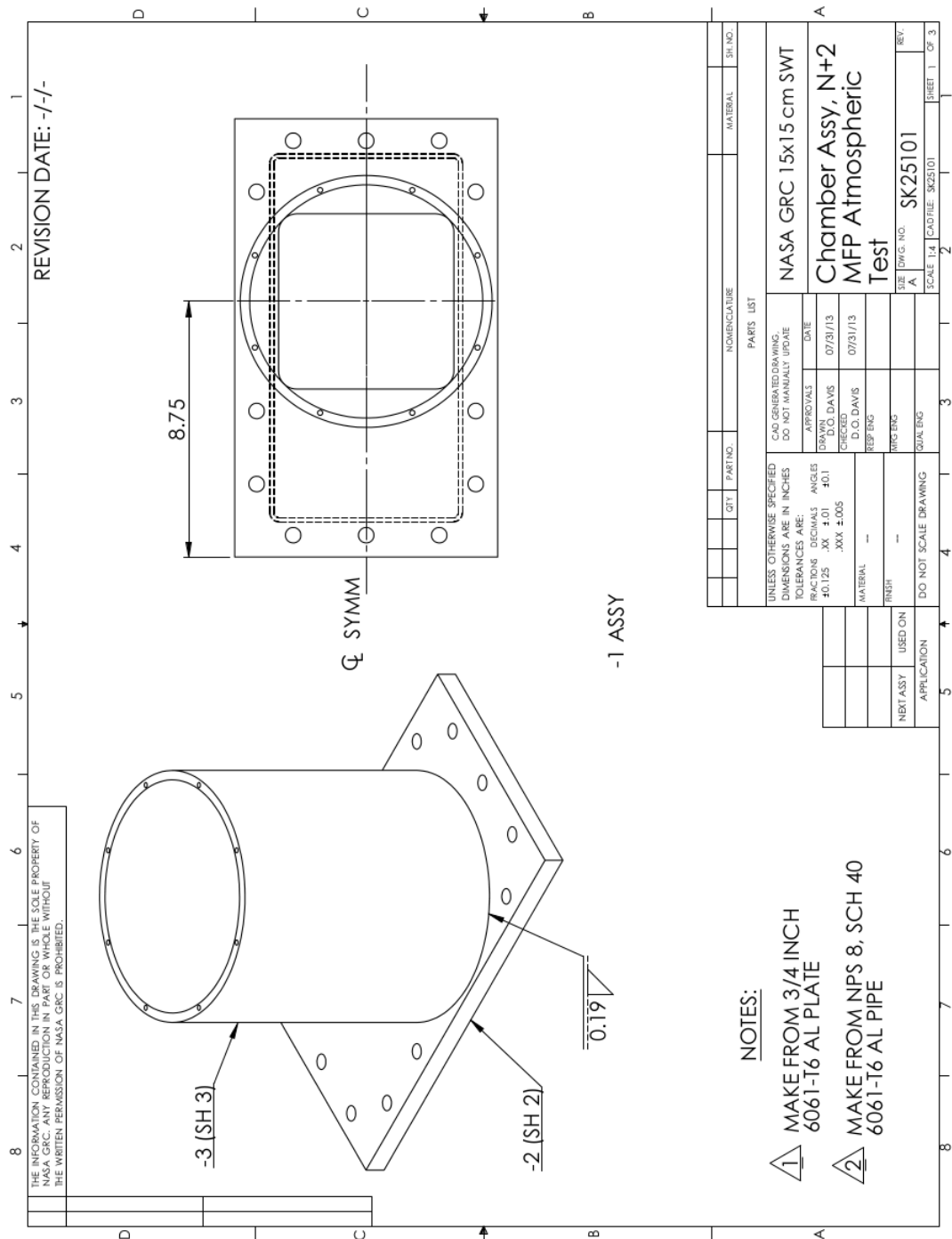


Figure C.1: MFP calibration rig assembly.



**Figure C.3:** *MFP support assembly- part 2.*

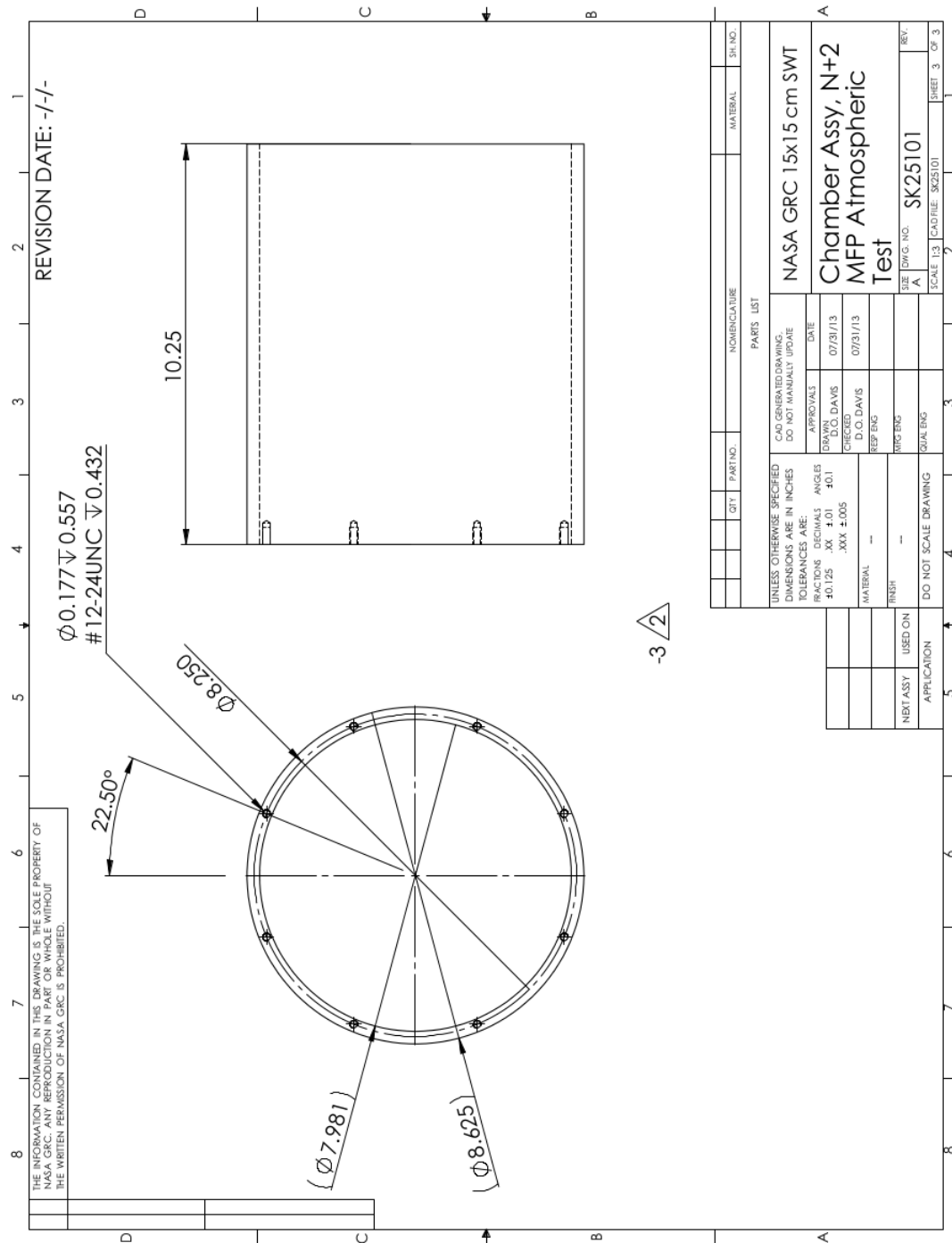


Figure C.4: MFP support assembly- part 3.

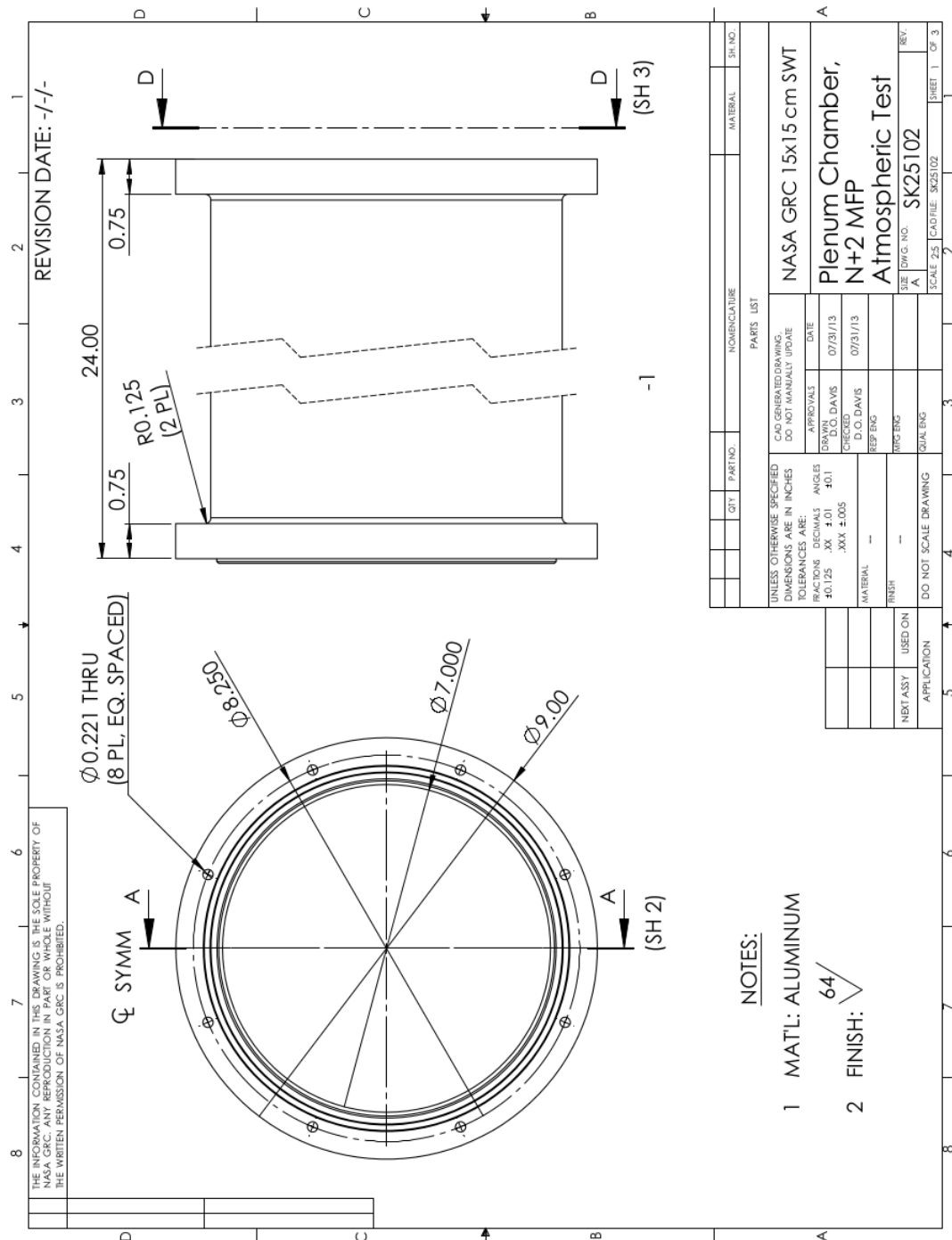


Figure C.5: Settling chamber- part 1.

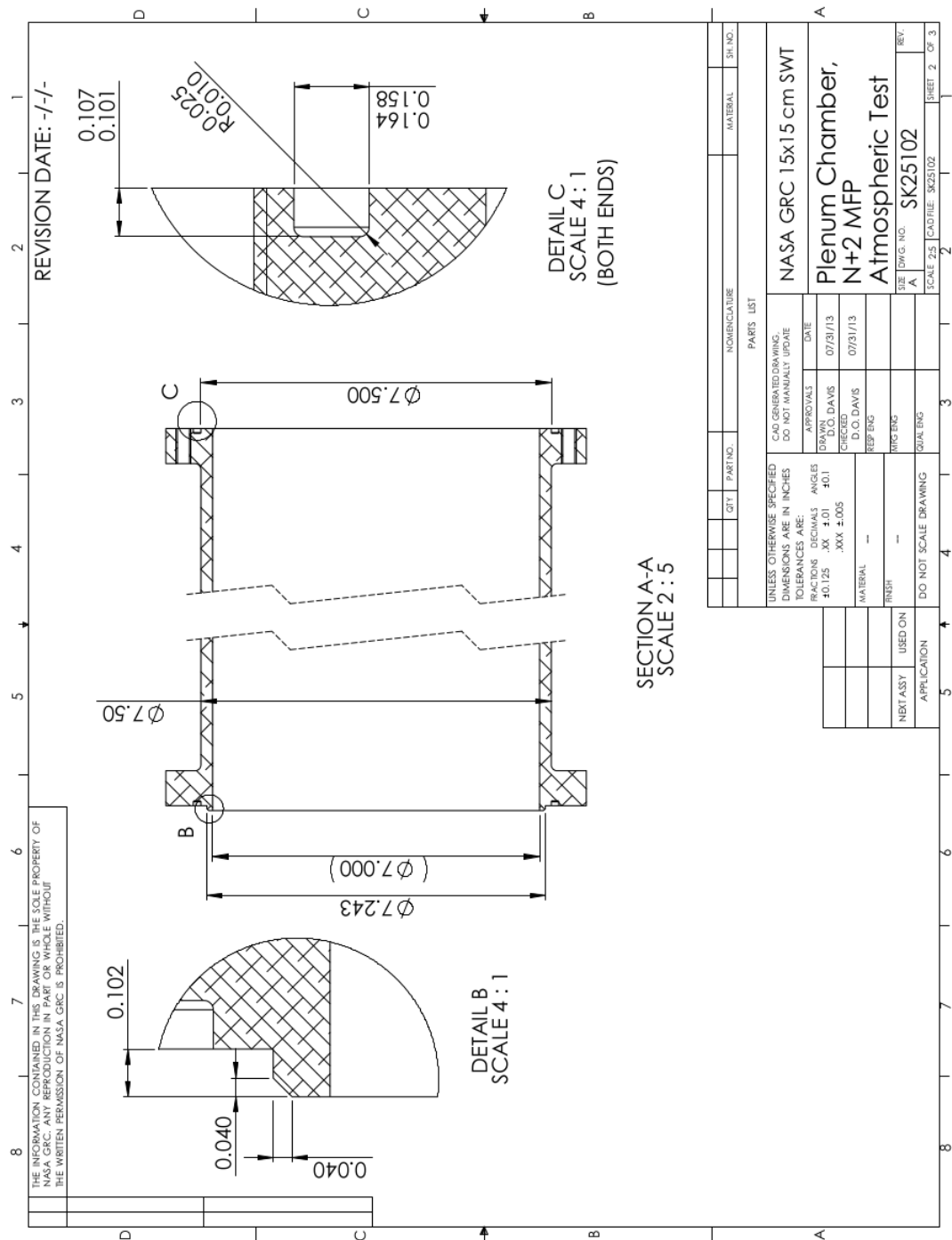


Figure C.6: Settling chamber- part 2.

Figure C.7: *Settling chamber- part 3.*





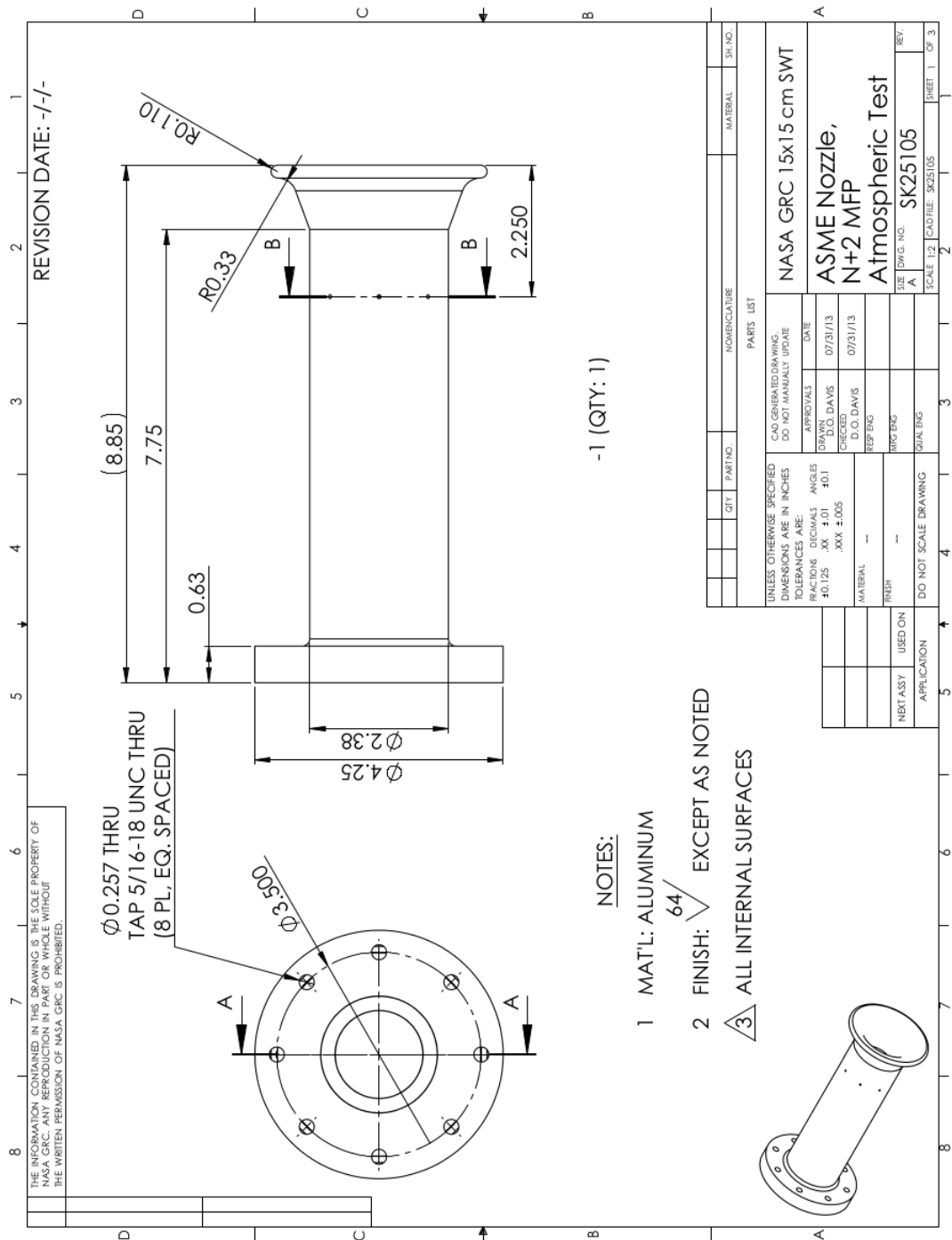


Figure C.9: ASME nozzle- part 1.

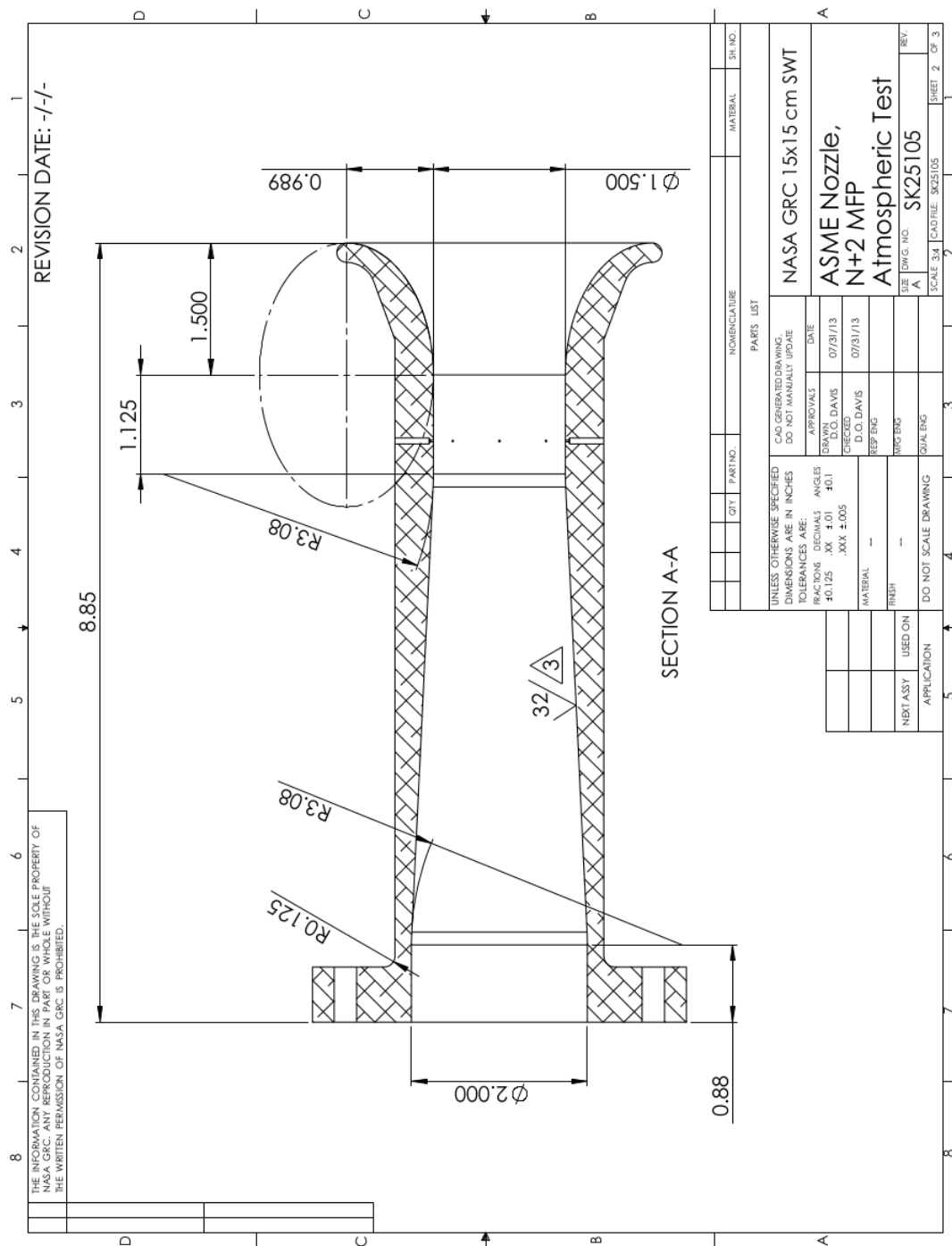


Figure C.10: ASME nozzle- part 2.

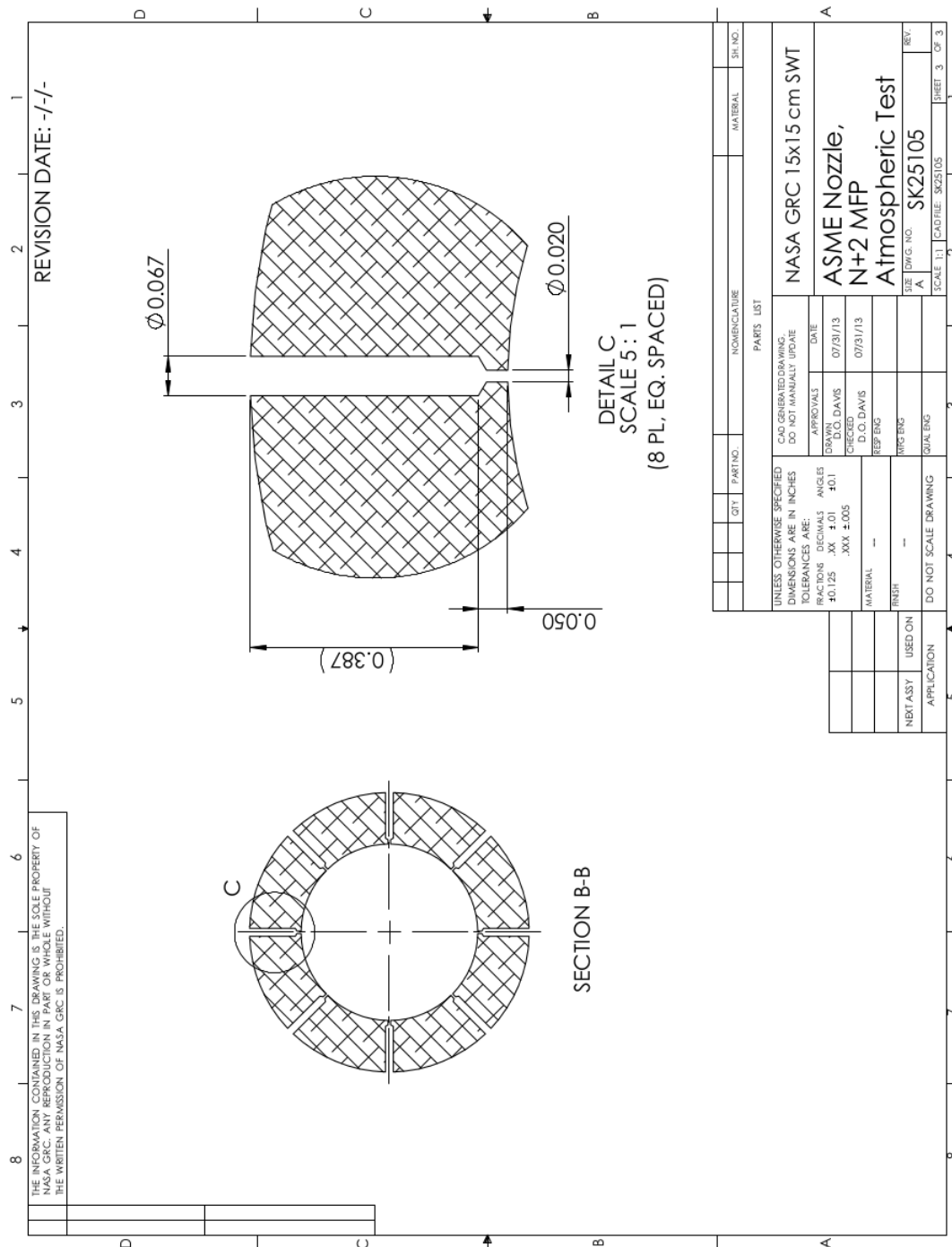


Figure C.11: ASME nozzle- part 3.

# Bibliography

- [1] D. O. Davis and J. D. Saunders, "Calibration of the NASA GRC 16" Mass-Flow Plug," in ASME, Rio Grande, Puerto Rico, 2012.
- [2] D. O. Davis, "Reference Mass-Flow Plug Calibration Experiments Test Requirements," NASA Glenn Research Center, Brook Park, OH, 2014.
- [3] J. Seddon and E. L. Goldsmith, Intake Aerodynamics, Reston, VA: AIAA Education Series, 1999.
- [4] A. H. Shapiro, The Dynamics and Thermodynamics of Compressible Fluid Flow, New York, NY: John Wiley & Sons, 1953.
- [5] P. J. Barnhart, "NPAC- Nozzle Performance Analysis Code," NYMA, Inc., Brook Park, OH, 1997.
- [6] F. M. White, Viscous Fluid Flow, New York, NY: McGraw Hill, 2006.
- [7] J. O. Hinze, Turbulence, New York, NY: McGraw Hill, 1975.
- [8] H. Schlichting and K. Gersten, Boundary Layer Theory, Germany: McGraw Hill, 2003.
- [9] J. Moran, An Introduction to Theoretical and Computational Aerodynamics, Mineola, NY: Dover Publications, 2003.
- [10] W. H. Press, S. A. Teukolsky, W. T. Vetterling and B. P. Flannery, Numerical Recipes in Fortran, New York, NY: Cambridge University Press, 1992.
- [11] R. H. Pletcher, J. C. Tannehill and D. A. Anderson, Computational Fluid

Mechanics and Heat Transfer, Boca Raton, FL: CRC Press, 2013.

[12] P. Z. Blumenthal, "A PC Program For Estimating Measurement Uncertainty for Aeronautics Test Instrumentation," in AIAA, San Diego, CA, 1995.

[13] "ARP 1420," SAE, Warrendale, PA, 2002.

[14] "ARP 246," SAE, Warrendale, PA, 2012.

[15] E. L. Goldsmith and J. Seddon, Intake Aerodynamics, Reston, VA: AIAA Education Series, 1999.

[16] E. L. Goldsmith and J. Seddon, Practical Intake Aerodynamic Design, Reston, VA: AIAA Education Series, 1993.





